UNIVERSITY OF CALIFORNIA

Los Angeles

Cortical Myosin Contraction Shapes the Morphogenesis of Microridge Patterns

A dissertation submitted in partial satisfaction of the

requirements for the degree Doctor of Philosophy

in Molecular Biology

by

Aaron Paul van Loon

2020

ABSTRACT OF THE DISSERTATION

Cortical Myosin Contraction Shapes the Morphogenesis of Microridge Patterns

by

Aaron Paul van Loon

Doctor of Philosophy in Molecular Biology

University of California, Los Angeles, 2020

Professor Alvaro Sagasti, Chair

The concept that form adapts to function has long been at the core of biological science. However, there are many cellular forms that we do not fully understand. Microridges are actin-based cell membrane protrusions that wind into labyrinthine patterns on the apical surfaces of mucosal epithelial cells, conferring a unique cellular morphology. Though the form of microridges has been studied in fixed tissues for many years, their morphogenesis is not understood. To investigate the formation of these enigmatic structures, I observed the process directly on the epidermis of developing zebrafish larvae using live fluorescence microscopy.

In Chapter 2 of this dissertation I describe the mechanism of microridge formation and the role of contractile force in this process. Prior to microridge formation, epithelial cells are covered in “pegs”, short finger-like protrusions that resemble microvilli. Pegs are dynamic, appearing and disappearing within a matter of minutes, as well as fusing with one another to form short microridges. As epithelial cells constrict, short microridges and pegs gradually assemble into elongated microridges in a pattern that begins near cell borders and progresses toward the center of the cell surface. A biophysical model of this process demonstrated that contraction of the apical actomyosin cortex in a similar concentric pattern leads to cellular constriction and microridge formation by reducing membrane tension. Observation of myosin activity in live epithelial cells demonstrated that contraction progresses in a concentric manner and small molecule inhibition

of contraction blocked both cellular constriction and microridge formation. Reduction of membrane tension through hyperosmolar shock and reorganization of the apical cortex through rapid cell elongation demonstrated that microridge formation is directly regulated by membrane tension and the organization of the cortical cytoskeleton.

Chapter 3 describes the mechanics of microridge formation and pattern maturation with high spatial resolution. After formation, microridges elongate further, align with their neighbors, and become more regularly spaced. Microridge fusion and fission continue during this period of pattern maturation and these events correlate spatially and temporally with cortical myosin contraction. However, microridge rearrangements diminish after microridge formation and negatively correlate with the degree of microridge alignment. Inhibiting myosin contraction prevented microridge rearrangements and disrupted the microridge pattern. High-resolution Airyscan microscopy revealed individual myosin minifilaments in the cortex that connect microridges to one another and mediate microridge rearrangements through contraction.

Overall, this work elucidates the mechanism of microridge formation. Pegs and microridges fuse, fission, and gradually rearrange, a process driven by the web-like network of myosin minifilaments in the apical cortex which contracts to reduce membrane tension. As myosin contraction diminishes, the input needed to overcome the energy barrier associated with the changes in membrane curvature during microridge rearrangement is decreased, and microridges slowly settle into their highly organized patterns.

The dissertation of Aaron Paul van Loon is approved.

Allison Renee Frand

Luisa Iruela Arispe

Alexander Jacob Levine

Margot Elizabeth Quinlan

Alvaro Sagasti, Committee Chair

University of California, Los Angeles

2020

Dedication

To my parents, whose love and guidance set me on this path

To my brothers, for a lifetime of fellowship

To Samantha Edwards, my partner in everything

TABLE OF CONTENTS

LIST OF FIGURES AND TABLES

ACKNOWLEDGEMENTS

I would like to thank my advisor, Dr. Alvaro Sagasti, for his mentorship and for the freedom to explore my own scientific path. I must also thank the past and current members of the Sagasti lab who were a daily source of friendship and technical expertise. I want to express my enormous gratitude to Dr. Ivan Erofeev and Dr. Andrew Goryachev for all the time and effort they poured into our collaborative research. My graduate work and our collective publications were truly enriched by working together. Finally, I would like to thank my undergraduate mentors Dr. Donna Nofziger, Dr. Thomas Vandergon, and Dr. Jay Brewster for guiding me through my first steps toward a future in scientific research.

VITA

EDUCATION

Doctor of Philosophy, Molecular Biology 2014 - 2020
University of California, Los Angeles

Bachelors of Science, Biology 2010 - 2014
Pepperdine University

RESEARCH EXPERIENCE

Doctoral Candidate 2015 - 2020
PI: Dr. Alvaro Sagasti, UCLA
Thesis: Cortical myosin contraction shapes the morphogenesis of microridge patterns

Undergraduate Honors Thesis 2011 - 2014
PI: Dr. Nofziger Plank, Pepperdine University
Thesis: Notch signaling decreases expression of MMP2 in HLECs

FELLOWSHIPS AND AWARDS

Dissertation Year Fellowship, UCLA 2019 - 2020
Whitcome Pre-Doctoral Fellowship, UCLA 2018 - 2019
Cellular and Molecular Biology Training Grant, UCLA 2015 - 2018
Outstanding Student in Biology Award, Pepperdine University 2014
NSF REU Fellowship, Pepperdine University 2012

TEACHING AND MENTORSHIP EXPERIENCE

UCLA, Department of Molecular, Cellular, and Developmental Biology, Los Angeles, CA
Teaching Assistant
Biology of Cells 2015, 2017

Pepperdine University, **Natural Sciences Division**, Malibu, CA
Teaching Assistant
Genetics & Human Affairs 2014

RELATED PROFESSIONAL EXPERIENCE

GPB Student Advisory Committee Member 2018 - 2019
UCLA

Internal President of the Biological Sciences Council 2017 - 2019
UCLA

MBIDP Representative on the Biological Sciences Council 2015 - 2017
UCLA

PUBLICATIONS

van Loon AP, Erofeev IS, Goryachev AB, Sagasti A. Cortical myosin minifilaments orchestrate the arrangement of microridge protrusions on epithelial cell surfaces**.** bioRxiv 202 Oct 22;351312; doi: https://doi.org/10.1101/2020.10.22.351312

van Loon AP, Erofeev IS, Maryshev IV, Goryachev AB, Sagasti A. Cortical contraction drives the 3D patterning of epithelial cell surfaces. J Cell Biol. 2020 Mar 2;219(3). doi: http://dx.doi.org/10.1083/jcb.201904144 PMID: 32003768

Patel AA, Oztug Durer ZA, **van Loon AP**, Bremer KV, Quinlan ME. Drosophila and human FHOD family formin proteins nucleate actin filaments. J Biol Chem. 2018 Jan 12;293(2):532–540.

SELECTED PRESENTATIONS

van Loon AP, Erofeev I, Maryshev I, Goryachev A, and Sagasti A. *Cortical Contraction Sculpts the Apical Surface of Epithelial Cells*. Southern California Fish Meeting. Los Angeles, CA. 2019. Oral Presentation.

van Loon AP, Erofeev I, Goryachev A, and Sagasti A. *Non-muscle Myosin II contraction sculpts apical protrusions of mucosal epithelial cells*. Annual Meeting of the American Society for Cell Biology. San Diego, CA. 2018. Poster.

van Loon AP, Lu T, and Sagasti A. *Tight junctions pattern Myosin II contractions that sculpt the surface of mucosal epithelial cells*. Annual Meeting of the International Zebrafish Society. Madison, WI. 2018. Poster.

van Loon AP, Lu T, and Sagasti A. *Contractile Forces Shape the Labyrinthine Surface of Mucosal Epithelial Cells*. "Motile & Contractile Systems" Gordon-Kenan Research Seminar. New London, NH. 2017. Oral Presentation and Poster.

van Loon AP and Sagasti A. *Non-muscle Myosin II and Rho Kinase play distinct roles in microridge formation and maintenance, sometimes in a single pathway, sometimes in opposition*. Annual Meeting of the American Society for Cell Biology. San Francisco, CA. 2016. Poster.

van Loon AP, Chauhan V, and Sagasti A. *Morphogenesis of Epithelial Microridges in Zebrafish*. Annual Meeting of the American Society for Cell Biology, San Diego, CA. 2015. Poster.

van Loon AP. *The Effect of the Notch Signal Pathway on the Expression of Matrix Metalloproteinase 2 in Human Lymphatic Endothelial Cells*. Annual Meeting of the American Society for Cell Biology, New Orleans, LA. 2013. Poster.

Chapter 1

Introduction

Epithelial cells present a variety of apical cell membrane protrusions which create morphologies that fit their functions. In contrast to filopodia and lamellipodia, which are transient protrusions that perform temporary functions, microvilli, stereocilia, and microridges are apical protrusions on epithelial cells that are relatively stable and perform their functions over the lifetime of the cell. The contexts and time-scales in which these apical protrusions develop have made them more difficult to study than other types of protrusions. Microvilli are short, finger-like protrusions that are regularly arranged on the surfaces of intestinal and renal epithelia to perform the function of nutrient absorption. Stereocilia are elongated finger-like protrusions arranged in triangular formations that display a highly regular gradient of protrusion lengths and perform the mechanotransduction of hearing. Despite differences in protrusion organization and function, microvilli and stereocilia share a similar morphology. Microridges are elongated folds of the apical cell membrane that create labyrinthine patterns on the surface of mucosal epithelial cells, making them morphologically unique among apical protrusions. While progress has been made toward understanding the formation and maintenance of microvilli and stereocilia, almost nothing is known about microridge morphogenesis.

Microridge structure and function

Microridges were first mentioned in the literature in the 1960s (Blümcke and Morgenroth, 1967). Since then, they have been found on a variety of tissues from many different animal species, but have primarily been studied in fish and humans (Depasquale, 2018). In humans, microridges have been found on epithelia of the esophagus, kidney, and cornea, among many other tissues (Depasquale, 2018). Since many studies of these structures are descriptive in nature, it remains unclear whether the protrusions on each of these tissues are molecularly similar structures. This ambiguity is illustrated by the variety of names used to refer to protrusions on these various tissues, including microridges (Fahrenbach and Knutson, 1975), microplicae (Blümcke and Morgenroth, 1967), and sometimes, simply, microvilli (Dormans and van Logten,

1982). What is clear, is that microridges represent a large group of morphologically similar protrusions that are found broadly on mucosal epithelia.

Though little research has been done on the subject, the function of microridges has been the topic of much speculation. One enduring hypothesis is that the primary function of microridges is to increase surface area for mucus retention (Sperry and Wassersug, 1976). This hypothesis has only recently begun to be tested experimentally. Small molecule inhibitors that disrupt microridge patterns also affect the organization of the overlying glycan layer (Pinto et al., 2019). Additionally, in treatment conditions where microridges are nearly completely destroyed, mucus levels are reduced and the surface glycans that persist appear to preferentially coat the remaining membrane protrusions (Pinto et al., 2019). It is still unclear whether microridges are required to retain mucus on a tissue, and if they are, in what capacity they contribute to its retention: whether they provide an optimal morphology to capture and retain mucus through purely physical means, or whether microridge projections simply contain a greater number of molecular binding sites for glycoproteins (Blalock et al., 2007). Microridges have also been speculated to serve as a membrane reserve in case a cell is stretched, due to their presence on esophageal epithelial cells (Wassersug and Johnson, 2009). In support of this hypothesis, microridges are lost or fragmented when epithelial cells are stretched during wound healing (Rai et al., 2012; Richardson et al., 2016; Verma et al., 2017). It may be that multiple of these hypotheses are true, but more extensive experimentation will be needed to determine the functions of microridges in the various contexts in which they appear.

To gain further insight into the function of microridges, it will be necessary to understand the molecular structure and composition of these unique protrusions. Early studies of microridge ultrastructure noted that microridges were associated with keratin filaments at their base and filled with thinner filaments (Schliwa, 1975). The thinner filaments that filled microridge protrusions were later confirmed to be actin filaments using immunofluorescence and further electron

microscopy (Bereiter-Hahn et al., 1979). The actin filaments are connected to the keratin filaments in the terminal web below microridges (Uehara et al., 1990), which contains both actin and keratin filaments (Bereiter-Hahn et al., 1979). Interestingly, keratin filaments can also be found within microridges (Uehara et al., 1991; Pinto et al., 2019; Inaba et al., 2020). The precise organization of the actin filaments that fill microridge protrusions is still unclear. TEM studies have found branched actin filaments oriented in many directions within microridges (Bereiter-Hahn et al., 1979; Uehara et al., 1991; Pinto et al., 2019; Schliwa, 1975). Some of these studies also observed the presence of linear actin filament bundles that appear to support microridges from base to tip (Bereiter-Hahn et al., 1979; Schliwa, 1975; Uehara et al., 1991), although one study concluded that microridges exclusively contain branched filaments (Pinto et al., 2019). Differences in the conclusions of these studies could be attributed to observations made in different animal species, or to differences in sample preparation. Observations of bundled actin filaments in apparent columns that are periodically positioned along microridges (Bereiter-Hahn et al., 1979; Uehara et al., 1991; Depasquale, 2018), have lead some to hypothesize that microridges may be organized like a fence, with branched actin meshwork connecting bundled actin “fence posts.” This hypothesis is supported by the observation that multiple microridge fluorescent reporters, including actin itself, appear punctate by light microscopy (Depasquale, 2018). The actin filaments within microridges also appear to have many connections to the plasma membrane (Bereiter-Hahn et al., 1979; Uehara et al., 1990; Schliwa, 1975). The true molecular organization of microridges will be revealed as we learn more about the various actin- and keratin-binding proteins that build and organize the cytoskeletal network that supports microridges.

So far, only a few actin- and keratin-binding proteins have been found to associate with microridges. A recent publication from the Sagasti lab demonstrated that cytolinkers envoplakin and periplakin connect the actin and keratin cytoskeletal networks and that this connection is

required for microridge formation (Inaba et al., 2020), providing the first evidence of a role for keratin filaments in apical protrusion formation. The actin-binding proteins that have been found in microridges are associated with diverse cytoskeletal architectures. Arp2/3, Cortactin, and WASL localize to microridges (Pinto et al., 2019; Lam et al., 2015) and are all associated with branched actin networks. However, proteins associated with bundled actin, including VASP and α-actinin, have also been identified in microridges (Bereiter-Hahn et al., 1979; Lam et al., 2015). Other actin-binding proteins in microridges include Ezrin (Raman et al., 2016), a membrane-actin linking protein; Paxillin (Crawford et al., 2003), a component of focal adhesion complexes; and Cofilin (Pinto et al., 2019), an actin-severing protein. Even among the limited pool of proteins thus far identified, microridges share components with many protrusions including lamellipodia (Arp2/3 and VASP) and filopodia (VASP) (Rottner and Schaks, 2019), as well as microvilli (Ezrin) (Crawley et al., 2014a). Given this fact, a useful approach to learn more about microridge structure and function may be to look for additional proteins that are found in other actin-based protrusions and determine whether they play analogous roles in microridges.

The roles of myosins in apical cell membrane protrusions

The motor protein non-muscle myosin II (NMII) has also been identified in microridges (Raman et al., 2016). Myosins compose a large protein superfamily and play a variety of roles in multiple cellular protrusions. The diverse members of the myosin protein superfamily are divided into many classes, but each has a common domain structure: a head domain that binds to actin and hydrolyzes ATP to produce movement, a neck domain that binds to light chains that modify its activity, and a tail domain which is typically used to position the molecule, but can have a variety of functions. Variations of the myosin protein template, such as subtle differences in the activity of the motor head, or an additional protein-protein interacting domain in the tail can have large impacts on the function and regulation of the molecule. The numerous variants among members of the myosin superfamily allow this group of actin-based motor proteins to generate

force in a variety of manners and contexts. The essential roles that myosins play in the formation and maintenance of apical protrusions demonstrate that these processes not only require regulation of the actin cytoskeleton, but also regulation of force.

Conventional Myosins

Class II myosins were the first to be discovered and are the classical force-generating myosins, often referred to as “conventional myosins.” These myosins form hexameric macromolecules which include two myosin heavy chains (myosin gene products), two regulatory light chains (RLCs), and two essential light chains. Myosin II macromolecules can assemble into filaments through interactions between their long coiled-coil tail domains. This filamentous organization allows class II myosins to generate contractile forces when bound to the actin cytoskeleton in both muscle and non-muscle cells. A broad expression pattern and versatility as a force-generator allow myosin II to function in the formation and maintenance of several apical cell membrane protrusions.

NMII is found in the terminal web below microvilli (Chinowsky et al., 2020), and plays multiple roles in the formation and maintenance of these protrusions. It helps instruct formation of microvilli through the indirect, though crucial, mechanism of apical domain specification; contractile activity of NMII is required for epithelial polarization and microvilli formation in cultured canine kidney epithelial MDCK cells and in Drosophila photoreceptors (Zihni et al., 2017). Myosin activation through phosphorylation of its RLC by MRCK is specifically required for differentiation of the apical domain in these contexts, while activity of another RLC kinase, ROCK, is antagonized by the MRCK-activating GTPase Cdc42 (Zihni et al., 2017). This example shows the complexity and specificity of NMII regulation, but NMII also has more direct functions in the morphogenesis of microvilli. NMII contraction stimulates actin turnover in microvilli, which regulates their length

(Chinowsky et al., 2020). NMII also contributes to microvillar motility during brush border maturation (Meenderink et al., 2019), likely through a similar mechanism.

In cells with stereocilia, NMII localizes throughout the length of the stereocilia, in the rootlets, and also near the apical membrane between protrusions (Lalwani et al., 2008). Notably, NMII is absent from the tips of stereocilia, where several unconventional myosins are known to localize (Lalwani et al., 2008). The importance of NMII in stereocilia is emphasized by the hearing loss found in patients with mutations in the NMII heavy chain MYH9 gene (Verver et al., 2016). However, molecular studies have not yet pursued the function of NMII in stereocilia, or a mechanism for its pathology.

NMII also plays a role in microridge morphogenesis, although current studies on the topic present conflicting results. Lam et al first reported that short-term treatment with the NMII inhibitor, blebbistatin, had no effect on microridge morphology (Lam et al., 2015) . They also noted that they could not detect phosphorylated Myosin RLC in microridges using immunofluorescence (Lam et al., 2015). However, they did find that expression of either constitutively active or dominant negative RhoA, a small GTPase well-known for regulating NMII activity, affects microridge morphology. Cells expressing constitutively active RhoA presented a web-like microridge pattern, and the surfaces of these cells became domed, rather than flat (Lam et al., 2015). Dominant negative RhoA increased both apical cell surface size and the spacing between microridges (Lam et al., 2015). In direct contrast to the preceding study, Raman et al observed phosphorylated myosin RLC in microridges, using a different antibody, and reported that blebbistatin treatment reduced microridge length (Raman et al., 2016). They also found that overexpression of a constitutively active myosin activator, MLCK, increases microridge length, suggesting that NMII contraction is important for microridge length maintenance (Raman et al., 2016). Raman et al also demonstrated that aPKC suppresses NMII activity at the apical membrane by removing the NMII-interacting protein Lgl from the apical membrane (Raman et al., 2016). Since aPKC

localization and activity are dependent on another small GTPase, Cdc42 (Goldstein and Macara, 2007), regulation of NMII in microridge morphogenesis appears complex. Interestingly, Cdc42 antagonizes RhoA-mediated NMII activity in cells with microvilli (Zihni et al., 2017). So, although both GTPases appear to control separate aspects of microridge morphogenesis, organization versus length maintenance, our understanding of NMII activity and regulation in microridge morphogenesis remains incomplete. I directly address this knowledge gap in this dissertation by imaging NMII activity during microridge morphogenesis using live fluorescence microscopy.

Membrane-actin tethering myosins

While there is only one class of conventional myosins, there are many classes of unconventional myosins that perform a wide variety of functions in apical membrane protrusions. Myosins in classes I and VI link the membrane to the cytoskeleton in both microvilli and stereocilia.

There are eight myosin I proteins expressed in higher vertebrates, Myo1a-h (Gillespie et al., 2001). Class I myosins are monomeric with neck regions that contain a variable number of IQ domains which bind Ca^{2+}-regulated light chains, like calmodulin (McIntosh and Ostap, 2016). Myosin I proteins share a tail homology domain (TH1) which contains a plekstrin homology (PH) domain that can bind various phospholipids (McIntosh and Ostap, 2016); although, Myo1e and Myo1f possess additional tail domains which can mediate interactions with other proteins (Krendel et al., 2007) and regulate ATPase activity (Stöffler and Bähler, 1998).

Class 1 myosin Myo1a connects the membrane and the actin core throughout the microvillus protrusion (Mooseker and Tilney, 1975; Howe and Mooseker, 1983). It is targeted to microvilli and associates with the membrane using the TH1 domain in its tail region, which binds to PI(4,5)P2 (Mazerik and Tyska, 2012). The Myo1a motor head is a low-duty-ratio motor, so it binds to the actin core of microvilli infrequently (Jontes et al., 1997). Despite this, the large number of Myo1a molecules independently cycling in microvilli allows for continuous membrane-

actin cross-linking (Brown and McKnight, 2010). In fact, the transient interaction between Myo1a and actin may be an advantageous way for Myo1a, and the attached membrane, to avoid being pulled downward by actin treadmilling (Brown and McKnight, 2010). Enterocytes in *Myo1a* KO mice have fused microvilli and gaps between the membrane and the microvillar actin core (Tyska et al., 2005), demonstrating that Myo1a is critical to maintain the structural integrity of microvilli, possibly through its ability to directly regulate membrane surface tension (Nambiar et al., 2009). Surprisingly, *Myo1a* KO microvilli are still functional (Tyska et al., 2005), though this may be the result of compensation from other class 1 myosins (Myo1c and Myo1d) that are recruited along microvilli in its absence (Tyska et al., 2005; Benesh et al., 2010).

Myo1c is another single-headed class 1 myosin that binds tightly to PIP_2 through the PH domain in its tail (Hokanson et al., 2006). The N-terminal region of Myo1c confers unique force sensitivity (Greenberg et al., 2015; Zattelman et al., 2017), which gives it properties more similar to that of a slow transporter than a tension-sensitive anchor (Greenberg et al., 2012). Myo1c is localized throughout the length of stereocilia (García et al., 1998; Steyger et al., 1998), though some data suggest it is excluded from the tip (Schneider et al., 2006). In hair cells, Myo1c mediates the adaptation of ion channels, which is important for mechanotransduction in hearing (Stauffer et al., 2005; Holt et al., 2002). Mutations in *Myo1c* are genetically associated with bilateral sensorineural hearing loss (Zadro et al., 2009). The role of Myo1c in the formation and maintenance of stereocilia morphology has yet to be investigated.

Class VI myosin Myo6 can function as a monomer, dimer, or oligomer, depending on the context and cargo that is bound (de Jonge et al., 2019), and it is the only myosin to move toward the pointed end of actin filaments (Wells et al., 1999). Unique insertions in its motor domain distinguish it from other myosins, modifying its ATPase activity and reorienting its lever arm to allow for reverse movement (Ménétrey et al., 2005). Otherwise, myosin VI contains one calmodulin-associated IQ domain, a coiled-coil domain, and a globular c-terminal domain (Hasson

and Mooseker, 1994). Under high load, Myo6 stepping activity dramatically slows, suggesting a force-sensitive transition from functioning as a transporter to a tension-sensitive anchor (Altman et al., 2004).

In intestinal enterocytes, Myo6 localizes to the terminal web below microvilli (Heintzelman et al., 1994). Myo6 has been shown to directly bind to lipids, through a PIP_2-binding domain in its tail (Spudich et al., 2007), although it is unclear whether this domain is directly involved in its localization in enterocytes. Myo6 also directly binds to PLCδ3, which is required for Myo6 expression in the lower ileum and for proper formation of microvilli in Caco-2 cells (Sakurai et al., 2011). Given that PLCδ3 regulates PIP_2 (Streb et al., 1983), it is unclear whether loss of PLCδ3 affects Myo6 directly, or through its control of phosphoinositide levels. Interestingly, Myo6 localization to the brush border has also been shown to be dependent on Myo1a (Tyska et al., 2005). Enterocytes in *Snell's waltzer* (*Myo6)* KO mice show clear defects in microvillar morphology. Loss of Myo6 results in fusion of microvilli and the lifting of the inter-microvillar membrane, which effectively shortens the protrusions (Hegan et al., 2012).

Myo6 also plays important structural and functional roles in stereocilia. In stereocilia, Myo6 localizes along the length of the protrusion, but is particularly concentrated near the base (Rzadzinska et al., 2004; Hertzano et al., 2008), consistent with its preference for curved membranes *in vitro* (Rogez et al., 2019). Phenotypes of stereocilia in *Myo6* KO hair cells are strikingly similar to those found in the microvilli of *Myo6* KO intestinal enterocytes: stereocilia fuse and branch abnormally and the membrane at the base of stereocilia is lifted (Hertzano et al., 2008; Seiler et al., 2004; Seki et al., 2017). Loss of Myo6 also results in the disorganization of the cuticular plate that underlies stereocilia, as well as movement of cuticular plate components upward into the stereocilia themselves (Seki et al., 2017). The morphological defects associated with the loss of Myo6 result in nonsyndromic hearing loss (Avraham et al., 1995; Melchionda et al., 2001). However, it is unclear whether the phenotype of *Myo6* KO in hair cells is the result of

defects in membrane-actin attachment, Myo6 cargo transport, the organization of the cuticular plate, or some combination of these functions.

Transport myosins

Class III myosins are monomeric myosins that function as cargo transporters to the tips of stereocilia (Nambiar et al., 2010). A unique feature of class III myosins is their N-terminal kinase domain (Dosé and Burnside, 2000; Dosé et al., 2003). The activity of the kinase domain and the motor domain are regulated by *trans*-autophosphorylation and, possibly, by other kinases (Quintero et al., 2013; Komaba et al., 2003). Phosphorylation of the kinase domain increases its activity and additionally modulates motor ATPase activity (Quintero et al., 2013), while phosphorylation of the motor domain decreases its ATPase activity (Quintero et al., 2013, 2010). Loss of kinase activity or deletion of the kinase domain result in increased Myo3a localization to the tip of filopodia and stereocilia protrusions, possibly due to the associated increases in motor activity (Quintero et al., 2010, 2013; Les Erickson et al., 2003). Another unique feature of class III myosins is their method of locomotion: they use separate actin-binding sites at opposing ends of the molecule to move processively in an inchworm-like manner. To accomplish processive locomotion, Myo3a uses an actin-binding site in its C-terminal tail homology domain II (THDII) to increase its steady state interaction with actin (Dosé et al., 2007; Les Erickson et al., 2003). This THDII is required for Myo3a tip localization in filopodia (Les Erickson et al., 2003). Myo3b has a shorter tail than Myo3a and lacks the THDII (Dosé et al., 2003). However, association of the Myo3b THDI with the protein espin-1 allows movement of Myo3b along filopodia (Merritt et al., 2012). This process requires the espin-1 actin-binding module of Myo3b (Merritt et al., 2012), suggesting a similar method of locomotion to Myo3a, but rather than binding actin directly, Myo3b can bind actin through interaction with espin-1.

In hair cells, Myo3a and Myo3b localize to the tips of stereocilia with differing preferences for stereocilia length. Myo3a localizes preferentially to intermediate length stereocilia and less to long or short ones, while Myo3b localizes preferentially to the longest stereocilia and less to stereocilia of other lengths (Ebrahim et al., 2016). Two important myosin III cargos in stereocilia are actin-binding proteins espin-1 and espin-like, which control stereocilia length and are essential for hearing (Ebrahim et al., 2016; Rzadzinska et al., 2005; Zheng et al., 2000). Deletion of *Myo3a* results in late-onset deafness (Walsh et al., 2002; Dantas et al., 2018), although stereocilia in *Myo3a*$^{-/-}$ mice appear normal (Ebrahim et al., 2016). *Myo3b* mutations have not been associated with deafness, but the longest and shortest stereocilia in *Myo3b*$^{-/-}$ mice are, respectively, shorter and longer than WT, equalizing their height (Ebrahim et al., 2016). Despite differential effects of *Myo3a* and *Myo3b* knockout on stereocilia morphology, both show clear roles in the length regulation of stereocilia and filopodia (Salles et al., 2009; Schneider et al., 2006; Ebrahim et al., 2016). Deletion of *Myo3a* and *Myo3b* together results in deafness and progressive morphological and organizational abnormalities in stereocilia prior to, and shortly after, birth (Lelli et al., 2016). Hair bundles on cells from *Myo3a*$^{-/-}$ *Myo3b*$^{-/-}$ mice lose their characteristic “U” or “V” shaped organizations and have unusually long stereocilia (Lelli et al., 2016).

Class V myosins are double-headed myosins that travel toward the barbed ends of actin filaments, and are best known for their role in cargo transport. Myosin V motors are excellent transporters because they have a high duty ratio: the slow kinetics of its strong actin-binding transition state allow for processive movement along actin filaments (De La Cruz et al., 1999). The elongated neck region of myosin V proteins acts as an extended lever arm that results in a 36nm step size, permitting linear travel along helical actin filaments which have a pitch of similar length (Hammer and Sellers, 2011). The motor activity of class V myosins is autoinhibited by interactions between the N-terminal motor heads and the C-terminal globular tail domains (Thirumurugan et al., 2006; Liu et al., 2006). The interactions between the head and tail domains

are relieved in the presence of free Ca^{2+} by the six calmodulins that bind the IQ domains in the neck of Myosin V under these conditions (Wang et al., 2004; Gardini et al., 2018). While Ca^{2+}-dependent activation of the calmodulin bound at the IQ motif nearest to the motor domain is essential for Myosin V motor function (Lu et al., 2012), high levels of Ca^{2+} promote the dissociation of calmodulin from the second IQ motif resulting in a flexible neck that cannot perform mechanical work (Trybus et al., 2007; Nguyen and Higuchi, 2005; Koide et al., 2006). Myo5a autoinhibition can also be regulated by binding cargo receptors. Melanophilin can activate Myo5a motor activity by binding to its tail domain, allosterically inhibiting interactions with the head domain (Li et al., 2005; Yao et al., 2015). Although much work has been done on the structure, activity, and regulation of Myosin V, relatively little investigation has been dedicated to its role in apical protrusions.

Myo5b in enterocytes localizes apically, above the terminal web, and plays an important role in membrane trafficking to the brush border. Mutations in *Myo5b* have been identified as a primary genetic determinant of Microvillus Inclusion Disease (MVID) (Weis et al., 2016), a life-threatening condition in newborns that causes severe diarrhea and malnutrition (Ruemmele et al., 2006; Davidson et al., 1978). Genetic KO of *Myo5b* results in large, microvilli-lined inclusions in intestinal enterocytes that contain transmembrane proteins, microvillar components, and extracellular proteins, as a result of disrupted apical polarity and bulk endocytosis (Knowles et al., 2014; Weis et al., 2016; Engevik et al., 2019). In *Myo5b* KD CaCo2-BBE cell cultures, microvillus development appears to stall after formation of early microvilli clusters, never forming an organized brush border (Knowles et al., 2014). While *Myo5b* KO mouse neonates have an organized brush border, their microvilli are shorter and wider than WT (Weis et al., 2016).

Thus far, one study has found a role for Myo5b in microridge morphogenesis. Periderm cells on *Myo5b* KD zebrafish larvae had smooth apical surfaces, completely lacking microridge projections (Sonal et al., 2014). This could be the result of a dramatic increase in endocytosis

from the apical membrane (Sonal et al., 2014). However, Myo5b also regulates apico-basal polarity in *Drosophila* follicle cells through transport of Crumbs to the apical domain (Aguilar-Aragon et al., 2020). So, it is also possible that periderm cells on Myo5b KD zebrafish have impaired apico-basal polarity, which is essential for proper microridge formation (Raman et al., 2016).

MyTH4-FERM myosins

Class VII myosins are monomeric and have a high duty ratio, making them ideal for tension generation and maintenance (Sakai et al., 2015; Henn and De La Cruz, 2005; Inoue and Ikebe, 2003). Aside from the motor domain, class VII myosins have five IQ domains in their neck and an SH3 domain flanked by two MyTH4-FERM domains in their tail. Class VII myosins are autoinhibited by interactions between the tail and head domains which are relieved by Ca^{2+}, possibly through calmodulin binding to the first IQ domain (Sakai et al., 2015), or through interactions with tail-binding proteins (Yang et al., 2009; El-Amraoui et al., 2002). The localization of Myo7a to the tips of filopodia is dependent on forced dimerization (Sakai et al., 2015, 2011; Arthur et al., 2019) and can be induced by cargo binding (Sakai et al., 2011), suggesting that class VII myosins could function as a cargo-dependent oligomers, similar to Myo6.

Class VII myosin Myo7a localizes to multiple locations within stereocilia. Myo7a is present in the upper tip-link density (UTLD) where it anchors tip-links to actin through its binding partners SANS and Harmonin b (Adato et al., 2005; Boëda et al., 2002; Yan et al., 2010; Bahloul et al., 2010). Tip-links are tethers between stereocilia, composed of trans-heterophilic binding partners cadherin-23 and protocadherin-15 (Kazmierczak et al., 2007), that anchor in a lower tip-link density, which contains the transmembrane channels required for mechanotransduction (Beurg et al., 2009). Myo7a can also be found in stereocilia ankle-links (Morgan et al., 2016; Michalski et al., 2007), tethers that interconnect stereocilia at the base of protrusions. *Myo7a* KO leads to

the mislocalization of stereocilia tip- and ankle-link complex components (Boëda et al., 2002; Michalski et al., 2007) and loss of the third row of stereocilia (Self et al., 1998; Li et al., 2020), which ultimately result in deafness (Well et al., 1995). Interestingly, there are two isoforms of Myo7a that are differentially expressed in the inner ear, a canonical isoform that contains an 11 AA N-terminal extension and a short isoform that lacks this extension (Li et al., 2020). In a mouse KO of the canonical Myo7a isoform, the mechano-electrical transduction (MET) channel resting open probability and current onset were significantly reduced in inner hair cells (IHCs), suggesting that Myo7a creates tension in IHC tip-links (Li et al., 2020). If the Myo7a motor generates tension between the tips of stereocilia, differential expression of Myo7a isoforms among hair cells may explain the differential MET properties observed among hair cell populations (Li et al., 2020).

The role of Myo7b in microvilli is highly analogous to that of Myo7a in stereocilia. Myo7b localizes to the distal tips of microvilli where it interacts with intracellular components of the intermicrovillar adhesion complex (IMAC) (Crawley et al., 2014b; Chen et al., 2001). Myo7b anchors IMACs to actin through interactions with Harmonin a and ANKS4B which are analogous to the interactions of Myo7a with Harmonin b and USH1G in stereocilia (Li et al., 2016). In *Myo7b* KD intestinal epithelial cells, components of the IMAC are mislocalized along the length of the microvillus rather than exclusive to the tip (Weck et al., 2016). The sides of microvilli in these cells have aberrant connections to the apical cell membrane, and do not form an organized brush border (Weck et al., 2016). These analogous tip complexes, the IMAC (microvilli) and the UTLD (stereocilia), can both form high-density condensates via liquid-liquid phase separation (LLPS) (He et al., 2019). Pathological mutations in *Myo7* reduce the LLPS capacity of these complexes (He et al., 2019), suggesting an important role for protein density in the function of the IMAC and UTLD.

Class XV myosin Myo15 is the largest member of the myosin superfamily to date, containing 3530 amino acids (Liang et al., 1999). Similar to myosin VII, the tail domain of Myo15

contains MyTH4, SH3, and FERM domains (Liang et al., 1999). The IQ domains of Myo15 bind smooth muscle RLC and ELC in addition to calmoldulin (Bird et al., 2014), although it is unclear how these factors may work to regulate Myo15 function *in vivo*. The Myo15 motor has a high duty ratio that suggests it functions as a transporter (Bird et al., 2014).

Myo15a localizes to the tips of stereocilia (Belyantseva et al., 2003), and is required for the localization of stereocilia tip proteins Eps8 and whirlin, both of which are important regulators of stereocilia length (Belyantseva et al., 2005; Manor et al., 2011). Stereocilia in *Myo15* null mice are dramatically shortened compared to WT, and mutations in both this gene and the human ortholog are associated with deafness (Fang et al., 2015; Probst et al., 1998; Wang et al., 1998). One exceptional feature of the Myo15 protein is a proline-rich 133kDa N-terminal extension, which can be eliminated by alternative splicing of exon 2 (Liang et al., 1999). Both protein isoforms are expressed in hair cells (Liang et al., 1999; Fang et al., 2015), but preferentially localize to distinct rows of stereocilia in IHCs. The longer protein isoform localizes to the shorter, second and third rows, while the short isoform localizes to the tallest row (Fang et al., 2015). In long isoform mutants, stereocilia development and localization of Eps8 and whirlin are largely normal, although mechanotransduction in the lower rows of stereocilia is imparied (Fang et al., 2015). Despite normal development in long isoform mutants, the shorter rows of stereocilia, to which the long isoform typically localizes, eventually adopt an abnormal tip morphology and are resorbed (Fang et al., 2015).

The many variants among proteins of the myosin superfamily are able to use their force-generating motor activity for diverse functions, from transporting essential protein components, to anchoring the cell membrane to the cytoskeletal core of protrusions. The contributions of NMII to protrusion morphogenesis are particularly interesting, as they suggest an important role for physical forces in this process. Although many myosin functions have been discovered in the morphogenesis of microvilli and stereocilia, the role of NMII in formation and maintenance of

microridges is ambiguous. In this dissertation, I investigate the mechanism of microridge morphogenesis and the role of NMII contraction in this process by directly observing microridge development on live zebrafish larvae.

References

Adato, A., V. Michel, Y. Kikkawa, J. Reiners, K.N. Alagramam, D. Weil, H. Yonekawa, U. Wolfrum, A. El-Amraoui, and C. Petit. 2005. Interactions in the network of Usher syndrome type 1 proteins. *Hum. Mol. Genet.* 14:347–356.

Aguilar-Aragon, M., G. Fletcher, and B.J. Thompson. 2020. The cytoskeletal motor proteins Dynein and MyoV direct apical transport of Crumbs. *Dev. Biol.* 459:126–137.

Altman, D., H.L. Sweeney, and J.A. Spudich. 2004. The mechanism of myosin VI translocation and its load-induced anchoring. *Cell*. 116:737–749.

Arthur, A.L., L.D. Songster, H. Sirkia, A. Bhattacharya, C. Kikuti, F.P. Borrega, A. Houdusse, and M.A. Titus. 2019. Optimized filopodia formation requires myosin tail domain cooperation. *Proc. Natl. Acad. Sci. U. S. A.* 116:22196–22204.

Avraham, K.B., T. Hasson, K.P. Steel, D.M. Kingsley, L.B. Russell, M.S. Mooseker, N.G. Copeland, and N.A. Jenkins. 1995. The mouse Snell's waltzer deafness gene encodes an unconventional myosin required for structural integrity of inner ear hair cells. *Nat. Genet.* 11:369–375.

Bahloul, A., V. Michel, J.-P. Hardelin, S. Nouaille, S. Hoos, A. Houdusse, P. England, and C. Petit. 2010. Cadherin-23, myosin VIIa and harmonin, encoded by Usher syndrome type I genes, form a ternary complex and interact with membrane phospholipids. *Hum. Mol. Genet.* 19:3557–3565.

Belyantseva, I.A., E.T. Boger, and T.B. Friedman. 2003. Myosin XVa localizes to the tips of inner ear sensory cell stereocilia and is essential for staircase formation of the hair bundle. *Proc. Natl. Acad. Sci. U. S. A.* 100:13958–13963.

Belyantseva, I.A., E.T. Boger, S. Naz, G.I. Frolenkov, J.R. Sellers, Z.M. Ahmed, A.J. Griffith, and T.B. Friedman. 2005. Myosin-XVa is required for tip localization of whirlin and differential elongation of hair-cell stereocilia. *Nat. Cell Biol.* 7:148–156.

Benesh, A.E., R. Nambiar, R.E. McConnell, S. Mao, D.L. Tabb, and M.J. Tyska. 2010. Differential localization and dynamics of class I myosins in the enterocyte microvillus. *Mol. Biol. Cell*. 21:970–978.

Bereiter-Hahn, J., M. Osborn, K. Weber, and M. Vöth. 1979. Filament organization and formation of microridges at the surface of fish epidermis. *J. Ultrastruct. Res.* 69:316–330.

Beurg, M., R. Fettiplace, J.-H. Nam, and A.J. Ricci. 2009. Localization of inner hair cell mechanotransducer channels using high-speed calcium imaging. *Nat. Neurosci.* 12:553–558.

Bird, J.E., Y. Takagi, N. Billington, M.-P. Strub, J.R. Sellers, and T.B. Friedman. 2014. Chaperone-enhanced purification of unconventional myosin 15, a molecular motor specialized for stereocilia protein trafficking. *Proc. Natl. Acad. Sci. U. S. A.* 111:12390–12395.

Blalock, T.D., S.J. Spurr-Michaud, A.S. Tisdale, S.R. Heimer, M.S. Gilmore, V. Ramesh, and I.K. Gipson. 2007. Functions of MUC16 in corneal epithelial cells. *Invest. Ophthalmol. Vis. Sci.* 48:4509–4518.

Blümcke, S., and K. Morgenroth Jr. 1967. The stereo ultrastructure of the external and internal surface of the cornea. *J. Ultrastruct. Res.* 18:502–518.

Boëda, B., A. El-Amraoui, A. Bahloul, R. Goodyear, L. Daviet, S. Blanchard, I. Perfettini, K.R. Fath, S. Shorte, J. Reiners, A. Houdusse, P. Legrain, U. Wolfrum, G. Richardson, and C. Petit. 2002. Myosin VIIa, harmonin and cadherin 23, three Usher I gene products that

cooperate to shape the sensory hair cell bundle. *EMBO J.* 21:6689–6699.

Brown, J.W., and C.J. McKnight. 2010. Molecular model of the microvillar cytoskeleton and organization of the brush border. *PLoS One*. 5:e9406.

Chen, Z.Y., T. Hasson, D.S. Zhang, B.J. Schwender, B.H. Derfler, M.S. Mooseker, and D.P. Corey. 2001. Myosin-VIIb, a novel unconventional myosin, is a constituent of microvilli in transporting epithelia. *Genomics*. 72:285–296.

Chinowsky, C.R., J.A. Pinette, L.M. Meenderink, K.S. Lau, and M.J. Tyska. 2020. Non-muscle myosin-2 contractility-dependent actin turnover limits the length of epithelial microvilli. *MBoC*. mbc.E20–09–0582.

Crawford, B.D., C.A. Henry, T.A. Clason, A.L. Becker, and M.B. Hille. 2003. Activity and distribution of paxillin, focal adhesion kinase, and cadherin indicate cooperative roles during zebrafish morphogenesis. *Mol. Biol. Cell*. 14:3065–3081.

Crawley, S.W., M.S. Mooseker, and M.J. Tyska. 2014a. Shaping the intestinal brush border. *J. Cell Biol.* 207:441–451.

Crawley, S.W., D.A. Shifrin Jr, N.E. Grega-Larson, R.E. McConnell, A.E. Benesh, S. Mao, Y. Zheng, Q.Y. Zheng, K.T. Nam, B.A. Millis, B. Kachar, and M.J. Tyska. 2014b. Intestinal brush border assembly driven by protocadherin-based intermicrovillar adhesion. *Cell*. 157:433–446.

Dantas, V.G.L., M.H. Raval, A. Ballesteros, R. Cui, L.K. Gunther, G.L. Yamamoto, L.U. Alves, A.S. Bueno, K. Lezirovitz, S. Pirana, B.C.A. Mendes, C.M. Yengo, B. Kachar, and R.C. Mingroni-Netto. 2018. Characterization of a novel MYO3A missense mutation associated with a dominant form of late onset hearing loss. *Sci. Rep.* 8:8706.

Davidson, G.P., E. Cutz, J.R. Hamilton, and D.G. Gall. 1978. Familial enteropathy: a syndrome of protracted diarrhea from birth, failure to thrive, and hypoplastic villus atrophy. *Gastroenterology*. 75:783–790.

De La Cruz, E.M., A.L. Wells, S.S. Rosenfeld, E.M. Ostap, and H.L. Sweeney. 1999. The kinetic mechanism of myosin V. *Proc. Natl. Acad. Sci. U. S. A.* 96:13726–13731.

Depasquale, J.A. 2018. Actin Microridges. *Anat. Rec.* . 301:2037–2050.

Dormans, J.A., and M.J. van Logten. 1982. The effects of ophthalmic preservatives on corneal epithelium of the rabbit: a scanning electron microscopical study. *Toxicol. Appl. Pharmacol.* 62:251–261.

Dosé, A.C., S. Ananthanarayanan, J.E. Moore, B. Burnside, and C.M. Yengo. 2007. Kinetic mechanism of human myosin IIIA. *J. Biol. Chem.* 282:216–231.

Dosé, A.C., and B. Burnside. 2000. Cloning and chromosomal localization of a human class III myosin. *Genomics*. 67:333–342.

Dosé, A.C., D.W. Hillman, C. Wong, L. Sohlberg, J. Lin-Jones, and B. Burnside. 2003. Myo3A, one of two class III myosin genes expressed in vertebrate retina, is localized to the calycal processes of rod and cone photoreceptors and is expressed in the sacculus. *Mol. Biol. Cell*. 14:1058–1073.

Ebrahim, S., M.R. Avenarius, M. 'hamed Grati, J.F. Krey, A.M. Windsor, A.D. Sousa, A. Ballesteros, R. Cui, B.A. Millis, F.T. Salles, M.A. Baird, M.W. Davidson, S.M. Jones, D. Choi, L. Dong, M.H. Raval, C.M. Yengo, P.G. Barr-Gillespie, and B. Kachar. 2016. Stereocilia-staircase spacing is influenced by myosin III motors and their cargos espin-1 and espin-like. *Nat. Commun.* 7:10833.

El-Amraoui, A., J.-S. Schonn, P. Küssel-Andermann, S. Blanchard, C. Desnos, J.-P. Henry, U. Wolfrum, F. Darchen, and C. Petit. 2002. MyRIP, a novel Rab effector, enables myosin VIIa recruitment to retinal melanosomes. *EMBO Rep.* 3:463–470.

Engevik, A.C., I. Kaji, M.M. Postema, J.J. Faust, A.R. Meyer, J.A. Williams, G.N. Fitz, M.J. Tyska, J.M. Wilson, and J.R. Goldenring. 2019. Loss of myosin Vb promotes apical bulk endocytosis in neonatal enterocytes. *J. Cell Biol.* 218:3647–3662.

Fahrenbach, W.H., and D.D. Knutson. 1975. Surface adaptations of the vertebrate epidermis to friction. *J. Invest. Dermatol.* 65:39–44.

Fang, Q., A.A. Indzhykulian, M. Mustapha, G.P. Riordan, D.F. Dolan, T.B. Friedman, I.A. Belyantseva, G.I. Frolenkov, S.A. Camper, and J.E. Bird. 2015. The 133-kDa N-terminal domain enables myosin 15 to maintain mechanotransducing stereocilia and is essential for hearing. *Elife*. 4. doi:10.7554/eLife.08627.

García, J.A., A.G. Yee, P.G. Gillespie, and D.P. Corey. 1998. Localization of myosin-Ibeta near both ends of tip links in frog saccular hair cells. *J. Neurosci.* 18:8637–8647.

Gardini, L., S.M. Heissler, C. Arbore, Y. Yang, J.R. Sellers, F.S. Pavone, and M. Capitanio. 2018. Dissecting myosin-5B mechanosensitivity and calcium regulation at the single molecule level. *Nat. Commun.* 9:2844.

Gillespie, P.G., J.P. Albanesi, M. Bahler, W.M. Bement, J.S. Berg, D.R. Burgess, B. Burnside, R.E. Cheney, D.P. Corey, E. Coudrier, P. de Lanerolle, J.A. Hammer, T. Hasson, J.R. Holt, A.J. Hudspeth, M. Ikebe, J. Kendrick-Jones, E.D. Korn, R. Li, J.A. Mercer, R.A. Milligan, M.S. Mooseker, E.M. Ostap, C. Petit, T.D. Pollard, J.R. Sellers, T. Soldati, and M.A. Titus. 2001. Myosin-I nomenclature. *J. Cell Biol.* 155:703–704.

Goldstein, B., and I.G. Macara. 2007. The PAR proteins: fundamental players in animal cell polarization. *Dev. Cell*. 13:609–622.

Greenberg, M.J., T. Lin, Y.E. Goldman, H. Shuman, and E.M. Ostap. 2012. Myosin IC generates power over a range of loads via a new tension-sensing mechanism. *Proc. Natl. Acad. Sci. U. S. A.* 109:E2433–40.

Greenberg, M.J., T. Lin, H. Shuman, and E.M. Ostap. 2015. Mechanochemical tuning of myosin-I by the N-terminal region. *Proc. Natl. Acad. Sci. U. S. A.* 112:E3337–44.

Hammer, J.A., 3rd, and J.R. Sellers. 2011. Walking to work: roles for class V myosins as cargo transporters. *Nat. Rev. Mol. Cell Biol.* 13:13–26.

Hasson, T., and M.S. Mooseker. 1994. Porcine myosin-VI: characterization of a new mammalian unconventional myosin. *J. Cell Biol.* 127:425–440.

Hegan, P.S., H. Giral, M. Levi, and M.S. Mooseker. 2012. Myosin VI is required for maintenance of brush border structure, composition, and membrane trafficking functions in the intestinal epithelial cell. *Cytoskeleton* . 69:235–251.

Heintzelman, M.B., T. Hasson, and M.S. Mooseker. 1994. Multiple unconventional myosin domains of the intestinal brush border cytoskeleton. *J. Cell Sci.* 107 (Pt 12):3535–3543.

Henn, A., and E.M. De La Cruz. 2005. Vertebrate myosin VIIb is a high duty ratio motor adapted for generating and maintaining tension. *J. Biol. Chem.* 280:39665–39676.

Hertzano, R., E. Shalit, A.K. Rzadzinska, A.A. Dror, L. Song, U. Ron, J.T. Tan, A.S. Shitrit, H. Fuchs, T. Hasson, N. Ben-Tal, H.L. Sweeney, M.H. de Angelis, K.P. Steel, and K.B. Avraham. 2008. A Myo6 mutation destroys coordination between the myosin heads,

revealing new functions of myosin VI in the stereocilia of mammalian inner ear hair cells. *PLoS Genet.* 4:e1000207.

He, Y., J. Li, and M. Zhang. 2019. Myosin VII, USH1C, and ANKS4B or USH1G Together Form Condensed Molecular Assembly via Liquid-Liquid Phase Separation. *Cell Rep.* 29:974–986.e4.

Hokanson, D.E., J.M. Laakso, T. Lin, D. Sept, and E.M. Ostap. 2006. Myo1c binds phosphoinositides through a putative pleckstrin homology domain. *Mol. Biol. Cell*. 17:4856–4865.

Holt, J.R., S.K.H. Gillespie, D.W. Provance, K. Shah, K.M. Shokat, D.P. Corey, J.A. Mercer, and P.G. Gillespie. 2002. A chemical-genetic strategy implicates myosin-1c in adaptation by hair cells. *Cell*. 108:371–381.

Howe, C.L., and M.S. Mooseker. 1983. Characterization of the 110-kdalton actin-calmodulin-, and membrane-binding protein from microvilli of intestinal epithelial cells. *J. Cell Biol.* 97:974–985.

Inaba, Y., V. Chauhan, A.P. van Loon, L.S. Choudhury, and A. Sagasti. 2020. Keratins and the plakin family cytolinker proteins control the length of epithelial microridge protrusions. *Elife*. 9. doi:10.7554/eLife.58149.

Inoue, A., and M. Ikebe. 2003. Characterization of the motor activity of mammalian myosin VIIA. *J. Biol. Chem.* 278:5478–5487.

de Jonge, J.J., C. Batters, T. O'Loughlin, S.D. Arden, and F. Buss. 2019. The MYO6 interactome: selective motor-cargo complexes for diverse cellular processes. *FEBS Lett.* 593:1494–1507.

Jontes, J.D., R.A. Milligan, T.D. Pollard, and E.M. Ostap. 1997. Kinetic characterization of brush border myosin-I ATPase. *Proc. Natl. Acad. Sci. U. S. A.* 94:14332–14337.

Kazmierczak, P., H. Sakaguchi, J. Tokita, E.M. Wilson-Kubalek, R.A. Milligan, U. Müller, and B. Kachar. 2007. Cadherin 23 and protocadherin 15 interact to form tip-link filaments in sensory hair cells. *Nature*. 449:87–91.

Knowles, B.C., J.T. Roland, M. Krishnan, M.J. Tyska, L.A. Lapierre, P.S. Dickman, J.R. Goldenring, and M.D. Shub. 2014. Myosin Vb uncoupling from RAB8A and RAB11A elicits microvillus inclusion disease. *J. Clin. Invest.* 124:2947–2962.

Koide, H., T. Kinoshita, Y. Tanaka, S. 'ichiro Tanaka, N. Nagura, G. Meyer zu Hörste, A. Miyagi, and T. Ando. 2006. Identification of the single specific IQ motif of myosin V from which calmodulin dissociates in the presence of Ca2+. *Biochemistry*. 45:11598–11604.

Komaba, S., A. Inoue, S. Maruta, H. Hosoya, and M. Ikebe. 2003. Determination of human myosin III as a motor protein having a protein kinase activity. *J. Biol. Chem.* 278:21352–21360.

Krendel, M., E.K. Osterweil, and M.S. Mooseker. 2007. Myosin 1E interacts with synaptojanin-1 and dynamin and is involved in endocytosis. *FEBS Lett.* 581:644–650.

Lalwani, A.K., G. Atkin, Y. Li, J.Y. Lee, D.E. Hillman, and A.N. Mhatre. 2008. Localization in stereocilia, plasma membrane, and mitochondria suggests diverse roles for NMHC-IIa within cochlear hair cells. *Brain Res.* 1197:13–22.

Lam, P.-Y., S. Mangos, J.M. Green, J. Reiser, and A. Huttenlocher. 2015. In vivo imaging and characterization of actin microridges. *PLoS One*. 10:e0115639.

Lelli, A., V. Michel, J. Boutet de Monvel, M. Cortese, M. Bosch-Grau, A. Aghaie, I. Perfettini, T.

Dupont, P. Avan, A. El-Amraoui, and C. Petit. 2016. Class III myosins shape the auditory hair bundles by limiting microvilli and stereocilia growth. *J. Cell Biol.* 212:231–244.

Les Erickson, F., A.C. Corsa, A.C. Dose, and B. Burnside. 2003. Localization of a class III myosin to filopodia tips in transfected HeLa cells requires an actin-binding site in its tail domain. *Mol. Biol. Cell*. 14:4173–4180.

Liang, Y., A. Wang, I.A. Belyantseva, D.W. Anderson, F.J. Probst, T.D. Barber, W. Miller, J.W. Touchman, L. Jin, S.L. Sullivan, J.R. Sellers, S.A. Camper, R.V. Lloyd, B. Kachar, T.B. Friedman, and R.A. Fridell. 1999. Characterization of the human and mouse unconventional myosin XV genes responsible for hereditary deafness DFNB3 and shaker 2. *Genomics*. 61:243–258.

Li, J., Y. He, Q. Lu, and M. Zhang. 2016. Mechanistic Basis of Organization of the Harmonin/USH1C-Mediated Brush Border Microvilli Tip-Link Complex. *Dev. Cell*. 36:179–189.

Li, S., A. Mecca, J. Kim, G.A. Caprara, E.L. Wagner, T.-T. Du, L. Petrov, W. Xu, R. Cui, I.T. Rebustini, B. Kachar, A.W. Peng, and J.-B. Shin. 2020. Myosin-VIIa is expressed in multiple isoforms and essential for tensioning the hair cell mechanotransduction complex. *Nat. Commun.* 11:2066.

Liu, J., D.W. Taylor, E.B. Krementsova, K.M. Trybus, and K.A. Taylor. 2006. Three-dimensional structure of the myosin V inhibited state by cryoelectron tomography. *Nature*. 442:208–211.

Li, X.-D., R. Ikebe, and M. Ikebe. 2005. Activation of myosin Va function by melanophilin, a specific docking partner of myosin Va. *J. Biol. Chem.* 280:17815–17822.

Lu, Z., M. Shen, Y. Cao, H.-M. Zhang, L.-L. Yao, and X.-D. Li. 2012. Calmodulin bound to the first

IQ motif is responsible for calcium-dependent regulation of myosin 5a. *J. Biol. Chem.* 287:16530–16540.

Manor, U., A. Disanza, M. 'hamed Grati, L. Andrade, H. Lin, P.P. Di Fiore, G. Scita, and B. Kachar. 2011. Regulation of stereocilia length by myosin XVa and whirlin depends on the actin-regulatory protein Eps8. *Curr. Biol.* 21:167–172.

Mazerik, J.N., and M.J. Tyska. 2012. Myosin-1A targets to microvilli using multiple membrane binding motifs in the tail homology 1 (TH1) domain. *J. Biol. Chem.* 287:13104–13115.

McIntosh, B.B., and E.M. Ostap. 2016. Myosin-I molecular motors at a glance. *J. Cell Sci.* 129:2689–2695.

Meenderink, L.M., I.M. Gaeta, M.M. Postema, C.S. Cencer, C.R. Chinowsky, E.S. Krystofiak, B.A. Millis, and M.J. Tyska. 2019. Actin Dynamics Drive Microvillar Motility and Clustering during Brush Border Assembly. *Dev. Cell*. 50:545–556.e4.

Melchionda, S., N. Ahituv, L. Bisceglia, T. Sobe, F. Glaser, R. Rabionet, M.L. Arbones, A. Notarangelo, E. Di Iorio, M. Carella, L. Zelante, X. Estivill, K.B. Avraham, and P. Gasparini. 2001. MYO6, the Human Homologue of the Gene Responsible for Deafness in Snell's Waltzer Mice, Is Mutated in Autosomal Dominant Nonsyndromic Hearing Loss. *Am. J. Hum. Genet.* 69:635–640.

Ménétrey, J., A. Bahloul, A.L. Wells, C.M. Yengo, C.A. Morris, H.L. Sweeney, and A. Houdusse. 2005. The structure of the myosin VI motor reveals the mechanism of directionality reversal. *Nature*. 435:779–785.

Merritt, R.C., U. Manor, F.T. Salles, M. 'hamed Grati, A.C. Dose, W.C. Unrath, O.A. Quintero, C.M. Yengo, and B. Kachar. 2012. Myosin IIIB uses an actin-binding motif in its espin-1 cargo

to reach the tips of actin protrusions. *Curr. Biol.* 22:320–325.

Michalski, N., V. Michel, A. Bahloul, G. Lefèvre, J. Barral, H. Yagi, S. Chardenoux, D. Weil, P. Martin, J.-P. Hardelin, M. Sato, and C. Petit. 2007. Molecular characterization of the ankle-link complex in cochlear hair cells and its role in the hair bundle functioning. *J. Neurosci.* 27:6478–6488.

Mooseker, M.S., and L.G. Tilney. 1975. Organization of an actin filament-membrane complex. Filament polarity and membrane attachment in the microvilli of intestinal epithelial cells. *J. Cell Biol.* 67:725–743.

Morgan, C.P., J.F. Krey, M. 'hamed Grati, B. Zhao, S. Fallen, A. Kannan-Sundhari, X.Z. Liu, D. Choi, U. Müller, and P.G. Barr-Gillespie. 2016. PDZD7-MYO7A complex identified in enriched stereocilia membranes. *Elife*. 5. doi:10.7554/eLife.18312.

Nambiar, R., R.E. McConnell, and M.J. Tyska. 2009. Control of cell membrane tension by myosin-I. *Proc. Natl. Acad. Sci. U. S. A.* 106:11972–11977.

Nambiar, R., R.E. McConnell, and M.J. Tyska. 2010. Myosin motor function: the ins and outs of actin-based membrane protrusions. *Cell. Mol. Life Sci.* 67:1239–1254.

Nguyen, H., and H. Higuchi. 2005. Motility of myosin V regulated by the dissociation of single calmodulin. *Nat. Struct. Mol. Biol.* 12:127–132.

Pinto, C.S., A. Khandekar, R. Bhavna, P. Kiesel, G. Pigino, and M. Sonawane. 2019. Microridges are apical epithelial projections formed of F-actin networks that organize the glycan layer. *Sci. Rep.* 9:12191.

Probst, F.J., R.A. Fridell, Y. Raphael, T.L. Saunders, A. Wang, Y. Liang, R.J. Morell, J.W.

Touchman, R.H. Lyons, K. Noben-Trauth, T.B. Friedman, and S.A. Camper. 1998. Correction of deafness in shaker-2 mice by an unconventional myosin in a BAC transgene. *Science*. 280:1444–1447.

Quintero, O.A., J.E. Moore, W.C. Unrath, U. Manor, F.T. Salles, M. 'hamed Grati, B. Kachar, and C.M. Yengo. 2010. Intermolecular autophosphorylation regulates myosin IIIa activity and localization in parallel actin bundles. *J. Biol. Chem.* 285:35770–35782.

Quintero, O.A., W.C. Unrath, S.M. Stevens Jr, U. Manor, B. Kachar, and C.M. Yengo. 2013. Myosin 3A kinase activity is regulated by phosphorylation of the kinase domain activation loop. *J. Biol. Chem.* 288:37126–37137.

Rai, A.K., N. Srivastava, A.K. Nigam, U. Kumari, S. Mittal, and A.K. Mittal. 2012. Healing of cutaneous wounds in a freshwater teleost, Labeo rohita: scanning electron microscopical investigation. *Microsc. Res. Tech.* 75:890–897.

Raman, R., I. Damle, R. Rote, S. Banerjee, C. Dingare, and M. Sonawane. 2016. aPKC regulates apical localization of Lgl to restrict elongation of microridges in developing zebrafish epidermis. *Nat. Commun.* 7:11643.

Richardson, R., M. Metzger, P. Knyphausen, T. Ramezani, K. Slanchev, C. Kraus, E. Schmelzer, and M. Hammerschmidt. 2016. Re-epithelialization of cutaneous wounds in adult zebrafish combines mechanisms of wound closure in embryonic and adult mammals. *Development*. 143:2077–2088.

Rogez, B., L. Würthner, A.B. Petrova, F.B. Zierhut, D. Saczko-Brack, M.-A. Huergo, C. Batters, E. Frey, and C. Veigel. 2019. Reconstitution reveals how myosin-VI self-organises to generate a dynamic mechanism of membrane sculpting. *Nat. Commun.* 10:3305.

Rottner, K., and M. Schaks. 2019. Assembling actin filaments for protrusion. *Curr. Opin. Cell Biol.* 56:53–63.

Ruemmele, F.M., J. Schmitz, and O. Goulet. 2006. Microvillous inclusion disease (microvillous atrophy). *Orphanet J. Rare Dis.* 1:22.

Rzadzinska, A.K., M.E. Schneider, C. Davies, G.P. Riordan, and B. Kachar. 2004. An actin molecular treadmill and myosins maintain stereocilia functional architecture and self-renewal. *J. Cell Biol.* 164:887–897.

Rzadzinska, A., M. Schneider, K. Noben-Trauth, J.R. Bartles, and B. Kachar. 2005. Balanced levels of Espin are critical for stereociliary growth and length maintenance. *Cell Motil. Cytoskeleton*. 62:157–165.

Sakai, T., H.S. Jung, O. Sato, M.D. Yamada, D.-J. You, R. Ikebe, and M. Ikebe. 2015. Structure and Regulation of the Movement of Human Myosin VIIA. *J. Biol. Chem.* 290:17587–17598.

Sakai, T., N. Umeki, R. Ikebe, and M. Ikebe. 2011. Cargo binding activates myosin VIIA motor function in cells. *Proc. Natl. Acad. Sci. U. S. A.* 108:7028–7033.

Sakurai, K., M. Hirata, H. Yamaguchi, Y. Nakamura, and K. Fukami. 2011. Phospholipase Cδ3 is a novel binding partner of myosin VI and functions as anchoring of myosin VI on plasma membrane. *Adv. Enzyme Regul.* 51:171–181.

Salles, F.T., R.C. Merritt Jr, U. Manor, G.W. Dougherty, A.D. Sousa, J.E. Moore, C.M. Yengo, A.C. Dosé, and B. Kachar. 2009. Myosin IIIa boosts elongation of stereocilia by transporting espin 1 to the plus ends of actin filaments. *Nat. Cell Biol.* 11:443–450.

Schliwa, M. 1975. Cytoarchitecture of surface layer cells of the teleost epidermis. *J. Ultrastruct.*

Res. 52:377–386.

Schneider, M.E., A.C. Dosé, F.T. Salles, W. Chang, F.L. Erickson, B. Burnside, and B. Kachar. 2006. A new compartment at stereocilia tips defined by spatial and temporal patterns of myosin IIIa expression. *J. Neurosci.* 26:10243–10252.

Seiler, C., O. Ben-David, S. Sidi, O. Hendrich, A. Rusch, B. Burnside, K.B. Avraham, and T. Nicolson. 2004. Myosin VI is required for structural integrity of the apical surface of sensory hair cells in zebrafish. *Dev. Biol.* 272:328–338.

Seki, Y., Y. Miyasaka, S. Suzuki, K. Wada, S.P. Yasuda, K. Matsuoka, Y. Ohshiba, K. Endo, R. Ishii, H. Shitara, S.-I. Kitajiri, N. Nakagata, H. Takebayashi, and Y. Kikkawa. 2017. A novel splice site mutation of myosin VI in mice leads to stereociliary fusion caused by disruption of actin networks in the apical region of inner ear hair cells. *PLoS One*. 12:e0183477.

Self, T., M. Mahony, J. Fleming, J. Walsh, S.D. Brown, and K.P. Steel. 1998. Shaker-1 mutations reveal roles for myosin VIIA in both development and function of cochlear hair cells. *Development*. 125:557–566.

Sonal, J. Sidhaye, M. Phatak, S. Banerjee, A. Mulay, O. Deshpande, S. Bhide, T. Jacob, I. Gehring, C. Nuesslein-Volhard, and M. Sonawane. 2014. Myosin Vb mediated plasma membrane homeostasis regulates peridermal cell size and maintains tissue homeostasis in the zebrafish epidermis. *PLoS Genet.* 10:e1004614.

Sperry, D.G., and R.J. Wassersug. 1976. A proposed function for microridges on epithelial cells. *Anat. Rec.* 185:253–257.

Spudich, G., M.V. Chibalina, J.S.-Y. Au, S.D. Arden, F. Buss, and J. Kendrick-Jones. 2007. Myosin VI targeting to clathrin-coated structures and dimerization is mediated by binding to

Disabled-2 and PtdIns(4,5)P2. *Nat. Cell Biol.* 9:176–183.

Stauffer, E.A., J.D. Scarborough, M. Hirono, E.D. Miller, K. Shah, J.A. Mercer, J.R. Holt, and P.G. Gillespie. 2005. Fast adaptation in vestibular hair cells requires myosin-1c activity. *Neuron*. 47:541–553.

Steyger, P.S., P.G. Gillespie, and R.A. Baird. 1998. Myosin Ibeta is located at tip link anchors in vestibular hair bundles. *J. Neurosci.* 18:4603–4615.

Stöffler, H.E., and M. Bähler. 1998. The ATPase activity of Myr3, a rat myosin I, is allosterically inhibited by its own tail domain and by Ca2+ binding to its light chain calmodulin. *J. Biol. Chem.* 273:14605–14611.

Streb, H., R.F. Irvine, M.J. Berridge, and I. Schulz. 1983. Release of Ca2+ from a nonmitochondrial intracellular store in pancreatic acinar cells by inositol-1,4,5-trisphosphate. *Nature*. 306:67–69.

Thirumurugan, K., T. Sakamoto, J.A. Hammer 3rd, J.R. Sellers, and P.J. Knight. 2006. The cargo-binding domain regulates structure and activity of myosin 5. *Nature*. 442:212–215.

Trybus, K.M., M.I. Gushchin, H. Lui, L. Hazelwood, E.B. Krementsova, N. Volkmann, and D. Hanein. 2007. Effect of calcium on calmodulin bound to the IQ motifs of myosin V. *J. Biol. Chem.* 282:23316–23325.

Tyska, M.J., A.T. Mackey, J.-D. Huang, N.G. Copeland, N.A. Jenkins, and M.S. Mooseker. 2005. Myosin-1a is critical for normal brush border structure and composition. *Mol. Biol. Cell*. 16:2443–2457.

Uehara, K., M. Miyoshi, and S. Miyoshi. 1990. Actin filaments in microridges of the oral mucosal

epithelium in the carp Cyprinus carpio. *Cell Tissue Res.* 261:419–422.

Uehara, K., M. Miyoshi, and S. Miyoshi. 1991. Cytoskeleton in microridges of the oral mucosal epithelium in the carp, Cyprinus carpio. *Anat. Rec.* 230:164–168.

Verma, N., U. Kumari, S. Mittal, and A.K. Mittal. 2017. Scanning electron microscope investigation on the process of healing of skin wounds in Cirrhinus mrigala. *Microsc. Res. Tech.* 80:1205–1214.

Verver, E.J.J., V. Topsakal, H.P.M. Kunst, P.L.M. Huygen, P.G. Heller, N. Pujol-Moix, A. Savoia, M. Benazzo, T. Fierro, W. Grolman, P. Gresele, and A. Pecci. 2016. Nonmuscle Myosin Heavy Chain IIA Mutation Predicts Severity and Progression of Sensorineural Hearing Loss in Patients With MYH9-Related Disease. *Ear Hear.* 37:112–120.

Walsh, T., V. Walsh, S. Vreugde, R. Hertzano, H. Shahin, S. Haika, M.K. Lee, M. Kanaan, M.-C. King, and K.B. Avraham. 2002. From flies' eyes to our ears: mutations in a human class III myosin cause progressive nonsyndromic hearing loss DFNB30. *Proc. Natl. Acad. Sci. U. S. A.* 99:7518–7523.

Wang, A., Y. Liang, R.A. Fridell, F.J. Probst, E.R. Wilcox, J.W. Touchman, C.C. Morton, R.J. Morell, K. Noben-Trauth, S.A. Camper, and T.B. Friedman. 1998. Association of unconventional myosin MYO15 mutations with human nonsyndromic deafness DFNB3. *Science*. 280:1447–1451.

Wang, F., K. Thirumurugan, W.F. Stafford, J.A. Hammer 3rd, P.J. Knight, and J.R. Sellers. 2004. Regulated conformation of myosin V. *J. Biol. Chem.* 279:2333–2336.

Wassersug, R.J., and R.K. Johnson. 2009. A remarkable pyloric caecum in the evermannellid genus Coccorella with notes on gut structure and function in alepisauroid fishes (Pisces,

Myctophiformes). *J. Zool.* 179:273–289.

Weck, M.L., S.W. Crawley, C.R. Stone, and M.J. Tyska. 2016. Myosin-7b Promotes Distal Tip Localization of the Intermicrovillar Adhesion Complex. *Curr. Biol.* 26:2717–2728.

Weis, V.G., B.C. Knowles, E. Choi, A.E. Goldstein, J.A. Williams, E.H. Manning, J.T. Roland, L.A. Lapierre, and J.R. Goldenring. 2016. Loss of MYO5B in mice recapitulates Microvillus Inclusion Disease and reveals an apical trafficking pathway distinct to neonatal duodenum. *Cell Mol Gastroenterol Hepatol*. 2:131–157.

Well, D., S. Blanchard, J. Kaplan, P. Guilford, F. Gibson, J. Walsh, P. Mburu, A. Varela, J. Levilliers, M.D. Weston, P.M. Kelley, W.J. Kimberling, M. Wagenaar, F. Levi-Acobas, D. Larget-Piet, A. Munnich, K.P. Steel, S.D.M. Brown, and C. Petit. 1995. Defective myosin VIIA gene responsible for Usher syndrome type IB. *Nature*. 374:60–61.

Wells, A.L., A.W. Lin, L.Q. Chen, D. Safer, S.M. Cain, T. Hasson, B.O. Carragher, R.A. Milligan, and H.L. Sweeney. 1999. Myosin VI is an actin-based motor that moves backwards. *Nature*. 401:505–508.

Yang, Y., T.G. Baboolal, V. Siththanandan, M. Chen, M.L. Walker, P.J. Knight, M. Peckham, and J.R. Sellers. 2009. A FERM domain autoregulates Drosophila myosin 7a activity. *Proc. Natl. Acad. Sci. U. S. A.* 106:4189–4194.

Yan, J., L. Pan, X. Chen, L. Wu, and M. Zhang. 2010. The structure of the harmonin/sans complex reveals an unexpected interaction mode of the two Usher syndrome proteins. *Proc. Natl. Acad. Sci. U. S. A.* 107:4040–4045.

Yao, L.-L., Q.-J. Cao, H.-M. Zhang, J. Zhang, Y. Cao, and X.-D. Li. 2015. Melanophilin Stimulates Myosin-5a Motor Function by Allosterically Inhibiting the Interaction between the Head and

Tail of Myosin-5a. *Sci. Rep.* 5:10874.

Zadro, C., M.S. Alemanno, E. Bellacchio, R. Ficarella, F. Donaudy, S. Melchionda, L. Zelante, R. Rabionet, N. Hilgert, X. Estivill, G. Van Camp, P. Gasparini, and M. Carella. 2009. Are MYO1C and MYO1F associated with hearing loss? *Biochim. Biophys. Acta*. 1792:27–32.

Zattelman, L., R. Regev, M. Ušaj, P.Y.A. Reinke, S. Giese, A.O. Samson, M.H. Taft, D.J. Manstein, and A. Henn. 2017. N-terminal splicing extensions of the human MYO1C gene fine-tune the kinetics of the three full-length myosin IC isoforms. *J. Biol. Chem.* 292:17804–17818.

Zheng, L., G. Sekerková, K. Vranich, L.G. Tilney, E. Mugnaini, and J.R. Bartles. 2000. The deaf jerker mouse has a mutation in the gene encoding the espin actin-bundling proteins of hair cell stereocilia and lacks espins. *Cell*. 102:377–385.

Zihni, C., E. Vlassaks, S. Terry, J. Carlton, T.K.C. Leung, M. Olson, F. Pichaud, M.S. Balda, and K. Matter. 2017. An apical MRCK-driven morphogenetic pathway controls epithelial polarity. *Nat. Cell Biol.* 19:1049–1060.

Chapter 2

Cortical contraction drives the 3D patterning of epithelial cell surfaces

Authors

Aaron P. van Loon[1,*], Ivan S. Erofeev[2,*], Ivan V. Maryshev[2], Andrew B. Goryachev[2,†], and Alvaro Sagasti[1,†]

* Authors contributed equally

Affiliations

1. Department of Molecular, Cell and Developmental Biology and Molecular Biology Interdepartmental Program, University of California, Los Angeles

2. Centre for Synthetic and Systems Biology, School of Biological Sciences, University of Edinburgh

Reprinted with permission from: van Loon AP, Erofeev IS, Maryshev IV, Goryachev AB, Sagasti A. 2020. Cortical contraction drives the 3D patterning of epithelial cell surfaces. J Cell Biol 219. doi:10.1083/jcb.201904144. Copyright 2020 van Loon et al.

Abstract

Cellular protrusions create complex cell surface topographies, but biomechanical mechanisms regulating their formation and arrangement are largely unknown. To study how protrusions form, we focused on the morphogenesis of microridges, elongated actin-based structures that are arranged in maze-like patterns on the apical surfaces of zebrafish skin cells. Microridges form by accreting simple finger-like precursors. Live imaging demonstrated that microridge morphogenesis is linked to apical constriction. A non-muscle myosin II (NMII) reporter revealed pulsatile contractions of the actomyosin cortex, and inhibiting NMII blocked apical constriction and microridge formation. A biomechanical model suggested that contraction reduces surface tension to permit the fusion of precursors into microridges. Indeed, reducing surface tension with hyperosmolar media promoted microridge formation. In anisotropically stretched cells, microridges formed by precursor fusion along the stretch axis, which computational modeling explained as a consequence of stretch-induced cortical flow. Collectively, our results demonstrate how contraction within the 2D plane of the cortex can pattern 3D cell surfaces.

Introduction

Animal cells generate a broad repertoire of dynamic structures based on the highly versatile and plastic actin cytoskeleton (Pollard and Cooper, 2009; Blanchoin et al., 2014). Actin generates both the protrusive forces that shape the membrane and, in conjunction with myosin, contractile forces that can alter cell geometry. Rapid restructuring of the actin cytoskeleton is controlled by a core of conserved actin regulatory proteins, including nucleators, elongators,

bundlers, depolymerizers, and myosin motors (Pollard, 2016). Despite their universality, the divergent patterns of self-organization between these regulators generate a remarkable diversity of actin-based structures, including filopodia, lamellipodia, microvilli, dorsal ruffles, and podosomes (Blanchoin et al., 2014; Buccione et al., 2004). While actin regulatory proteins have been extensively studied, neither molecular mechanisms, nor biophysical principles that generate and switch between specific actin structures are well understood. The coexistence and competition of distinct actin-based structures within the same cell makes these problems even more complex (Rotty and Bear, 2014; Lomakin et al., 2015).

Microridges are membrane protrusions extended in one spatial dimension and arranged in remarkable, fingerprint-like patterns on the apical surface of mucosal epithelial cells (**Fig. 1A**) (Straus, 1963; Olson and Fromm, 1973). Microridges are found in a wide array of species on a variety of tissues, including the cornea, oral mucosa, and esophagus (Depasquale, 2018), and are thought to aid in mucus retention (Sperry and Wassersug, 1976; Pinto et al., 2019). Microridges are filled with actin filaments and associate with several actin-binding proteins (Depasquale, 2018; Pinto et al., 2019). Interestingly, microridges do not emerge as fully spatially-extended structures like dorsal ruffles. Instead, they assemble from short vertically-projecting precursors (Raman et al., 2016; Lam et al., 2015; Uehara et al., 1988; Gorelik et al., 2003). Ultrastructural analyses have demonstrated that actin filaments in microridges have mostly branched actin networks (Bereiter-Hahn et al., 1979; Pinto et al., 2019) and, therefore, it is unclear if microridge precursors are more similar in their actin organization to podosomes or microvilli, to which they had been frequently compared. To emphasize this distinction, we have dubbed these precursors actin “pegs”. Inhibiting Arp2/3 prevents aggregation of actin pegs into microridges, suggesting that branched actin networks are also required for microridge assembly (Lam et al., 2015; Pinto et al., 2019). Factors regulating non-muscle myosin II (NMII) activity have been found

to promote microridge elongation (Raman et al., 2016), but reports differ about whether NMII plays a direct role in microridge morphogenesis (Lam et al., 2015).

Although microridges are less studied than other actin-based structures, they offer an excellent opportunity to probe systemic properties of cytoskeletal regulation. Microridge patterns possess several characteristic parameters, including their spatial orientation, length distribution, and periodicity, which can be readily quantified from live images. These parameters reflect biochemical and biomechanical processes that regulate the morphogenesis of actin structures and are sensitive to experimental intervention. Multiple genetic and pharmacological perturbations can thus be applied to dissect principles of patterning and test theoretical hypotheses.

By imaging microridge development on the skin of larval zebrafish, we found that cortical contraction couples apical constriction to microridge morphogenesis. In vivo experiments and modeling suggest that contraction of the apical actomyosin cortex relieves surface tension to facilitate the coalescence of pegs to form, elongate, and orient microridges. Thus, cortical contraction not only determines the size and shape of the apical surface, but also concomitantly sculpts its 3D surface.

Results

The apical surfaces of periderm cells shrink as microridges form

We first asked if we could identify overarching organizational principles in the emergence of microridges from pegs. To characterize the process of microridge development in live animals, we imaged transgenic zebrafish expressing the F-actin reporter Lifeact-GFP specifically in periderm cells during development (Rasmussen et al., 2015; Helker et al., 2013). We developed

an automated image analysis protocol to segment microridges from these images and quantify microridge length in an unbiased manner (**Fig. S1**). As previously reported (Lam et al., 2015; Raman et al., 2016; Pinto et al., 2019), early in development (16 hours post-fertilization, hpf), periderm cells projected actin pegs that superficially resemble short microvilli (**Fig. 1A-B**). By 24 hpf, elongated microridges appeared near cell borders, whereas pegs still populated the center of the apical cell surface (**Fig. 1A-B**). By 32 hpf, microridges filled the apical surface, and continued to elongate through at least 48 hpf (**Fig. 1A-B**). This temporal progression of microridge growth was apparent from plotting the distribution of the pooled population of protrusions (**Fig. 1B, S2A**), or from measuring the average protrusion length per cell (**Fig. S2B**). To determine how cells transitioned from pegs to microridges, we imaged microridge growth in live animals at 15-30-second intervals. These videos revealed that pegs were dynamic, and coalesced to both form and elongate microridges (**Fig. S3, Video 1-1**). Time-lapse imaging also demonstrated that microridges form in a centripetal manner: assembly of microridges from pegs started in the cell periphery and progressed towards the cell center (**Fig. 1C, Video 1-1**). These observations confirmed previous studies suggesting that actin pegs are precursors to microridges that coalesce to form and elongate microridges (Lam et al., 2015; Pinto et al., 2019).

We next considered if microridge morphogenesis is associated with other changes in the morphology or biomechanical properties of the developing epithelium. Indeed, we noticed that during the period of transition from pegs to microridges (~16-32 hpf) the apical area of periderm cells decreased (44.7% on average), but stabilized between 32 hpf and 48 hpf (**Fig. 1D**). Moreover, average microridge length in individual cells inversely correlated with apical cell area: smaller cells had, on average, longer microridges (**Fig. S2C**), suggesting that apical area may influence microridge length. To determine whether cell areas shrunk predominantly by apical constriction or cell division, we imaged actin dynamics at 30-second intervals during an early stage of microridge elongation (18-19 hpf). These videos demonstrated that cells underwent

intermittent bouts of apical constriction and relaxation, but predominantly constricted, similar to the ratchet-like process that has been described in other instances of apical constriction (Martin et al., 2009; Solon et al., 2009; Blanchard et al., 2010). Microridge length closely tracked changes in apical cell area: microridges elongated, likely by peg accretion, as apical areas shrunk, and microridges shortened as apical areas increased (**Fig. 1E-F**). We conclude that pegs and microridges are in a dynamic equilibrium and that apical constriction promotes microridge formation.

A model for microridge formation reproduces experimental observations

Apical constriction significantly reduces the 2D-projected apical area of epithelial cells, as illustrated by our live-cell imaging (**Fig. 1E-F**). However, it was not clear how actin pegs and microridges, which determine the 3D topography of the membrane, affect the total surface area of the apical membrane. We therefore asked whether cells with pegs or cells with microridges have a larger 3D apical surface when their projected apical areas are identical. To answer this question, we assumed that actin pegs and microridges are of equal and uniform height and computationally evaluated the total 3D surface of apical regions with only microridges or only pegs. Surprisingly, after normalization by the 2D-projected area of the regions, we found that microridges induce larger membrane surfaces (**Fig. 1G**). Therefore, while apical constriction reduces the apical membrane surface, the associated transition from pegs to microridges increases it.

To gain quantitative insight into these observations, we developed a simple biophysical model of the cellular apical domain. We hypothesized that apical morphogenesis is generated by the dynamics of three closely interacting subsystems with distinct biomechanical properties: the membrane itself, the immediately underlying branched actin structure that fills pegs and microridges, and the deeper actomyosin cortex (**Fig. 2A**). Actin filaments within the branched

structure are largely disordered but project into the neighboring membrane (Uehara et al., 1991; Pinto et al., 2019), similar to the actin structures that power lamellipodia protrusion. We thus assumed that their polymerization stretches the membrane and expands the membrane surface. Conversely, filaments in the deeper actomyosin cortex are largely aligned parallel to the basal surface of cells (Pinto et al., 2019). Contraction of the cortex drives apical constriction (Martin and Goldstein, 2014) and reduces surface tension (**Fig. 2B**). Excess membrane is presumably removed by endocytosis (Sonal et al., 2014). We thus propose that the two actin subsystems have opposing effects on membrane area and tension; branched actin and the contractile actomyosin cortex increase and decrease surface tension, respectively. Pattern formation in our model is driven by the autocatalytic branched polymerization of actin at the membrane-cytoskeleton interface. To ensure formation of both pegs and microridges, we resorted to a prototypical activator-inhibitor model of Gierer and Meinhardt (Gierer and Meinhardt, 1972), in which the role of the inhibitor is played by the height h of the actin structure. This heuristic assumption mimics the opposition that surface tension produces to actin polymerization (Gov, 2006; Gov and Gopinathan, 2006; Atilgan et al., 2006; Mogilner and Rubinstein, 2005). Conversely, surface tension is relaxed by myosin motor-driven contraction of the actomyosin cortex, whose dynamics are described by the well-established active gel model (Prost et al., 2015). A detailed description of the model equations and parameters are provided in the Methods.

In our model, spatially uniform isotropic contraction of the apical actomyosin cortex produced a transition from pegs to microridges, which occurred uniformly on the apical surface (**Video 1-2**, right). We noticed that even with parameters corresponding to the initially relaxed cortex, when the interior of the apical domain is populated only by pegs, a single closed microridge had formed immediately proximal to the cell boundary (**Fig. 2C**). Interestingly, such microridges, positioned next to the tight junctions between cells, have been routinely observed in experiments by us and others (Depasquale, 2018). Remarkably, as in the model, they typically form prior to

the formation of microridges in the interior of the apical domain. In live-cell images, they emerged first as discontinuous, paired structures positioned on each side of, and strictly parallel to, the tight junctions (**Fig. 2C, inset**). As microridges developed within the apical interior, these junction-associated structures matured into proper microridges and continuously surrounded the entire apical domains of cells (**Fig. 1A**). In the model, formation of this outer microridge is determined by the boundary condition that fixes vertical membrane deflection on the boundary to $h = 0$. Thus, our model predicts that formation of these circumferential microridges is determined by the singularity in the surface tension imposed by unyielding tight junctions.

Model simulations showed that uniform contraction of the apical actomyosin cortex cannot explain centripetal emergence of microridges from the cell boundaries. We thus surmised that the apical actomyosin cortex could also undergo a process of maturation. Possibly, its contractility increases first at the tight junctions, where Rho GTPase activity that drives actin polymerization and myosin contraction is typically enriched (Zihni and Terry, 2015; Ratheesh et al., 2012), and then progresses inwards. Simulations of the model augmented with this additional hypothesis reproduced the experimental observations. Starting at the cell boundary, pegs coalesced into microridges, which eventually filled the entire apical domain (**Fig. 2D-E, Video 1-2, left**).

NMII is required for apical constriction and microridge formation

A previous study suggested that NMII is involved in lengthening microridges (Raman et al., 2016), but did not determine how it contributes to microridge formation, nor whether it is linked to apical constriction. We therefore sought direct evidence that NMII produces apical constriction and induces microridge morphogenesis from actin pegs. We first inhibited NMII contractility by treating zebrafish larvae with the specific small molecule inhibitor blebbistatin (Straight et al., 2003) for 24 hr spanning the period of microridge development (16-40 hpf). Blebbistatin reduced apical constriction in a concentration-dependent manner and inhibited the coalescence of pegs

into microridges (**Fig. 3A-C**). Since extended exposures to blebbistatin could affect microridges in a variety of direct or indirect ways, we examined the effects of shorter treatments; periderm cells expressing the actin reporter were imaged before and after 2 hr of blebbistatin exposure. During this short period of exposure, blebbistatin inhibited microridge elongation and reduced apical constriction, compared to controls (**Fig. 3E-F**). In control cells, microridge length and apical cell area were inversely correlated (R^2 = -.65), but this relationship was diminished by treatment with blebbistatin (R^2 = -.31) (**Fig. 3G**).

The branched actin nucleator Arp2/3 is required for microridge formation and maintenance (Lam et al., 2015). As expected, an inhibitor of Arp2/3, CK666 (Nolen et al., 2009), prevented coalescence of actin pegs into microridges (**Fig. S4A-B**), but did not prevent pegs from forming or reduce their dynamics (not shown). Interestingly, however, CK666 failed to reduce apical constriction and, in fact, appeared to promote it (**Fig. S4C**). This observation is consistent with our hypothesis that polymerization of the branched actin subsystem, for which Arp2/3 is required, induces membrane surface expansion and, thus, opposes apical constriction, which is driven by the underlying actomyosin layer.

To directly visualize the localization and activity of NMII in periderm cells during apical constriction and microridge development, we created a transgenic zebrafish line that expresses an NMII reporter (Maître et al., 2012) specifically in periderm cells. As expected, this reporter localized to cell-cell junctions and appeared to be distributed across the apical cortex. Time-lapse imaging revealed transient, local flashes of reporter fluorescence at the apical surface, which we interpreted as contractile pulses that concentrated NMII at their foci (**Fig. 4A, Video 1-3**). Indeed, one hour of exposure to blebbistatin was sufficient to significantly decrease these pulses (**Fig. 3D**), confirming that they reflect contractile activity of NMII. These apical NMII pulses temporally and spatially resembled pulsatile contractions that drive apical constriction in other systems (Fernández et al., 2007; Solon et al., 2009; Blanchard et al., 2010; David et al., 2010). Contractile

events concentrated towards the periphery of zebrafish periderm cells early in microridge development (16 hpf), progressed towards the center as development proceeded (24 hpf), and equalized across the apical surface after microridge formation (48 hpf) (**Fig. 4B**), supporting our hypothesis that apical constriction initiates at, and centripetally propagates from, junctions. This outside-in progression of cortical activity mirrors the spatial progression of microridge formation (**Fig. 1C**). Time-lapse imaging of periderm cells expressing both actin and NMII reporters demonstrated that contraction events pulled nearby actin pegs towards myosin foci (**Fig. 4C-D, Video 1-3**).

Contractile activity of NMII is activated via phosphorylation of the regulatory myosin light chain (MLC) by multiple kinases, such as Rho GTPase effector kinase (ROCK) and myosin light chain kinase (MLCK) (Matsumura, 2005). To determine if these kinases regulate microridge morphogenesis, we inhibited ROCK or MLCK with the small molecule inhibitors Rockout or ML-7, respectively, between 16-24 hpf. While ML-7 had no effect on microridge formation (data not shown), Rockout significantly decreased microridge length and increased apical cell area in a concentration-dependent manner (**Fig. 5A-C**). Additionally, one hour of Rockout treatment significantly reduced NMII pulses (**Fig. 5D**). Rockout did not dramatically affect peg dynamics, indicating that contraction specifically regulates peg coalescence, not peg formation (data not shown). This result indirectly supports the hypothesis that contraction of the actomyosin cortex is driven by activity of RhoA via its effector ROCK. We conclude that, regardless of its upstream regulation, NMII-driven contraction of the apical actomyosin cortex is required for both apical constriction and formation of microridges from actin peg precursors.

Surface tension directly controls microridge formation

Although the activity of NMII and its activation by ROCK are required for apical constriction and microridge formation, it is possible that myosin affects microridge formation by a means not

related to its biomechanical function; for example, by serving as a scaffold for signaling complexes. We therefore sought to directly test whether surface tension or an unrelated function of NMII controls microridge formation. To alter surface tension, we exposed zebrafish embryos to hyperosmolar media during early stages of microridge development. Placing animals in a hyperosmolar environment should draw water from periderm cells, causing them to "deflate", thus reducing surface tension independent of myosin contraction. Indeed, exposing zebrafish embryos to either high salt media or glycerol-supplemented media at a stage when cells are dominated by actin pegs, but before significant microridge formation typically occurs (16 hpf), caused cells to shrink rapidly (**Fig. 6**). Time-lapse imaging demonstrated that as cells shrank, actin pegs rapidly coalesced into microridges (**Fig. 6, Video 1-4**). Thus, reducing surface tension is sufficient to promote microridge formation, in agreement with our *in silico* model.

Anisotropy of microridge formation indicates that peg coalescence is an active process

To further our understanding of microridge formation, we sought to direct this process in a well-controlled experimental set-up. To achieve this goal, we leveraged the natural wound-healing behavior of epithelial sheets. In response to ablation of individual cells, neighboring cells generate a powerful biomechanical response to rapidly constrict the wound (Lam et al., 2015; Rosenblatt et al., 2001). If two cells are ablated simultaneously, intervening cells will sometimes undergo near perfect uniaxial stretching along the axis connecting the two wounds (**Fig. 7A-C**). For these experiments, we chose to ablate periderm cells at an early developmental stage with few microridges (16 hpf), using a laser on a 2-photon microscope (**Video 1-5**). Cells were selected for analysis if they exhibited robust uniaxial stretch. These analyses showed that stretch was accompanied by a small reduction of the apical surface, on average 10% of the projected area (**Fig. 7E**). Remarkably, as they stretched, all cells formed new microridges, which were predominantly aligned along the stretch axis (**Fig. 7B-D, F, Video 1-5**). The highest anisotropy of microridge orientation was coincident with the maximal distortion of stretched cells (~10 min after

ablation). This alignment slightly decreased as the epithelium relaxed into a new steady-state configuration.

Cell stretch produced by neighbor ablation temporarily induces flow of the viscoelastic actomyosin cortex, which is transmitted to the plasma membrane and the underlying branched F-actin cortex via multiple protein-protein links. The observed orientation of microridges along the stretch axis could be potentially explained by two distinct sources, both induced by flow. First, the torque generated by the actomyosin flow could re-orient preexisting microridges along the direction of stretch. However, quantification (**Fig. 7C,C'**) showed that, prior to cell stretch, microridges were essentially nonexistent and largely formed during the stretch itself. Thus, reorientation of preexisting microridges contributes little, if at all, to the aligned microridges seen in the experiment. Alternatively, microridges could form in an oriented manner if the fusion of pegs occurred preferentially along the direction of stretch. To test this second hypothesis, we quantified the angle at which actin peg fusion occurred after laser ablation. This analysis demonstrated that, in all analyzed cells, peg fusion was strongly anisotropic, on average three times more frequent along the stretch axis than perpendicular to it (**Fig. 7D**), confirming that microridges indeed form in an oriented manner.

The observation that pegs fuse along the stretch axis is surprising, as actin pegs sandwiched between the membrane and the actomyosin cortex are transported by the cortical flow and, thus, would be expected to collide preferentially along the direction orthogonal to the stretch axis (**Fig. 8A**). Theory predicts that peg fusion is energetically preferable (Gov, 2006; Derényi et al., 2002), as it reduces membrane bending energy. Hydrodynamic flow-induced collision of pegs should reduce the potential barrier to fusion and, therefore, promote peg fusion perpendicular to the direction of stretch. Indeed, in agreement with this theoretical argument, and contrary to experimental results, simulations of our model that emulated cell stretch produced preferential fusion of pegs perpendicular, rather than parallel, to the stretch axis (**Fig. 8C-D**). This

discrepancy suggested that our model failed to capture the full complexity of cortical biomechanics. Hydrodynamic flow could potentially order initially isotropic actin filaments along the stretch axis and, thus, induce orientation of force-generating NMII filaments (**Fig. 8B**). Counterintuitively, this passive re-orientation would increase the active stress generated by the actomyosin gel in the direction of stretch and reduce it in the opposite direction. Introduction of this hypothesis into our model produced simulation results in full agreement with the experiment (**Fig. 8C, E-F, Video 1-6**). Furthermore, the model revealed the existence of a minimal value of the flow-induced actomyosin anisotropy, below which peg fusion still occurs predominantly perpendicular to the stretch axis (**Fig. 8F**). Since our analysis of experimental data identified a significant (3:1) preference for pegs to fuse along the stretch axis, we conclude that stretch-induced cortical flow must induce substantial orientation of F-actin fibers and NMII motors.

Discussion

NMII-based contraction is well known to alter cell surfaces in two dimensions: for example, polarized contractions at junctions regulate polarized cell rearrangements (Bertet et al., 2004; Blankenship et al., 2006), and cortical contraction shrinks surfaces during apical constriction (Martin and Goldstein, 2014). Here we demonstrate that contraction in zebrafish periderm cells not only changes 2D cell surface geometry, but also simultaneously sculpts the 3D topography of cells: NMII-based cortical contractions couple apical constriction to the patterning of microridges, which protrude from the apical surface of zebrafish periderm cells, orthogonal to the cortex. Computational modeling and in vivo experiments together support a model in which cortical contractions lower surface tension to permit the coalescence of actin pegs into microridges, and cortical flow influences the organization of contractile machinery, which determines microridge orientation.

Microridges form by the accretion of precursor structures (pegs), a feature that distinguishes them from better-studied protrusions, such as lamellipodia and dorsal ruffles, which emerge and expand as a single unit. Inhibiting Arp2/3, NMII, or ROCK prevented peg coalescence into microridges, but did not appear to affect pegs themselves. Thus, peg formation and peg coalescence are two separate morphogenetic steps under distinct biomechanical and biochemical regulation. Understanding peg formation, actin dynamics in pegs, and the regulation of peg density will be critical to fully understanding microridge morphogenesis. For example, aggregation of similar peg-like precursors to form ridge-like structures in cultured kidney cells is influenced by actin dynamics (Gorelik et al., 2003). A critical local peg density may be required for microridge formation, but our observations suggest that it is not sufficient, since peg density remains relatively constant in the peripheral domain of cells for several hours before microridge formation begins (not shown). Upon integrating into microridges, pegs may, at least in part, retain their integrity as substructures since we, and others (Depasquale, 2018), have noted intensely labeled F-actin puncta within microridges. In fact, one ultrastructural study reported that periodic actin bundles could be discerned within microridges by electron microscopy (Bereiter-Hahn et al., 1979), though a more recent study using high resolution techniques did not identify these substructures (Pinto et al., 2019). Whether pegs contain bundled parallel actin filaments, like microvilli, or only branched filaments, like podosomes, is thus unclear. Identifying the bundling proteins, nucleators, and motors that localize to pegs may resolve whether they resemble microvilli or podosomes, or are unique structures with a distinct actin organization and protein composition.

The cortical contractions we observed in periderm cells resemble contractions driving well-characterized behaviors in other, better studied systems, like *C. elegans* and *Drosophila* gastrulation (Roh-Johnson et al., 2012; Martin et al., 2009). In those other systems, contraction is driven by Rho family GTPase signaling networks (Mason et al., 2013; Munjal et al., 2015;

Marston et al., 2016). It is thus likely that contraction of zebrafish periderm cells during microridge formation also depends on Rho family GTPases. Indeed, we found that the RhoA effector ROCK is required for apical contraction and microridge development in periderm cells, and previous work showed that RhoA inhibition can alter microridge patterning (Lam et al., 2015). Our observation that contractions initially predominate near cell borders may result from the association of RhoA regulators with cell-cell junctions (Ratheesh et al., 2012; Zihni and Terry, 2015), and could contribute to the centripetal progression of microridge formation. Defining the contribution of cell-cell junctions and Rho signaling networks could help explain how cortical contractions are tuned to create biomechanical conditions conducive to apical constriction and microridge morphogenesis.

Our theoretical model predicted that reducing surface tension is sufficient to promote peg coalescence into microridges. This prediction was supported by experiments showing that microridges rapidly formed as cells shrank in hyperosmolar media. Conversely, cell swelling would be predicted to prevent microridge formation or cause microridge disassembly. Unfortunately, fish larvae and periderm cells appeared to be unaffected by treatment with hypo-osmolar media (not shown), potentially due to homeostatic regulatory mechanisms. Nonetheless, a previous study showed that in zebrafish with Myosin Vb mutations, cells swell due to defects in vesicular trafficking and lose microridges (Sonal et al., 2014), consistent with the idea that increasing surface tension opposes microridge formation.

Contractile patterns are shaped by the flow of contractile machinery and NMII regulators within the plane of the cortex (Munjal et al., 2015; Rauzi et al., 2010; Bray and White, 1988). Our experiments and biomechanical modeling demonstrated that when cortical flow is anisotropically oriented by cell stretching, pegs coalesce into microridges in an oriented manner, aligning nascent microridges along the stretch axis. This phenomenon could explain microridge orientation during naturally anisotropic cell behaviors, like cytokinesis. Just before cytokinesis, cells expand and

microridges dissolve back into pegs; during cytokinesis, cells contract dramatically and microridges rapidly re-form (Lam et al., 2015). These new microridges are initially oriented predominantly perpendicular to the cytokinetic furrow, consistent with the observation that, during cytokinesis, ingression drives polarized cortical flow towards the furrow (Khaliullin et al., 2018; Cao and Wang, 1990; DeBiasio et al., 1996).

Microridges (and closely related structures called microplicae) are found on a variety of mucosal tissues in many vertebrate animals, suggesting that they play a common role in mucus retention (Depasquale, 2018). Nonetheless, their morphologies vary significantly in length, spacing, and branching, perhaps reflecting optimized morphologies for their function in different tissue contexts. Intriguingly, microridge morphology even varies in different parts of the zebrafish skin that are likely under distinct mechanical strains; for example, microridges are shorter and more branched in cells covering pectoral fins, and are reduced in periderm cells that stretch over bulges in the skin, such as those created by neuromast mechanosensory organs (not shown). This variation in microridge patterns provides an opportunity to further explore how actin regulators, contraction, and membrane biomechanics contribute to sculpting complex 3D membrane topographies.

Materials and Methods

Zebrafish

Zebrafish (Danio rerio) were raised at 28.5°C on a 14h/10h light/dark cycle. Embryos were raised at 28.5°C in embryo water composed of 0.3 g/L Instant Ocean Salt (Spectrum Brands, Inc.) and 0.1% methylene blue. Previously characterized zebrafish lines in this paper include AB wild-type fish (ZFIN: ZDB-GENO-960809-7), Tg(krt5:Gal4) (Rasmussen et al., 2015), Tg(UAS:Lifeact-GFP) (Helker et al., 2013). All experimental procedures were approved by the Chancellor's Animal Research Care Committee at UCLA.

Plasmids and Transgenes

Plasmids were constructed using the Gateway-based Tol2kit (Kwan et al., 2007). The following plasmids have been described previously: p5E-krt5 (Rasmussen et al., 2015), pME-myl12.1 (Maître et al., 2012), p3E-polyA, p3E-EGFPpA, and pDestTol2pA2 (Kwan et al., 2007).

To construct pME-lifeact-GFP, the following primers were used: (5'-GGGGACAAGTTTGTACAAAAAAGCAGGCTTAATGGGTGTCGCAGATTTG-3', 5'-GGGGACCACTTTGTACAAGAAAGCTGGGTATTACTTGTACAGCTCGTC-3'; actb1:lifeact-GFP; (Behrndt et al., 2012));

To construct pME-lifeact-Ruby, the following primers were used: (5'-GGGGACAAGTTTGTACAAAAAAGCAGGCTTAATGGGTGTCGCAGATTTG-3', 5'-GGGGACCACTTTGTACAAGAAAGCTGGGTATTAAGCGCCTGTGCTATG-3'; actb1:lifeact-RFP; (Behrndt et al., 2012)).

krt5:lifeact-GFP, krt5:lifeact-Ruby, and krt5:myl12.1-GFP plasmids were created by combining the appropriate Gateway entry vectors with the pDestTol2pA2 destination vector in an LR reaction. To generate zebrafish lines with each of these transgenes, wild type zebrafish embryos were injected at the one cell stage with the appropriate plasmid (50 pg/embryo) and Tol2 mRNA (50 pg/embryo).

Live imaging of zebrafish embryos

Live zebrafish embryos were anaesthetized with 0.2mg/mL MS-222 (Western Chemical) in system water prior to mounting. Embryos were embedded in 1.2% agarose on a cover slip and sealed within a microscope chamber, as previously described (O'Brien et al., 2009). For convenient mounting, images were taken on the top of the head through 32 hpf and images taken

after 32 hpf were captured on the side of the trunk, avoiding the yolk extension. Chambers were filled with 0.2mg/mL MS-222 solution and sealed with vacuum grease.

Hyperosmolar Media Treatment

After mounting zebrafish embryos on coverslips in 1.2% agarose, slide chambers were filled with solutions of either 0.15 g/mL Instant Ocean salt mix in DI water, or 12.5% glycerol in Ringer's Solution, with 0.2 mg/mL MS-222. Time-lapse imaging was started immediately after filling the slide chamber with hyperosmolar media.

Drug Treatments

All drugs were dissolved in DMSO. Treatment solutions were created by adding the appropriate volume of Blebbistatin (Cayman Chemical), Rockout (Santa Cruz Biotechnology), ML-7 (Tocris Bioscience), or an equivalent volume of DMSO (≤1%) to Ringer's Solution with 0.2 mg/mL MS-222. Zebrafish larvae were immersed in treatment solutions for the specified periods of time, then mounted in agarose and imaged while bathed in the same solution. For treatment periods longer than two hours, larvae were initially exposed to treatment solutions prepared without MS-222, then transferred to a treatment solution containing MS-222 at least 30 minutes prior to mounting and imaging.

Microscopy

Live fluorescent images and videos of microridge development, drug experiments, and hyperosmolar media experiments were performed on a Zeiss LSM510 or LSM800 confocal microscope. Images were acquired with Zeiss Zen software using an EC Plan-Neofluar 40x/1.30 Oil DIC M27 objective with 2-3x digital zoom. During imaging, zebrafish slide chambers were mounted on a heated stage set to 28°C. The X-Y position and Z-stack were occasionally adjusted during time-lapse imaging to keep the cells of interest in frame.

To ablate cells, we adapted a previously described method (O'Brien et al., 2009). Videos of cell stretching by periderm cell ablation were acquired using Zeiss Zen Software on a Zeiss LSM 880 microscope equipped with an EC Plan-Neofluar 40x/1.30 Oil DIC M27 objective and a Coherent Chameleon Ultra II 2-photon laser set to 813nm. A 488 laser was used to find and focus on the cell surface at 250x digital zoom, and the cell was then exposed to 2-photon laser illumination for 3-4 seconds at 5-6% laser power using "Live" scanning.

Image Analysis and Statistics

Statistical analyses and data presentation were conducted in RStudio (RStudio, Inc.). All distributions were statistically tested for normality using Shapiro-Wilks test for normality, and visually tested for normality using Q-Q Plots. All statistical comparisons contained one or more non-normal distributions, so non-parametric tests were chosen to analyze all data. p values generated by Dunn's tests were adjusted using the Benjamini-Hochberg method.

Image analysis was performed with FIJI (Schindelin et al., 2012). For display purposes, confocal z-stack images were projected (maximum intensity projection) and brightness and contrast were enhanced.

To analyze microridge length and other cell parameters, we developed an ImageJ script to automatically process cells in each image (**Fig. S1**). Cell outlines were traced by hand with the polygon selection tool to measure apical cell area. Brightness and contrast were automatically enhanced and the area around the cell was cleared. Images were then blurred using the Smoothen function three times, and passed through a Laplacian morphological filter from the MorphoLibJ plugin (Legland et al., 2016), using the square element and a radius of 1. Filtered images were automatically thresholded using the Triangle method and skeletonized. The Analyze Skeleton (2D/3D) feature was then used to measure microridge length.

To calculate surface excess for pegs and microridges (**Fig. 1G**), we cropped 10×10 μm samples showing regions occupied by pegs or microridges in several cell images and estimated the surface area of those samples with the following algorithm. We assumed that the height of the surface is proportional to the signal, and that both pegs and microridges have the same maximal height of $h = 400$ nm. We normalized the samples, so that the 10th percentile became 0 and the 90th percentile 1, then used the following formula: $A_{surf} = \iint \sqrt{1 + h^2(\nabla I)^2 dA} = \sum s^2 \sqrt{1 + (h/s)^2\left(I_x^2 + I_y^2\right)}$ where ∇I is the gradient of the image, I_x and I_y are normalized Sobel filters along x and y directions), s is the absolute pixel size and summation is taken over all pixels of the image. Surface excess of each sample was calculated $\epsilon = A_{surf}/A_{proj} - 1$, where A_{proj} is the area of the projected surface (width × length of the image).

To quantify NMII contraction, time-lapse z-stack images were projected and smoothened. Cell outlines were traced by hand and cells were cropped from each time-lapse frame. Brightness and contrast of each time-lapse frame was automatically adjusted, then images were automatically thresholded using the Triangle method. Thresholded pulses were measured using the ImageJ Analyze Particles function, excluding particles with < 4 pixels.

To construct the optic flow diagram (**Fig. 4D'**), we used the FlowJ plugin in Fiji (Lucas & Kanade algorithm).

To study the angular distribution of surface structure coalescence (**Fig. 7D**), we analyzed videos from ablation experiments. We isolated distinct peg coalescence events and determined their direction (the line connecting pegs on a frame just before fusion).

To calculate the direction and amount of elongation (**Fig. 7F**) we calculated the moment matrices M of cell shapes approximated with polygons (shifted to the polygons' centroids). We

then calculated non-rotational affine transformations that better transform the moment matrix at frame n to the moment matrix at frame n+1. The median direction of these transformations was defined as the direction of elongation. A ratio of the axes was defined as the elongation factor.

To calculate angular histograms for peg coalescence in the model (**Fig. 8D,E**), we created an automated version of the algorithm, which was used in the preparation of Figure 7D. This algorithm was applied to multiple (n = 100) simulations with random initial conditions, and the results plotted in the averaged histograms in Figures 8D,E.

To study how the angular distribution of peg coalescence in the model changes with the anisotropy parameter ϵ (**Fig. 8F**), we decreased the number of bins in the previous analysis to 2. All peg coalescence events with angles from −45° to 45° were considered to be parallel to the axis of stretch, whereas those with angles from 45° to 135° were considered perpendicular to it. We then calculated the polarization parameter $p = \frac{n_{\parallel} - n_{\perp}}{n_{\parallel} + n_{\perp}}$, using the number of coalescence events in both bins. As defined, the value $p = -1$ corresponds to all pegs merging perpendicular to the stretch axis, whereas $p = 1$ corresponds to all coalescence events parallel to it.

Modeling

We built a model as a system of partial differential equations and solved it with a finite element method. Calculations were performed with COMSOL Multiphysics (COMSOL, Inc); postprocessing was done with custom Python code.

A two layer model

We subdivided the apical surface of the cell into two interacting subsystems. The first layer represents a composite of the lipid membrane and the branched actin cytoskeleton, which fills pegs and microridges. The second layer represents the actomyosin cortex. The vertical component of interaction between the two layers results from the actin polymerization force of the

top layer and is opposed by the oppositely directed force of the bottom layer (Gov, 2006). For simplicity, we assumed that the interface between the two layers is flat and neglected its deformation, following an estimate based on the characteristic values of cortical tension (Balaban et al., 2001; Bischofs et al., 2009; Fischer-Friedrich et al., 2014) and the protrusive force of polymerizing actin (Lan and Papoian, 2008; Mogilner and Oster, 2003). This assumption is also consistent with the published ultrastructural analyses of the cytoskeleton in fish epidermal cells (Bereiter-Hahn et al., 1979; Pinto et al., 2019; Uehara et al., 1991).

The two layers are mechanically coupled. Due to the presence of extensive cytoskeletal linkers connecting actomyosin to the transmembrane proteins embedded in the lipid bilayer, we introduced a no slip boundary condition. Thus, the two layers are coupled by the common strain field. This coupling has two important consequences. First, velocity fields in the actomyosin layer induced by the forces directly translate onto the top layer. Second, these velocity fields produce advection of the patterned structures positioned there, such as pegs or microridges.

The cortex layer

To describe the actomyosin layer we used the active gel approach (Marchetti et al., 2013; Prost et al., 2015). Since we are interested in the behavior on a very long timescale (minutes and hours), we neglected inertia and shear elasticity and reduced the mechanics of the layer to a 2-dimensional compressible isotropic fluid with high viscosity and active stress. Following the active gel model (Prost et al., 2015), we formulated a standard force balance equation: $\frac{\partial}{\partial x_\beta}\left(\sigma^{\mathrm{a}}_{\alpha\beta} + \sigma^{\mathrm{h}}_{\alpha\beta} + \Pi\delta_{\alpha\beta}\right) = 0.$

In the force balance equation, the indices α, β, and γ belonging to {1,2} refer to the spatial coordinates x,y (x_1,x_2) in the plane of the layer, $\sigma^{\mathrm{a}}_{\alpha\beta}$ is the active stress, $\sigma^{\mathrm{h}}_{\alpha\beta}$ is the hydrodynamic (viscous) stress, and, finally, Π is the pressure. In all formulae, repeating indices imply the Einstein

summation convention and αβ is the Kronecker delta. Hydrodynamic stress for a 2D fluid was defined as: $\sigma_{\alpha\beta}^{\mathrm{h}} = \mu_1 U_{\gamma\gamma}\frac{\delta_{\alpha\beta}}{2} + \mu_2\left(U_{\alpha\beta} - U_{\gamma\gamma}\frac{\delta_{\alpha\beta}}{2}\right)$, where $U_{\alpha\beta} = \frac{\partial u_\alpha}{\partial x_\beta} + \frac{\partial u_\beta}{\partial x_\alpha}$ is a symmetric strain rate tensor, u_α is the velocity of the layer, and u_1 and u_2 are the bulk and shear viscosities.

Although in vivo the actomyosin cortex is constantly assembled and disassembled (Clark et al., 2013), for the sake of simplicity, we assumed in our model that the total mass of actomyosin is constant. In line with this assumption, we adopted a logarithmic continuation of Hooke's law as the constitutive relation describing the mechanical properties of actomyosin: $\Pi = \Pi_0 \log\rho$.

Here we defined the dimensionless density $\rho = V_0/V_1$ where V_0 and V_1 are infinitesimal volumes within the layer before and after deformation, and Π_0 is the effective stiffness of actomyosin. As defined, ρ follows the conservation law: $\frac{\partial \rho}{\partial t} + \frac{\partial(\rho u_\alpha)}{\partial x_\alpha} = 0$.

The top composite layer

We described the state of the top composite layer with a heuristic activator-inhibitor model of the Gierer-Meinhardt type (Gierer and Meinhardt, 1972), consisting of two spatially distributed variables: the autocatalytic activator of actin polymerization $c(x,y)$, and the height of the membrane $h(x,y)$ measured relative to an initial plane. The latter variable plays the role of the inhibitor and is presented in the Monge parametrization that is commonly used to describe membrane geometry under the assumption $|\nabla h| \ll 1$ (Kabaso et al., 2011; Gov, 2006).

The dynamics of the activator c was represented by the following equation that directly follows the Gierer-Meinhardt form:

$$\underbrace{\frac{\partial c}{\partial t} + \frac{\partial(c u_\alpha)}{\partial x_\alpha}}_{\substack{\text{material}\\ \text{derivative}}} = \underbrace{D_c \nabla^2 c}_{\text{Diffusion}} + \underbrace{k_{\mathrm{on}}}_{\text{production}} \underbrace{-k_{\mathrm{off}} c}_{\text{degradation}} + \underbrace{k_h H(c) K(h)}_{\substack{\text{height inhibited}\\ \text{activation}}}$$

Parameters $D_c, k_{on}, k_{off}, k_h, c_0$ and h_0 are constants whose values are given in Table 1. The last term corresponds to the process of positive feedback with a rate that saturates as the concentration c increases, and diminishes when h increases: $H(c) = \frac{(c/c_0)^2}{1+(c/c_0)^2}; K(h) = \frac{1}{1+h/h_0}$. Following Gierer and Meinhardt (Gierer and Meinhardt, 1972), we chose the second power in the Hill-like term $H(c)$ as the smallest integer power allowing the system to be unstable and form spatial patterns.

We described mechanical properties of the layer with the Helfrich Hamiltonian (Helfrich, 1973): $E = \int\{\Omega h^2 + S[\nabla h]^2\}\, dxdy$, where S is the effective layer tension coefficient. We added a spring-like "cytoskeletal confinement" term Ωh^2 to prevent unlimited spatially-homogeneous autocatalytic actin polymerization (Gov et al., 2003; Ben Isaac et al., 2013; Daniels et al., 2006; Gov, 2006), and neglected the curvature-dependent energy terms. Minimizing energy E, we obtained:

$$\underbrace{\frac{\partial h}{\partial t} + u_\alpha \frac{\partial h}{\partial x_\alpha}}_{\substack{\text{material} \\ \text{derivative}}} = \underbrace{\frac{F_c}{\gamma}(c^2 - c_1^2)}_{\substack{\text{actin} \\ \text{polymerization}}} + \frac{1}{\gamma}\left(-\frac{\delta E}{\delta h}\right).$$

The actin polymerization force is postulated to depend quadratically on the concentration of activator c with the preferred concentration c_1 and γ is the local Oseen parameter. The functional derivative has the form:

$$\frac{\delta E}{\delta h} = \underbrace{\Omega h}_{\substack{\text{restoring} \\ \text{force}}} - \underbrace{S\frac{\partial^2 h}{\partial x_\alpha \partial x_\alpha}}_{\substack{\text{membrane} \\ \text{tension}}}$$

In the force equilibrium, the actin polymerization force is balanced by the restoring force and surface tension.

We posited that tension of the top composite layer depends on its bulk strain $S\left(\frac{V_1-V_0}{V_0}\right)$, where V_0 and V_1 are the infinitesimal volumes before and after deformation. This constitutive relation can be written as $S(\rho^t)$, where ρ^t is the non-dimensional density of the top layer defined as $\rho^t = V_0/V_1$. Thus, introduced non-dimensional ρ^t is a variable representing the bulk strain and does not describe molecules, such as myosin. Following from the earlier introduced tight mechanical coupling between the layers by strain, we conclude that $\rho^t = \rho$. In other words, when the actomyosin layer contracts, the produced negative strain reduces the tension of the top layer. Making the simplest possible assumption about the response of this composite layer to strain, we adopted a linear relation in the form: $S = S_0 - S_1(\rho - 1)$.

Apical constriction

To model pattern formation during apical surface constriction, we applied time and space dependent active stress to a hexagonal cell with the side length L. We generated the initial pattern by simulating the equations for the lipid membrane layer with a zero-velocity field and zero pressure in the cortex layer.

We first used a spatially uniform active stress function: $\sigma^a_{\alpha\beta}(t,x,y) = \delta_{\alpha\beta}\sigma^a_0 g(t)$ where σ^a_0 is the magnitude of active stress, and $g(t)$ is a function representing temporal evolution: $g(t) = \frac{1-exp(-t/t_{AS})}{1-exp(-t_1/t_{AS})}$, where t_{AS} is a parameter given in Table 1, t_1 is the total simulation time. To model the hypothesis that apical constriction initiates at the cell periphery, we introduced a radially symmetric wave-like active stress function in the form: $\sigma^a_{\alpha\beta}(t,x,y) = \delta_{\alpha\beta}\sigma^a_0 step\left\{\frac{\sqrt{x^2+y^2}-L/2}{l_1} + \frac{L}{v_1 t_1}\left[g(t)-\frac{1}{2}\right]\right\}$ where σ^a_0 is the magnitude of active stress, l_1 is the transition half-length, v_1 is a typical wave propagation speed and $step(z)$ is a continuous step function: $step(z) = \left(\frac{3}{16}z^5 - \frac{5}{8}z^3 + \frac{15}{16}z + \frac{1}{2}\right)\theta(1-z^2) + \theta(z-1)$, where $\theta(z)$ is the Heaviside step function.

Anisotropic elongation

We speculate that during rapid uniaxial stretch of the cell, actomyosin filaments reorient in the direction of elongation (**Fig. 8B**) and thus introduce tensile anisotropy that propagates to the top layer. The surface tension term becomes: $f^{aniso} = S\frac{\partial}{\partial x_\alpha}\left(A_{\alpha\beta}\frac{\partial h}{\partial x_\beta}\right)$, where $A_{\alpha\beta}$ represents tensile anisotropic tensor, which we chose as: $A_{\alpha\beta} = \delta_{\alpha\beta} - \varepsilon\left\{1 - exp\left[-\frac{\widehat{U}}{\widehat{U}_0}\right]\right\}\frac{U^*_{\alpha\beta}}{\widehat{U}_0}$. Here $U^*_{\alpha\beta} = U_{\alpha\beta} - \frac{\delta_{\alpha\beta}}{2}U_{\gamma\gamma}$ is the traceless component of the strain rate $U_{\alpha\beta}$, $\widehat{U} = \sqrt{\frac{1}{2}U_{\alpha\beta}U_{\alpha\beta}}$ is the positive eigenvalue of traceless matrix $U_{\alpha\beta}$, ε is the maximal relative increment and $\widehat{U}_0$ is a typical strain-rate stress at which actomyosin filaments become partially ordered and surface tension becomes sensitive to anisotropic flow. The idea behind this dependency is as follows: without shear flow $\left(\widehat{U}_0 = 0\right)$, the tension tensor is isotropic. With very large shear flow $\left(\widehat{U}_0 \to \infty\right)$, tension in the direction of elongation becomes smaller by factor $1 - \varepsilon$ and tension in the orthogonal direction becomes greater by factor $1 + \varepsilon$. The transition occurs at a typical strain rate of $\widehat{U}_0$.

To simulate the elongation itself, we used a time-dependent affine transformation applied to the square border of the cell to simulate the experimental data (**Fig. 7E,F**). The duration of simulation was $t_2 = 15$ min. We varied parameter ε from 0 (isotropic case, Video 1-6, left panel) to 0.4. An anisotropic case with $\varepsilon = 0.25$ is shown in Video 1-6 on the right.

Author Contributions

APvL, ISE, ABG, and AS conceived of and designed the study; APvL performed all zebrafish experiments; ISE, IVM, and ABG performed all theoretical experiments; APvL, ISE, ABG, and AS wrote the paper.

Acknowledgements

We thank members of the Sagasti lab and Margot Quinlan for comments on the work, and Son Giang for excellent fish care. We also appreciate image analysis advice from Dr. Roy Wollman and Dr. Alon Oyler-Yaniv. This work was funded by NIH grants R21EY024400 and R01GM122901 to AS and BBSRC grants BB/P01190X and BB/P006507 to ABG. APvL was supported by the Ruth L. Kirschstein National Research Service Award GM007185.

The authors declare no competing financial interests.

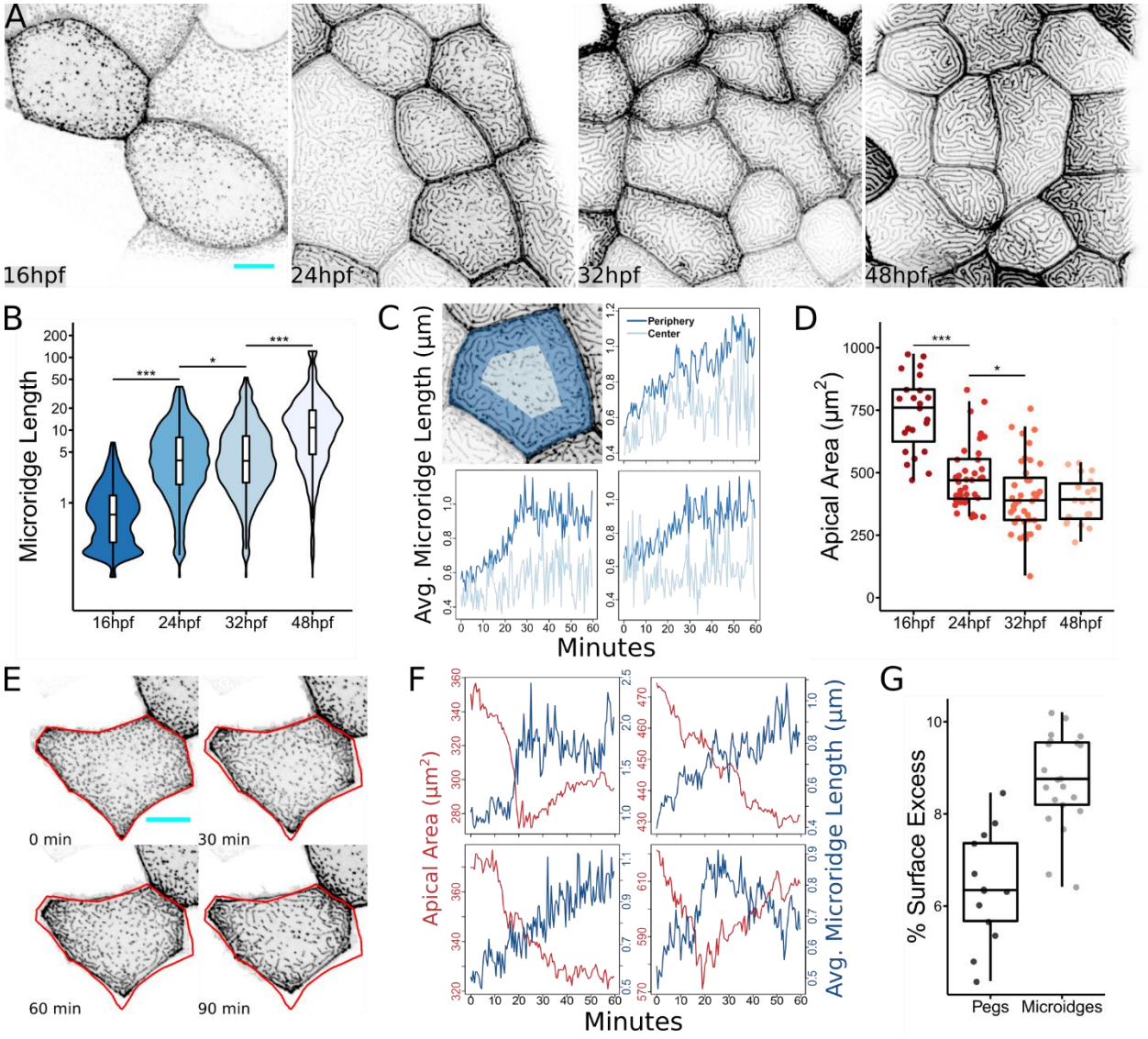

Figure 1. Microridge length changes in tandem with apical cell area. (A) Representative projections of Lifeact-GFP in periderm cells on zebrafish larvae at the indicated stages of zebrafish development. **(B)** Box and violin plot of microridge length at the indicated stages of zebrafish development. Data displayed are a weighted distribution of microridge length, in which frequency is proportional to microridge length, approximating occupied area. For a non-weighted presentation of the same data, see Fig. S1 K. *, P < 0.05; ***, P < 0.001; Kruskal–Wallis test followed by Dunn's test (*n* = 15,582 structures in 23 cells from 10 fish at 16 hpf; *n* = 5,096 structures in 40 cells from nine fish at 24 hpf; *n* = 4,572 structures in 40 cells from nine fish at 32

hpf; *n* = 1,309 structures in 19 cells from six fish at 48 hpf). **(C)** Top left: Representation of cell "periphery" (dark blue) and "center" (light blue) zones, representing 75% and 25% of apical cell area, respectively. Other panels: Line graphs comparing the average microridge length in the cell periphery versus the cell center over time. **(D)** Dot and box plot of periderm cell apical area at the indicated stages of zebrafish development. *, $P < 0.05$; ***, $P < 0.001$; Kruskal–Wallis test followed by Dunn's test (*n* = 23 cells from 10 fish at 16 hpf; *n* = 40 cells from nine fish at 24 hpf; *n* = 40 cells from nine fish at 32 hpf; *n* = 19 cells from six fish at 48 hpf). **(E)** Sequential projections from a time-lapse video of Lifeact-GFP in a single periderm cell during apical constriction. Red outline shows position of cell border at 0 min. **(F)** Line plots of apical area and average microridge length in single periderm cells over time. Top right panel corresponds to cell shown in E. **(G)** Dot and box plot of surface excess (relative difference between total surface area and projected surface area as seen in microscope) in regions of the apical cell membrane composed of only microridges or only pegs (*n* = 13 regions with pegs, *n* = 21 regions with microridges). Further details of this analysis are provided in Materials and methods. Scale bars, 10 µm (A and E). Avg., average. For box plots, middle box line is the median, and lower and upper ends of boxes are 25th and 75th percentiles, respectively.

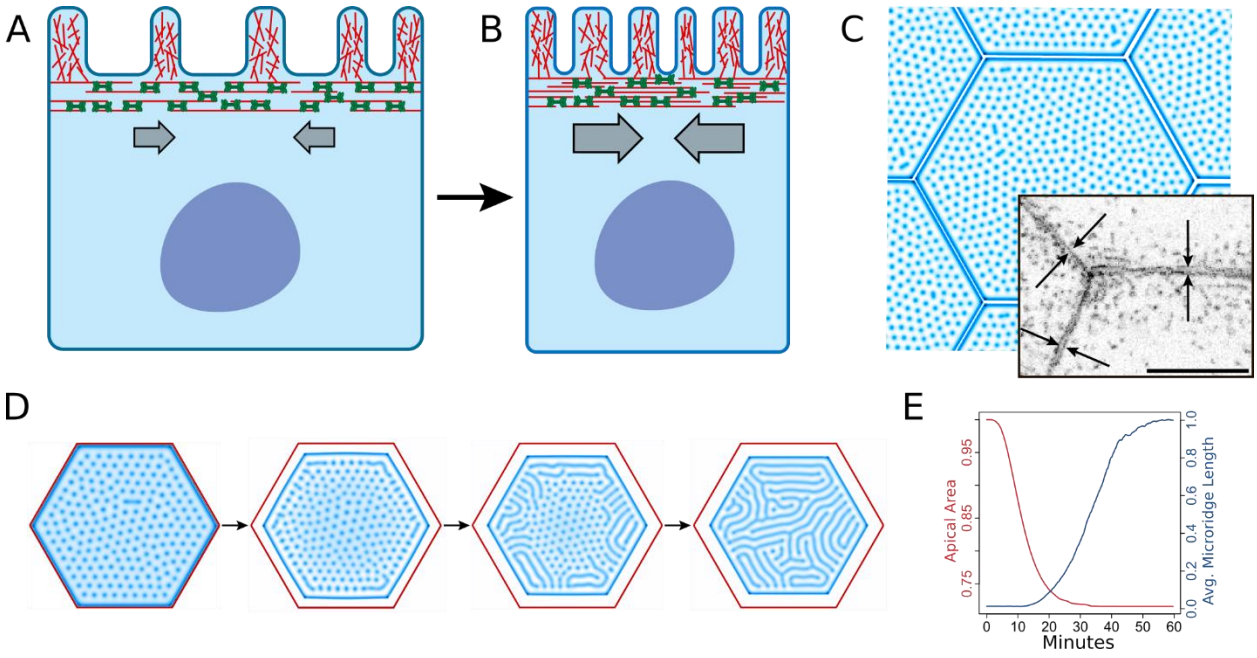

Figure 2. In silico simulation of apical constriction mimics microridge development in vivo. (A) Diagram of a periderm cell in homeostatic conditions with actin-filled microridges projecting from the apical surface. The underlying apical cortex is rich in actin (red filaments) and NMII (green bipolar mini-filaments) and attached to the cell membrane. **(B)** Diagram of a periderm cell undergoing apical constriction. NMII contraction in the apical cortex relieves tension in the attached cell membrane, allowing actin to protrude. **(C)** Cells from in silico simulations developed a long microridge at the cell border before microridge formation elsewhere on the apical membrane. Arrows in the inset image point to a similar structure in periderm cells expressing Lifeact-GFP before microridge development. **(D)** In silico simulation of apical constriction in our biomechanical model recapitulates the centripetal progression of microridge development observed in vivo. **(E)** Average change in apical area and average microridge length in 20 simulations. Scale bar, 10 µm (C).

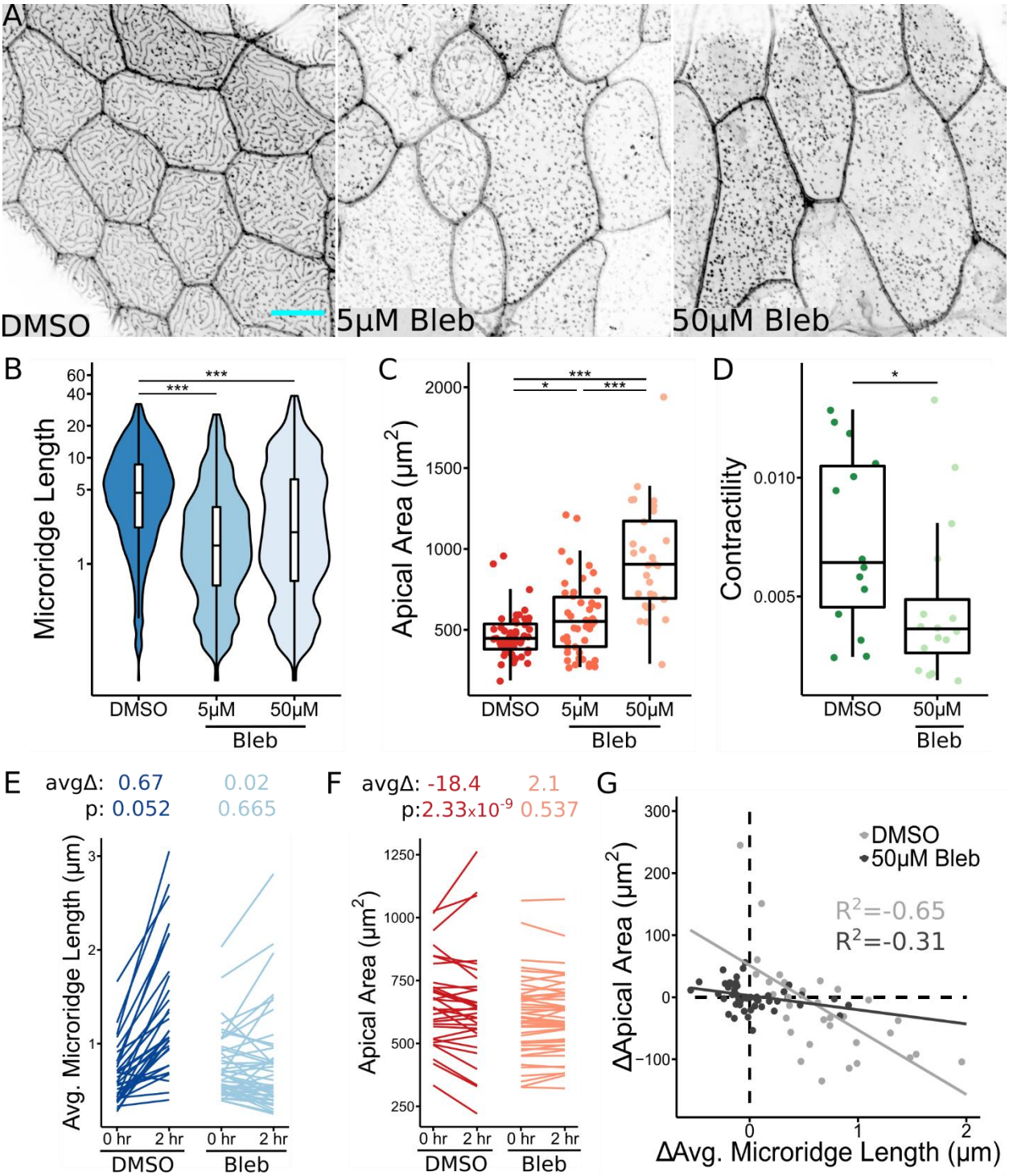

Figure 3. NMII contraction is required for apical constriction and microridge development. (A) Representative projections of Lifeact-GFP in periderm cells on 40 hpf zebrafish larvae after 24-h treatment with either 1% DMSO or indicated concentration of

blebbistatin (Bleb). **(B)** Box and violin plot of microridge length in 40 hpf zebrafish embryos after 24-h treatment with either 1% DMSO or indicated concentration of blebbistatin. Data are presented as a weighted distribution of microridge length, in which frequency is proportional to length, approximating occupied area. ***, P < 0.001; Kruskal–Wallis test followed by Dunn's test (*n* = 6,772 structures in 53 cells from 10 fish for 1% DMSO, *n* = 9,587 structures in 46 cells from 11 fish for 5 µM blebbistatin; *n* = 8,623 structures in 29 cells from 13 fish for 50 µM blebbistatin). **(C)** Dot and box plot of periderm cell apical area in 40 hpf zebrafish embryos after 24-h treatment with either 1% DMSO or indicated concentration of blebbistatin. *, P < 0.05; ***, P < 0.001; Kruskal–Wallis test followed by Dunn's test (*n* = 53 cells from 10 fish for 1% DMSO, *n* = 46 cells from 11 fish for 5 µM blebbistatin, *n* = 29 cells from 13 fish for 50 µM blebbistatin). **(D)** Dot and box plot of frame average NMII reporter contraction area summed over a 10-min period (30-s intervals), after 1-h treatment with either 1% DMSO or 50 µM blebbistatin. *, P < 0.05; Wilcoxon rank-sum test (*n* = 10,416 contractions in 29 cells from 18 fish for 1% DMSO, *n* = 2,259 contractions in 16 cells from nine fish for 50 µM blebbistatin). **(E)** Line plots of average microridge length in individual periderm cells before (18 hpf) and after (20 hpf) 2-h treatment with either 1% DMSO or 50 µM blebbistatin. Above, average change in average microridge length and P values (Wilcoxon signed-rank test; *n* = 17,039 structures in 64 cells from 10 fish for 1% DMSO, *n* = 20,873 structures in 92 cells from 11 fish for 50 µM blebbistatin). **(F)** Line plots of periderm cell apical area in individual cells before (18 hpf) and after (20 hpf) 2-h treatment with either 1% DMSO or 50 µM blebbistatin. Above, average change in periderm cell apical area and P values (Wilcoxon signed-rank test; *n* = 64 cells from 10 fish for 1% DMSO, *n* = 92 cells from 11 fish for 50 µM blebbistatin). **(G)** Scatter plot of change in average microridge length versus change in periderm cell apical area after 2-h treatment with 1% DMSO or 50 µM blebbistatin. R^2 determined using Pearson's correlation coefficient (*n* = 17,039 structures in 64 cells from 10 fish for 1% DMSO, *n* = 20,873 structures in 92 cells from 11 fish for 50 µM blebbistatin). Scale bar, 10 µm (A). For box

plots, middle box line is the median, and lower and upper ends of boxes are 25th and 75th percentiles, respectively.

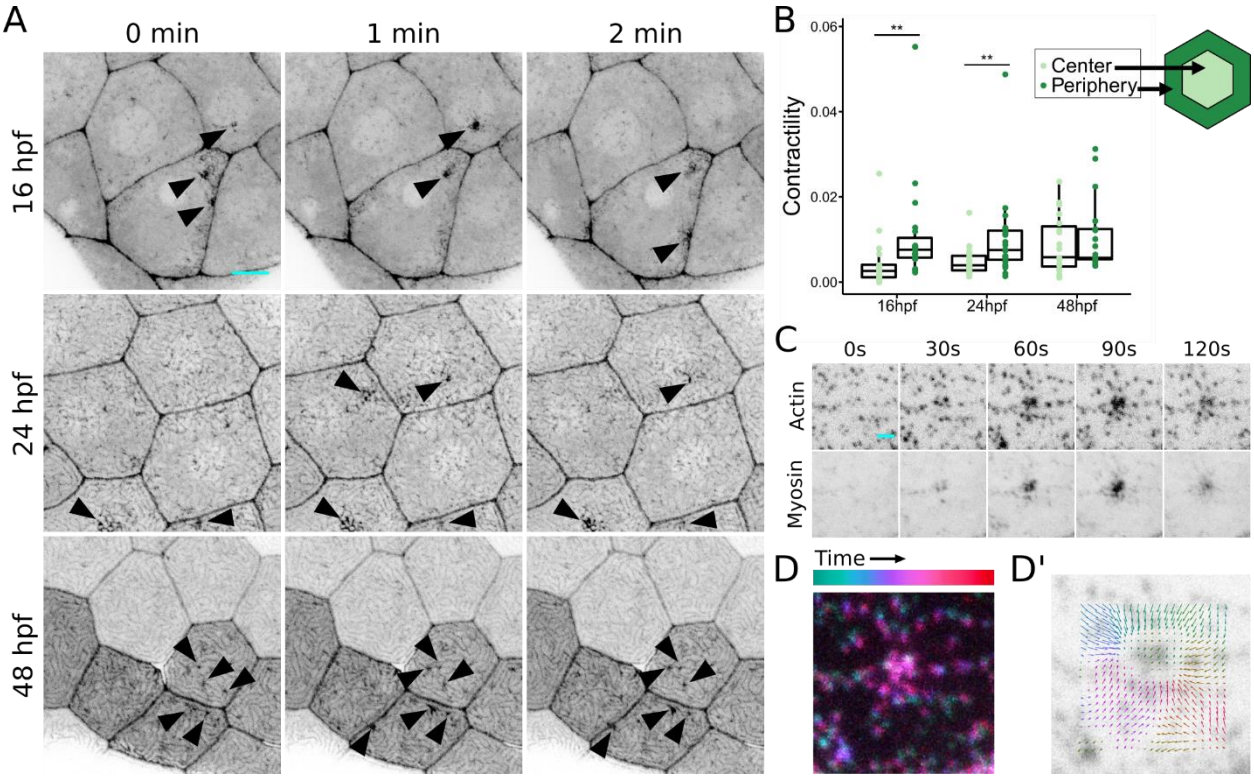

Figure 4. Apical NMII contractions pinch the cell membrane. (A) Sequential projections from time-lapse videos of Myl12.1-EGFP in periderm cells at indicated stages of zebrafish development. Arrowheads: dynamic concentrations of NMII reporter fluorescence at the apical membrane. **(B)** Dot and box plot of frame average NMII reporter contraction area summed over a 10-min period (30-s intervals) at specified time points during zebrafish development. Contractions were categorized based on whether the majority of contraction area was within the inner 25% of the cell surface (Center) or in the remaining outer 75% (Periphery). **, $P < 0.01$; Wilcoxon signed-rank test (*n* = 11,794 contractions in 19 cells from 13 fish at 16 hpf; *n* = 18,776 contractions in 25 cells from 13 fish at 24 hpf; *n* = 6,303 contractions in 19 cells from seven fish at 48 hpf). **(C)** Sequential projections from a time-lapse video of Lifeact-Ruby and Myl12.1-EGFP during an apical NMII pulse in a 16 hpf periderm cell. **(D and D')** Superimposition of sequential frames from a time-lapse video (D) and particle image velocimetry (D') show the centripetal trajectory of actin structures toward the focus of contraction. Scale bars, 10 µm (A) and 2 µm (C).

For box plots, middle box line is the median, and lower and upper ends of boxes are 25th and 75th percentiles, respectively.

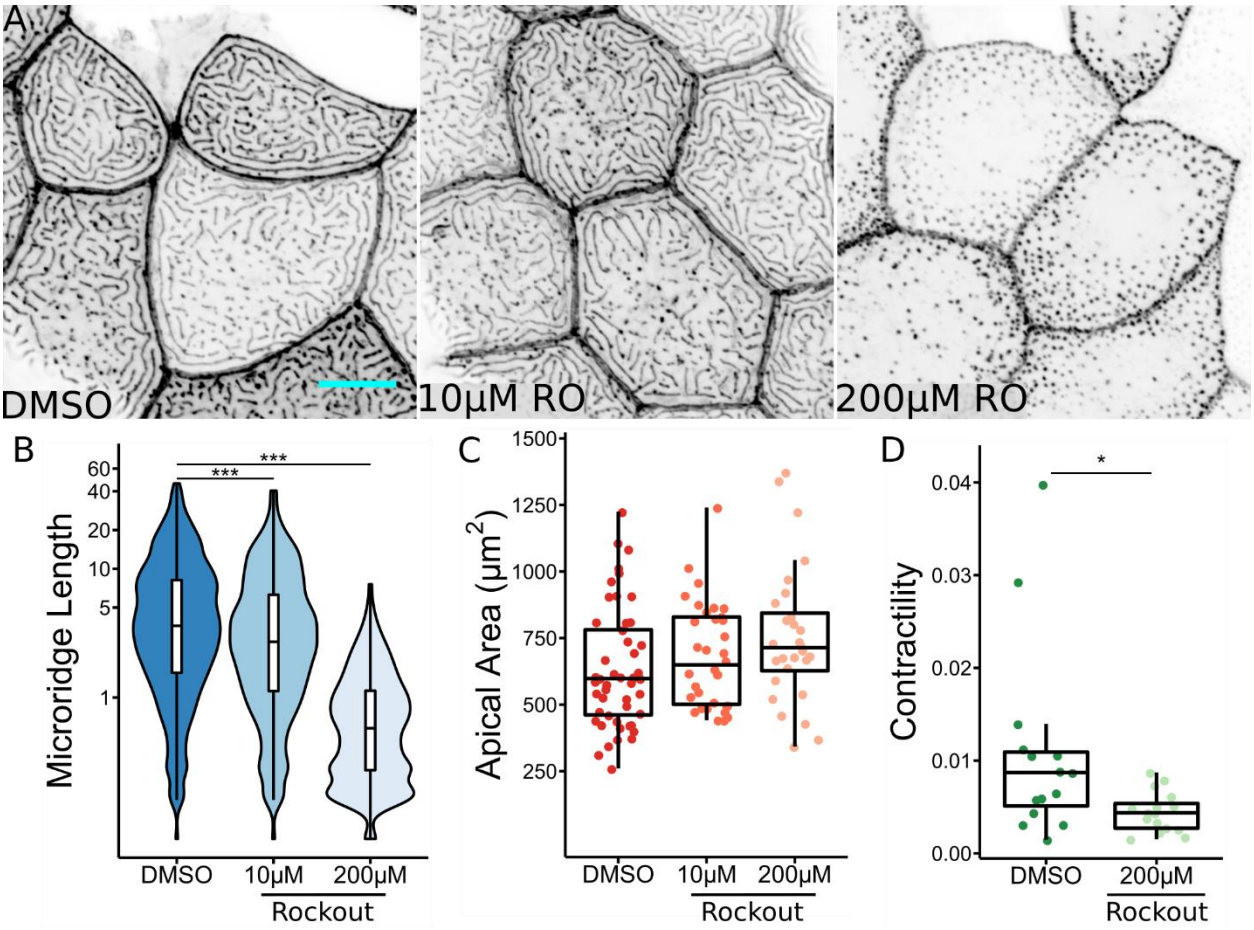

Figure 5. ROCK activity is required for microridge development. (A) Representative projections of Lifeact-GFP in periderm cells on 24 hpf zebrafish larvae after 8-h treatment with either 0.2% DMSO or indicated concentration of Rockout (RO). **(B)** Box and violin plot of microridge length in 24 hpf zebrafish embryos after 8-h treatment with either 0.2% DMSO or indicated concentration of Rockout. Data displayed are a weighted distribution of microridge length, where frequency is proportional to microridge length, approximating occupied area. ***, P < 0.001; Kruskal–Wallis test followed by Dunn's test (*n* = 10,385 structures in 49 cells from 15 fish for 0.2% DMSO, *n* = 8,353 structures in 34 cells from 11 fish for 10 µM Rockout, *n* = 7,501 structures in 28 cells from 10 fish for 200 µM Rockout). **(C)** Dot and box plot of periderm cell apical area in 24 hpf zebrafish embryos after 8-h treatment with either 0.2% DMSO or indicated concentration of Rockout. P = 0.063; Kruskal–Wallis test (*n* = 49 cells from 15 fish for 0.2%

DMSO, *n* = 34 cells from 11 fish for 10 µM Rockout, *n* = 28 cells from 10 fish for 200 µM Rockout). **(D)** Dot and box plot of frame average NMII reporter contraction area summed over a 10-min period (30-s intervals), after 1-h treatment with either 0.2% DMSO or 200 µM Rockout. *, $P < 0.05$; Wilcoxon rank-sum test (*n* = 9,048 contractions in 15 cells from 10 fish for 0.2% DMSO, *n* = 3,495 contractions in 16 cells from 10 fish for 200 µM Rockout). Scale bar, 10 µm (A). For box plots, middle box line is the median; lower and upper ends of boxes are 25th and 75th percentiles, respectively.

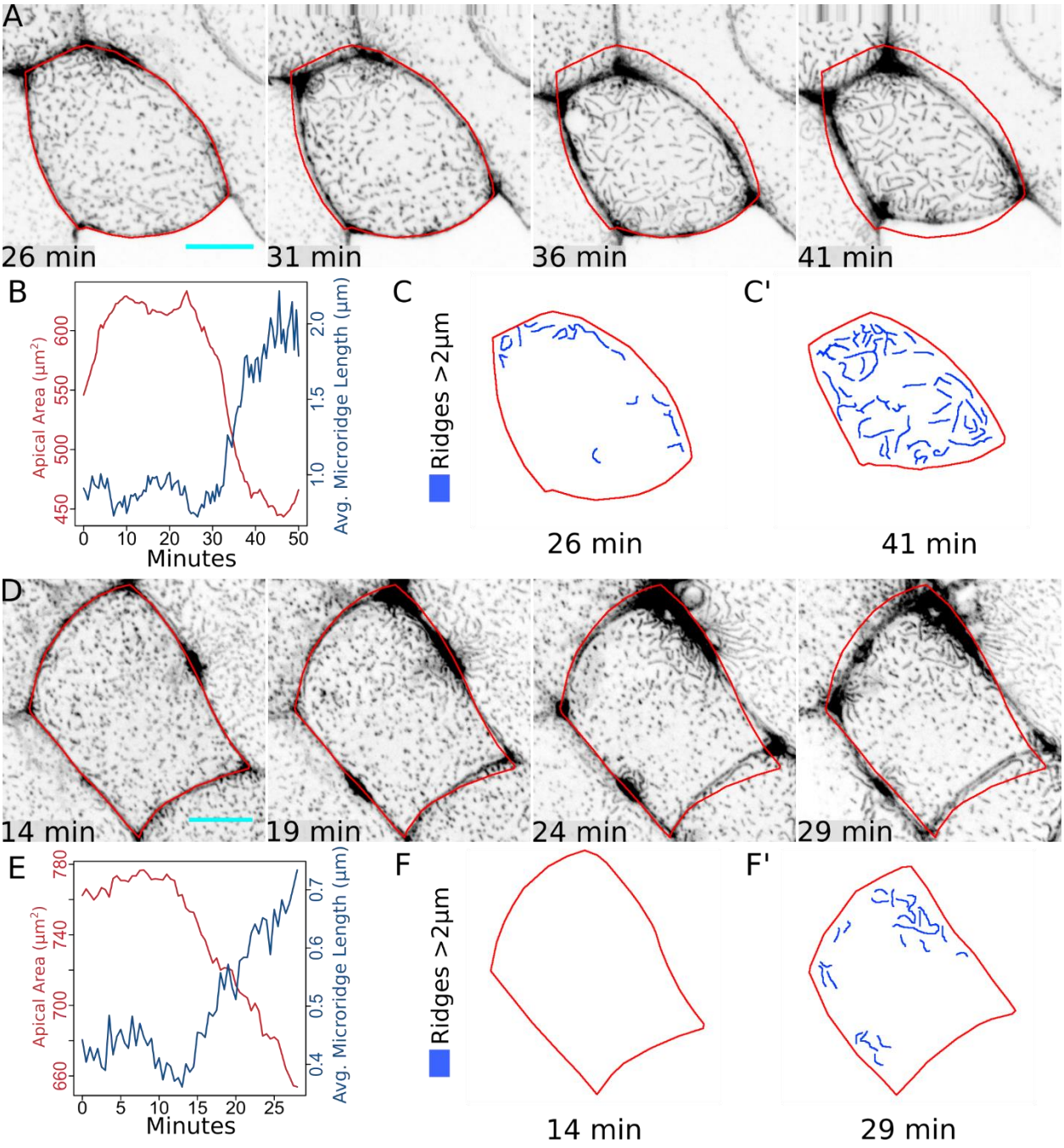

Figure 6. Membrane surface energy regulates microridge formation. (A) Sequential projections from a time-lapse video of Lifeact-GFP in periderm cells after exposure to water with 500× Instant Ocean salt. Red outline shows position of cell border at 26 min. **(B)** Line plot of apical area and average microridge length in the periderm cell shown in A after exposure to water with 500× Instant Ocean salt. **(C and C')** Diagram of cell in A at the indicated time points with

microridges longer than 2 μm traced in blue. **(D)** Sequential projections from a time-lapse video of Lifeact-GFP in periderm cells after exposure to 12.5% glycerol. Red outline shows position of cell border at 14 min. **(E)** Line plot of apical area and average microridge length in the cell shown in D after exposure to 12.5% glycerol. **(F and F')** Diagram of cell in E at the indicated time points with microridges longer than 2 μm traced in blue. Scale bars, 10 μm (A and D).

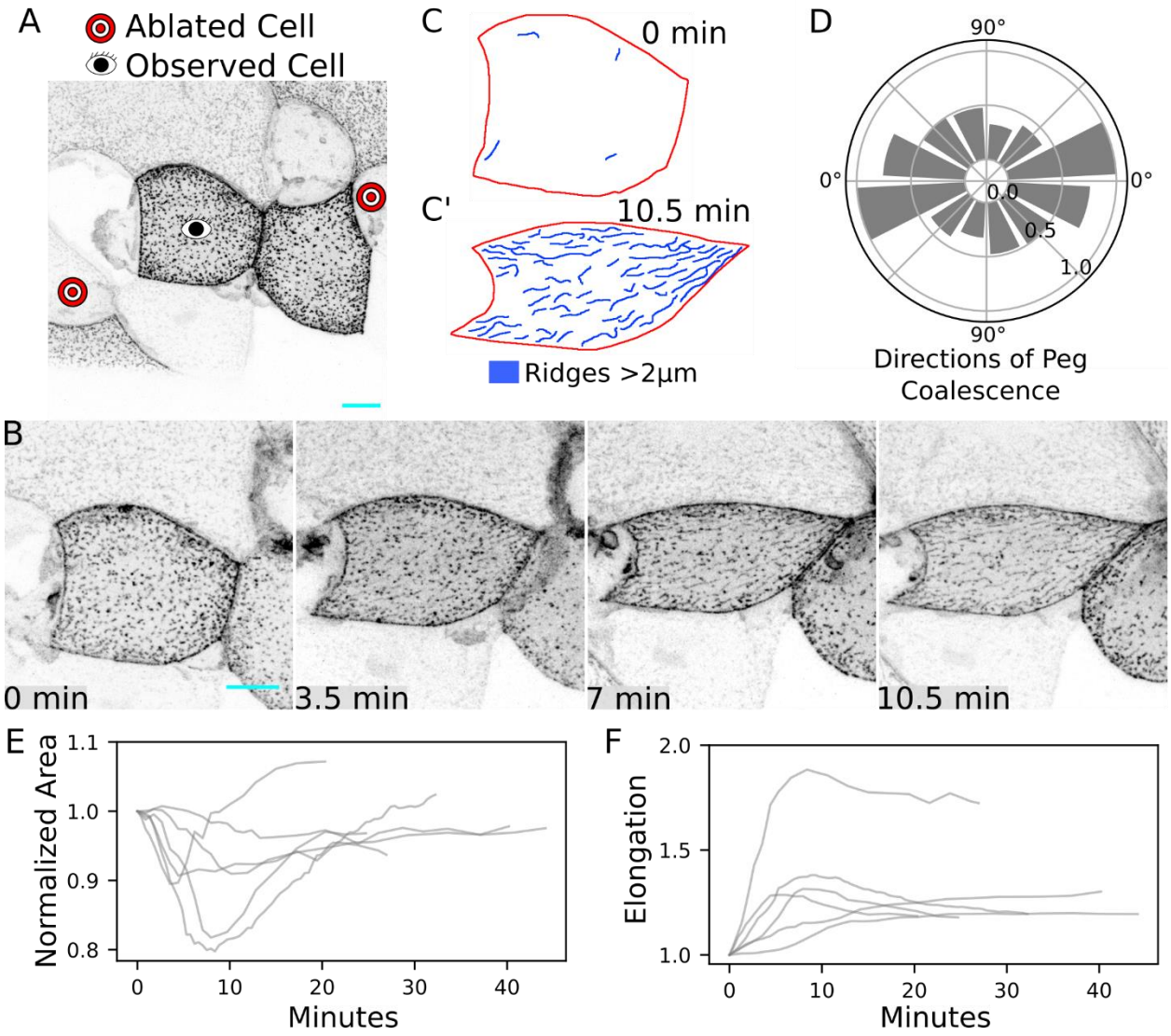

Figure 7. Cell stretching promotes formation of microridges along the elongation axis. (A) Projection of Lifeact-GFP in periderm cells on a 16 hpf zebrafish embryo before laser cell ablation. Eye: observed cell. Target: cell to be ablated. **(B)** Still images from a time-lapse sequence of the cell in A elongating over 10 min. **(C and C')** Outline of the elongating cell in B, shown at the initial time-point (C), and 10 min after ablation (C'). Microridges longer than 2 µm are highlighted in blue. **(D)** Averaged histogram of directions of peg coalescence events (normalized to maximal bin, direction of elongation at 0°). **(E)** Projected area for five cells used in this analysis. Areas were normalized to the initial value. **(F)** Elongation factor (ratio of longest axis

to shortest axis for the transformation of the cell) for five analyzed cells. Scale bars, 10 μm (A and B).

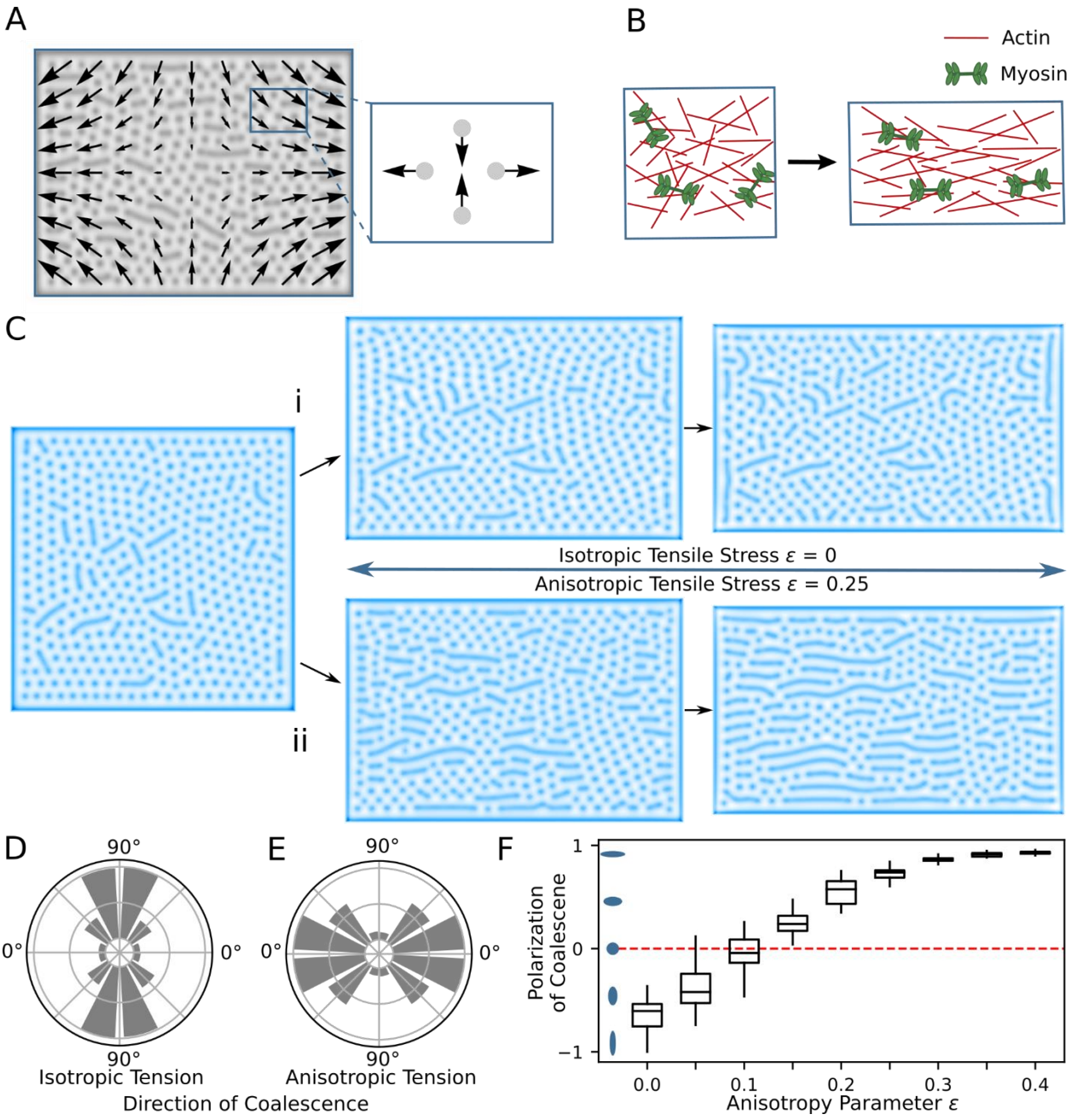

Figure 8. Flow-induced actomyosin anisotropy directs peg fusion along the cell stretch axis. (A) Approximated cortex flow during uniaxial stretch. Flow can be locally represented as elongation along one axis and compression along an orthogonal axis. **(B)** Scheme of rapid stretch that leads to partial alignment of actin and myosin filaments. **(C)** Modeling of cell stretching with isotropic (i) and anisotropic (ii) tensile stress. **(D and E)** Corresponding histograms of distributions

of structure fusions (averaged over 100 simulations with different initial conditions). If tension does not depend on the anisotropic flow, the fusions occur mostly in the direction perpendicular to the elongation (D). In the case of anisotropic tensile stress, the fusions occur in the direction of elongation (E). **(F)** Polarization of coalescence histogram for different values of the anisotropy parameter. Polarization value −1 corresponds to coalescence in the perpendicular direction and value 1 corresponds to coalescence in the direction parallel to elongation. For box plots, middle box line is the median, and lower and upper ends of boxes are 25th and 75th percentiles, respectively.

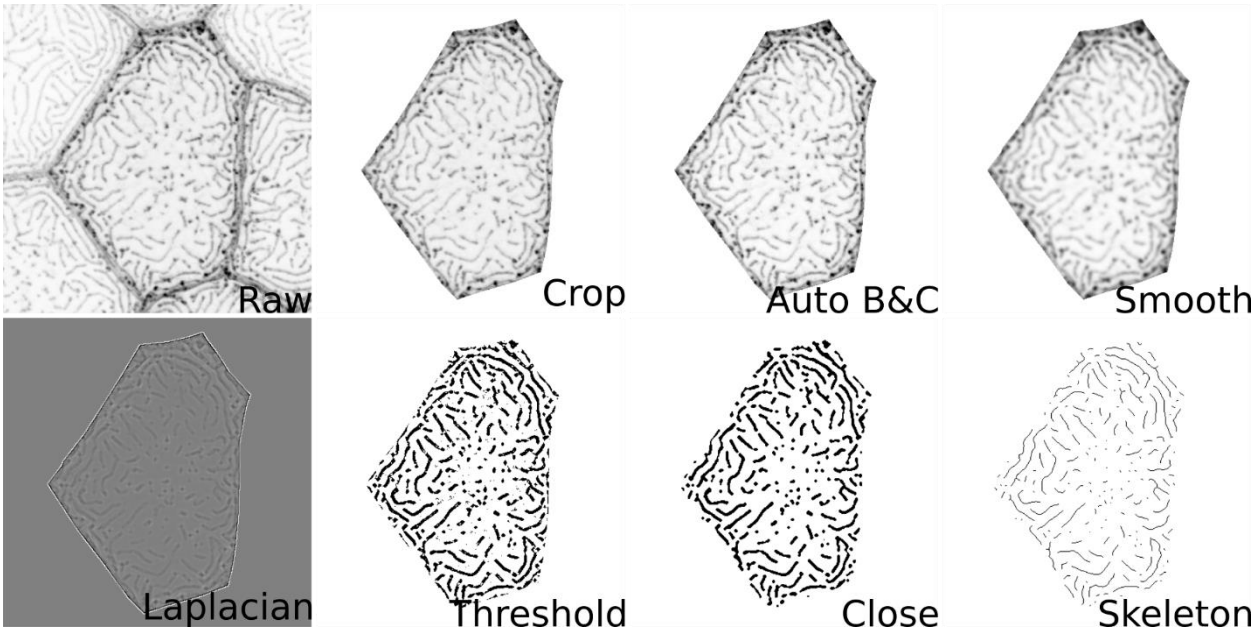

Figure S1. Image analysis method for microridge detection. Stepwise illustration of image analysis pipeline, as described in Materials and methods.

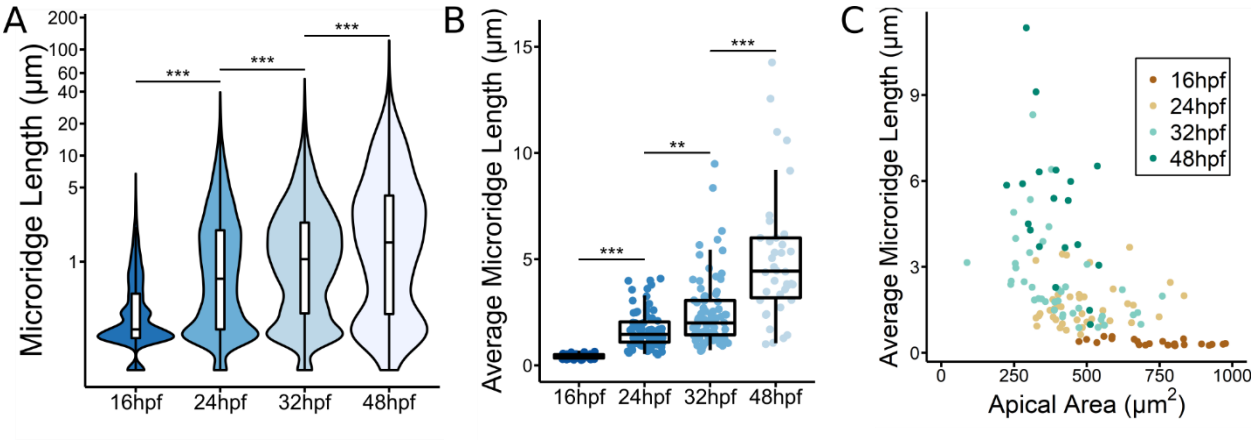

Figure S2. Additional analyses of microridge development. (A) Box and violin plot of microridge length in periderm cells at the indicated stages of zebrafish development. For a weighted presentation of this data, see Fig. 1 B. ***, P < 0.001; Kruskal–Wallis test followed by Dunn's test (*n* = 15,582 structures in 23 cells from 10 fish at 16 hpf; *n* = 5,096 structures in 40 cells from nine fish at 24 hpf; *n* = 4,572 structures in 40 cells from nine fish at 32 hpf; *n* = 1,309 structures in 19 cells from six fish at 48 hpf). **(B)** Dot and box plot of average microridge length per periderm cell at the indicated stages of zebrafish development. **, P < 0.01; ***, P < 0.001; Kruskal–Wallis test followed by Dunn's test (*n* = 15,582 structures in 23 cells from 10 fish at 16 hpf; *n* = 5,096 structures in 40 cells from nine fish at 24 hpf; *n* = 4,572 structures in 40 cells from nine fish at 32 hpf; *n* = 1,309 structures in 19 cells from six fish at 48 hpf). **(C)** Scatter plot of average microridge length per cell versus apical cell area at the indicated stages of zebrafish development (*n* = 15,582 structures in 23 cells from 10 fish at 16 hpf; *n* = 5,096 structures in 40 cells from nine fish at 24 hpf; *n* = 4,572 structures in 40 cells from nine fish at 32 hpf; *n* = 1,309 structures in 19 cells from six fish at 48 hpf). For box plots, middle box line is the median, and lower and upper ends of boxes are 25th and 75th percentiles, respectively.

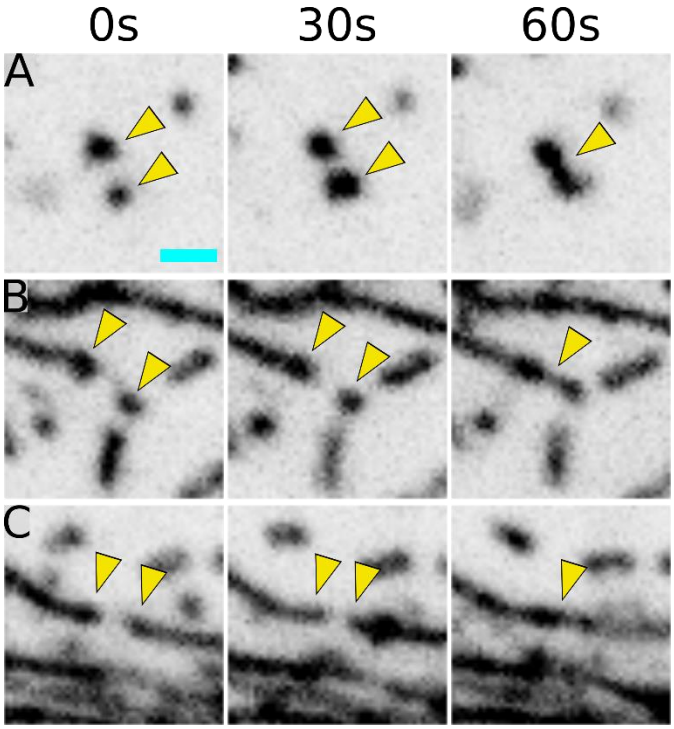

Figure S3. Three modes of microridge formation and growth. (A-C) Time-lapse sequences show examples of two pegs coalescing to form an incipient microridge (A), the addition of a peg to the end of a preexisting microridge (B), and the joining of two preexisting microridges (C). Scale bar, 1 μm (A).

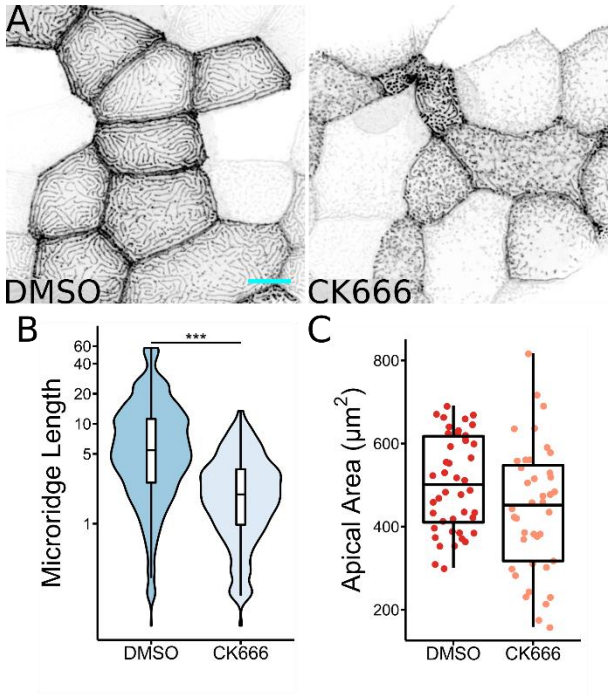

Figure S4. Arp2/3 activity is required for microridge development, but not apical constriction. (A) Representative projections of Lifeact-GFP in periderm cells on 24 hpf zebrafish larvae after 8-h treatment with either 1% DMSO or 100 µM CK666. **(B)** Box and violin plot of microridge length in 24 hpf zebrafish larvae after 8-h treatment with either 1% DMSO or 100 µM CK666. Data displayed are a weighted distribution of microridge length where frequency is proportional to microridge length, approximating occupied area. ***, P < 0.001; Wilcoxon rank-sum test (*n* = 5,283 structures in 44 cells from 11 fish for 1% DMSO, *n* = 6,130 structures in 40 cells from 12 fish for 100 µM CK666). **(C)** Dot and box plot of periderm cell apical area in 24 hpf zebrafish embryos after 8-h treatment with either 1% DMSO or 100 µM CK666. P = 0.052; Wilcoxon rank-sum test (*n* = 44 cells from 11 fish for 1% DMSO, *n* = 40 cells from 12 fish for 100 µM CK666). Scale bar, 10 µm (A). For box plots, middle box line is the median, and lower and upper ends of boxes are 25th and 75th percentiles, respectively.

Table 1. Parameters of the Model

Parameter	Value	Description
$\boldsymbol{\mu_1}$	$10^{-6}Pa \cdot s$	Bulk dynamic viscosity
$\boldsymbol{\mu}$	$10^{-5}Pa \cdot s$	Shear dynamic viscosity
$\boldsymbol{\Pi_0}$	$3 \cdot 10^{-8}\ N/m$	Effective stiffness of cortex layer
$\boldsymbol{D_c}$	$0.25\ \mu m^2$	Diffusion of activator
$\boldsymbol{k_{on}}$	0.054	Activator recruitment rate
$\boldsymbol{k_{off}}$	1.5	Activator turnover coefficient
$\boldsymbol{k_h}$	3.86	Coefficient of height mediated activation
$\boldsymbol{c_0}$	0.42	Activator coefficient
$\boldsymbol{h_0}$	0.39	Height coefficient
$\boldsymbol{\Omega/\gamma}$	1	Restoring force coefficient
$\boldsymbol{F_c/\gamma}$	5.76	Actin polymerization force coefficient
$\boldsymbol{c_1}$	0.42	Actin polymerization concentration offset
$\boldsymbol{S_0/\gamma}$	$15\ \mu m^2/s$	Initial surface tension
$\boldsymbol{S_1/\gamma}$	$25\ \mu m^2/s$	Surface tension density dependence coefficient
$\boldsymbol{\sigma_0^a}$	$10^{-8}\ N/m$	Active stress
$\boldsymbol{L}$	$100\ \mu m$	Size of the cell
$\boldsymbol{l_1}$	$\boldsymbol{50\ \mu m}$	Typical length of active stress transition
$\boldsymbol{t_1}$	$\boldsymbol{60\ min}$	Duration of apical constriction experiment
$\boldsymbol{t_{AS}}$	$\boldsymbol{20\ min}$	Time inhomogeneity coefficient
$\boldsymbol{v_1}$	$\boldsymbol{111\ \mu m/h}$	Speed of active stress transition
$\boldsymbol{\varepsilon}$	$0 - 0.4$	Maximal relative tension increment (anisotropy parameter)
$\boldsymbol{\widehat{U}_0}$	$10^{-4}s^{-1}$	Transition strain rate

Video Legends

Video 1-1. Live imaging of Lifeact-GFP in periderm cells during microridge development, beginning at 18 hpf. All images are maximum intensity projections; time stamp represents hours:minutes:seconds. Frame rate is 25 frames/s.

Video 1-2. Simulation of microridge formation. In silico simulation of apical constriction in our biomechanical model recapitulates the centripetal progression of microridge development observed in vivo (left panel). As the cell constricts its surface, surface tension is relieved in a centripetally moving wave, promoting peg coalescence in a similar pattern. For comparison, right panel shows constriction in response to the spatially homogeneous increase in active stress. Frame rate is 14 frames/s.

Video 1-3. NMII (Myl12.1-EGFP) contractions in the apical cortex pull on actin microridges (Lifeact-Ruby) of periderm cells at various stages in microridge development, indicated by title cards. All images are maximum intensity projections; time stamp represents minutes:seconds. Frame rate is 5 frames/s.

Video 1-4. Live imaging of Lifeact-GFP in 16 hpf periderm cells, beginning 3 min after exposure to high-salt media. All images are maximum intensity projections; time stamp represents minutes:seconds. Frame rate is 10 frames/s.

Video 1-5. Live imaging of Lifeact-GFP in 16 hpf periderm cells, beginning immediately after ablation of periderm cells on opposite sides of the central cell. All images are maximum intensity projections; time stamp represents minutes:seconds. Frame rate is 10 frames/s.

Video 1-6. In silico simulation of uniaxial elongation of a model rectangular cell. Left panel shows pattern formation in the absence of sensitivity to anisotropic flow (ε=0). Right panel shows pattern formation with surface tension depending on underlying anisotropic actomyosin flow. Frame rate is 14 frames/s.

References

Atilgan, E., D. Wirtz, and S.X. Sun. 2006. Mechanics and dynamics of actin-driven thin membrane protrusions. *Biophys. J.* 90:65–76.

Balaban, N.Q., U.S. Schwarz, D. Riveline, P. Goichberg, G. Tzur, I. Sabanay, D. Mahalu, S. Safran, A. Bershadsky, L. Addadi, and B. Geiger. 2001. Force and focal adhesion assembly: a close relationship studied using elastic micropatterned substrates. *Nat. Cell Biol.* 3:466–472.

Behrndt, M., G. Salbreux, P. Campinho, R. Hauschild, F. Oswald, J. Roensch, S.W. Grill, and C.-P. Heisenberg. 2012. Forces driving epithelial spreading in zebrafish gastrulation. *Science*. 338:257–260.

Ben Isaac, E., U. Manor, B. Kachar, A. Yochelis, and N.S. Gov. 2013. Linking actin networks and cell membrane via a reaction-diffusion-elastic description of nonlinear filopodia initiation. *Phys. Rev. E Stat. Nonlin. Soft Matter Phys.* 88:022718.

Bereiter-Hahn, J., M. Osborn, K. Weber, and M. Vöth. 1979. Filament organization and formation of microridges at the surface of fish epidermis. *J. Ultrastruct. Res.* 69:316–330.

Bertet, C., L. Sulak, and T. Lecuit. 2004. Myosin-dependent junction remodelling controls planar cell intercalation and axis elongation. *Nature*. 429:667–671.

Bischofs, I.B., S.S. Schmidt, and U.S. Schwarz. 2009. Effect of adhesion geometry and rigidity on cellular force distributions. *Phys. Rev. Lett.* 103:048101.

Blanchard, G.B., S. Murugesu, R.J. Adams, A. Martinez-Arias, and N. Gorfinkiel. 2010. Cytoskeletal dynamics and supracellular organisation of cell shape fluctuations during dorsal closure. *Development*. 137:2743–2752.

Blanchoin, L., R. Boujemaa-Paterski, C. Sykes, and J. Plastino. 2014. Actin dynamics, architecture, and mechanics in cell motility. *Physiol. Rev.* 94:235–263.

Blankenship, J.T., S.T. Backovic, J.S.P. Sanny, O. Weitz, and J.A. Zallen. 2006. Multicellular rosette formation links planar cell polarity to tissue morphogenesis. *Dev. Cell*. 11:459–470.

Bray, D., and J.G. White. 1988. Cortical flow in animal cells. *Science*. 239:883–888.

Buccione, R., J.D. Orth, and M.A. McNiven. 2004. Foot and mouth: podosomes, invadopodia and circular dorsal ruffles. *Nat. Rev. Mol. Cell Biol.* 5:647–657.

Cao, L.G., and Y.L. Wang. 1990. Mechanism of the formation of contractile ring in dividing cultured animal cells. II. Cortical movement of microinjected actin filaments. *J. Cell Biol.* 111:1905–1911.

Clark, A.G., K. Dierkes, and E.K. Paluch. 2013. Monitoring actin cortex thickness in live cells. *Biophys. J.* 105:570–580.

Daniels, D.R., J.C. Wang, R.W. Briehl, and M.S. Turner. 2006. Deforming biological membranes: how the cytoskeleton affects a polymerizing fiber. *J. Chem. Phys.* 124:024903.

David, D.J.V., A. Tishkina, and T.J.C. Harris. 2010. The PAR complex regulates pulsed actomyosin contractions during amnioserosa apical constriction in Drosophila. *Development*. 137:1645–1655.

DeBiasio, R.L., G.M. LaRocca, P.L. Post, and D.L. Taylor. 1996. Myosin II transport, organization, and phosphorylation: evidence for cortical flow/solation-contraction coupling during cytokinesis and cell locomotion. *Mol. Biol. Cell*. 7:1259–1282.

Depasquale, J.A. 2018. Actin Microridges: ACTIN MICRORIDGES IN EPITHELIUM. *Anat. Rec.*

31:81.

Derényi, I., F. Jülicher, and J. Prost. 2002. Formation and interaction of membrane tubes. *Phys. Rev. Lett.* 88:238101.

Fernández, B.G., A.M. Arias, and A. Jacinto. 2007. Dpp signalling orchestrates dorsal closure by regulating cell shape changes both in the amnioserosa and in the epidermis. *Mech. Dev.* 124:884–897.

Fischer-Friedrich, E., A.A. Hyman, F. Jülicher, D.J. Müller, and J. Helenius. 2014. Quantification of surface tension and internal pressure generated by single mitotic cells. *Sci. Rep.* 4:6213.

Gierer, A., and H. Meinhardt. 1972. A theory of biological pattern formation. *Kybernetik*. 12:30–39.

Gorelik, J., A.I. Shevchuk, G.I. Frolenkov, I.A. Diakonov, M.J. Lab, C.J. Kros, G.P. Richardson, I. Vodyanoy, C.R.W. Edwards, D. Klenerman, and Y.E. Korchev. 2003. Dynamic assembly of surface structures in living cells. *Proc. Natl. Acad. Sci. U. S. A.* 100:5819–5822.

Gov, N.S. 2006. Dynamics and morphology of microvilli driven by actin polymerization. *Phys. Rev. Lett.* 97:018101.

Gov, N.S., and A. Gopinathan. 2006. Dynamics of membranes driven by actin polymerization. *Biophys. J.* 90:454–469.

Gov, N., A.G. Zilman, and S. Safran. 2003. Cytoskeleton confinement and tension of red blood cell membranes. *Phys. Rev. Lett.* 90:228101.

Helfrich, W. 1973. Elastic properties of lipid bilayers: theory and possible experiments. *Z. Naturforsch. C*. 28:693–703.

Helker, C.S.M., A. Schuermann, T. Karpanen, D. Zeuschner, H.-G. Belting, M. Affolter, S. Schulte-Merker, and W. Herzog. 2013. The zebrafish common cardinal veins develop by a novel mechanism: lumen ensheathment. *Development*. 140:2776–2786.

Kabaso, D., R. Shlomovitz, K. Schloen, T. Stradal, and N.S. Gov. 2011. Theoretical model for cellular shapes driven by protrusive and adhesive forces. *PLoS Comput. Biol.* 7:e1001127.

Khaliullin, R.N., R.A. Green, L.Z. Shi, J.S. Gomez-Cavazos, M.W. Berns, A. Desai, and K. Oegema. 2018. A positive-feedback-based mechanism for constriction rate acceleration during cytokinesis in Caenorhabditis elegans. *Elife*. 7. doi:10.7554/eLife.36073.

Kwan, K.M., E. Fujimoto, C. Grabher, B.D. Mangum, M.E. Hardy, D.S. Campbell, J.M. Parant, H.J. Yost, J.P. Kanki, and C.-B. Chien. 2007. The Tol2kit: a multisite gateway-based construction kit for Tol2 transposon transgenesis constructs. *Dev. Dyn.* 236:3088–3099.

Lam, P.-Y., S. Mangos, J.M. Green, J. Reiser, and A. Huttenlocher. 2015. In vivo imaging and characterization of actin microridges. *PLoS One*. 10:e0115639.

Lan, Y., and G.A. Papoian. 2008. The stochastic dynamics of filopodial growth. *Biophys. J.* 94:3839–3852.

Legland, D., I. Arganda-Carreras, and P. Andrey. 2016. MorphoLibJ: integrated library and plugins for mathematical morphology with ImageJ. *Bioinformatics*. 32:3532–3534.

Lomakin, A.J., K.-C. Lee, S.J. Han, D.A. Bui, M. Davidson, A. Mogilner, and G. Danuser. 2015. Competition for actin between two distinct F-actin networks defines a bistable switch for cell polarization. *Nat. Cell Biol.* 17:1435–1445.

Maître, J.-L., H. Berthoumieux, S.F.G. Krens, G. Salbreux, F. Jülicher, E. Paluch, and C.-P. Heisenberg. 2012. Adhesion functions in cell sorting by mechanically coupling the cortices of

adhering cells. *Science*. 338:253–256.

Marchetti, M.C., J.F. Joanny, S. Ramaswamy, T.B. Liverpool, J. Prost, M. Rao, and R.A. Simha. 2013. Hydrodynamics of soft active matter. *Rev. Mod. Phys.* 85:1143–1189.

Marston, D.J., C.D. Higgins, K.A. Peters, T.D. Cupp, D.J. Dickinson, A.M. Pani, R.P. Moore, A.H. Cox, D.P. Kiehart, and B. Goldstein. 2016. MRCK-1 Drives Apical Constriction in C. elegans by Linking Developmental Patterning to Force Generation. *Curr. Biol.* 26:2079–2089.

Martin, A.C., and B. Goldstein. 2014. Apical constriction: themes and variations on a cellular mechanism driving morphogenesis. *Development*. 141:1987–1998.

Martin, A.C., M. Kaschube, and E.F. Wieschaus. 2009. Pulsed contractions of an actin-myosin network drive apical constriction. *Nature*. 457:495–499.

Mason, F.M., M. Tworoger, and A.C. Martin. 2013. Apical domain polarization localizes actin-myosin activity to drive ratchet-like apical constriction. *Nat. Cell Biol.* 15:926–936.

Matsumura, F. 2005. Regulation of myosin II during cytokinesis in higher eukaryotes. *Trends Cell Biol.* 15:371–377.

Mogilner, A., and G. Oster. 2003. Force generation by actin polymerization II: the elastic ratchet and tethered filaments. *Biophys. J.* 84:1591–1605.

Mogilner, A., and B. Rubinstein. 2005. The physics of filopodial protrusion. *Biophys. J.* 89:782–795.

Munjal, A., J.-M. Philippe, E. Munro, and T. Lecuit. 2015. A self-organized biomechanical network drives shape changes during tissue morphogenesis. *Nature*. 524:351–355.

Nolen, B.J., N. Tomasevic, A. Russell, D.W. Pierce, Z. Jia, C.D. McCormick, J. Hartman, R.

Sakowicz, and T.D. Pollard. 2009. Characterization of two classes of small molecule inhibitors of Arp2/3 complex. *Nature*. 460:1031–1034.

O'Brien, G.S., S. Rieger, S.M. Martin, A.M. Cavanaugh, C. Portera-Cailliau, and A. Sagasti. 2009. Two-photon axotomy and time-lapse confocal imaging in live zebrafish embryos. *J. Vis. Exp.* doi:10.3791/1129.

Olson, K.R., and P.O. Fromm. 1973. A scanning electron microscopic study of secondary lamellae and chloride cells of rainbow trout (Salmo gairdneri). *Z. Zellforsch. Mikrosk. Anat.* 143:439–449.

Pinto, C.S., A. Khandekar, R. Bhavna, P. Kiesel, G. Pigino, and M. Sonawane. 2019. Microridges are apical epithelial projections formed of F-actin networks that organize the glycan layer. *Sci. Rep.* 9:12191.

Pollard, T.D. 2016. Actin and Actin-Binding Proteins. *Cold Spring Harb. Perspect. Biol.* 8. doi:10.1101/cshperspect.a018226.

Pollard, T.D., and J.A. Cooper. 2009. Actin, a central player in cell shape and movement. *Science*. 326:1208–1212.

Prost, J., F. Jülicher, and J.-F. Joanny. 2015. Active gel physics. *Nat. Phys.* 11:111.

Raman, R., I. Damle, R. Rote, S. Banerjee, C. Dingare, and M. Sonawane. 2016. aPKC regulates apical localization of Lgl to restrict elongation of microridges in developing zebrafish epidermis. *Nat. Commun.* 7:11643.

Rasmussen, J.P., G.S. Sack, S.M. Martin, and A. Sagasti. 2015. Vertebrate epidermal cells are broad-specificity phagocytes that clear sensory axon debris. *J. Neurosci.* 35:559–570.

Ratheesh, A., G.A. Gomez, R. Priya, S. Verma, E.M. Kovacs, K. Jiang, N.H. Brown, A. Akhmanova, S.J. Stehbens, and A.S. Yap. 2012. Centralspindlin and α-catenin regulate Rho signalling at the epithelial zonula adherens. *Nat. Cell Biol.* 14:818–828.

Rauzi, M., P.-F. Lenne, and T. Lecuit. 2010. Planar polarized actomyosin contractile flows control epithelial junction remodelling. *Nature*. 468:1110–1114.

Roh-Johnson, M., G. Shemer, C.D. Higgins, J.H. McClellan, A.D. Werts, U.S. Tulu, L. Gao, E. Betzig, D.P. Kiehart, and B. Goldstein. 2012. Triggering a cell shape change by exploiting preexisting actomyosin contractions. *Science*. 335:1232–1235.

Rosenblatt, J., M.C. Raff, and L.P. Cramer. 2001. An epithelial cell destined for apoptosis signals its neighbors to extrude it by an actin- and myosin-dependent mechanism. *Curr. Biol.* 11:1847–1857.

Rotty, J.D., and J.E. Bear. 2014. Competition and collaboration between different actin assembly pathways allows for homeostatic control of the actin cytoskeleton. *Bioarchitecture*. 5:27–34.

Schindelin, J., I. Arganda-Carreras, E. Frise, V. Kaynig, M. Longair, T. Pietzsch, S. Preibisch, C. Rueden, S. Saalfeld, B. Schmid, J.-Y. Tinevez, D.J. White, V. Hartenstein, K. Eliceiri, P. Tomancak, and A. Cardona. 2012. Fiji: an open-source platform for biological-image analysis. *Nat. Methods*. 9:676–682.

Solon, J., A. Kaya-Copur, J. Colombelli, and D. Brunner. 2009. Pulsed forces timed by a ratchet-like mechanism drive directed tissue movement during dorsal closure. *Cell*. 137:1331–1342.

Sonal, J. Sidhaye, M. Phatak, S. Banerjee, A. Mulay, O. Deshpande, S. Bhide, T. Jacob, I. Gehring, C. Nuesslein-Volhard, and M. Sonawane. 2014. Myosin Vb mediated plasma membrane homeostasis regulates peridermal cell size and maintains tissue homeostasis in

the zebrafish epidermis. *PLoS Genet.* 10:e1004614.

Sperry, D.G., and R.J. Wassersug. 1976. A proposed function for microridges on epithelial cells. *Anat. Rec.* 185:253–257.

Straight, A.F., A. Cheung, J. Limouze, I. Chen, N.J. Westwood, J.R. Sellers, and T.J. Mitchison. 2003. Dissecting temporal and spatial control of cytokinesis with a myosin II Inhibitor. *Science*. 299:1743–1747.

Straus, L.P. 1963. A Study of the Fine Structure of the So-Called Chloride Cell in the Gill of the Guppy Lebistes Reticulatus P. *Physiol. Zool.* 36:183–198.

Uehara, K., M. Miyoshi, and S. Miyoshi. 1988. Microridges of oral mucosal epithelium in carp, Cyprinus carpio. *Cell Tissue Res.* 251:547–553.

Uehara, K., M. Miyoshi, and S. Miyoshi. 1991. Cytoskeleton in microridges of the oral mucosal epithelium in the carp, Cyprinus carpio. *Anat. Rec.* 230:164–168.

Zihni, C., and S.J. Terry. 2015. RhoGTPase signalling at epithelial tight junctions: Bridging the GAP between polarity and cancer. *Int. J. Biochem. Cell Biol.* 64:120–125.

Chapter 3

Cortical myosin minifilaments orchestrate the arrangement of microridge protrusions on epithelial cell surfaces

Authors:

Aaron P. van Loon[1], Ivan S. Erofeev[2], Andrew B. Goryachev[2], and Alvaro Sagasti[1,*]

Affiliation:

1. Department of Molecular, Cell and Developmental Biology, and Molecular Biology Institute, University of California, Los Angeles, Los Angeles, CA

2. Centre for Synthetic and Systems Biology, School of Biological Sciences, University of Edinburgh, Edinburgh, UK

Abstract

Actin-based protrusions vary in morphology, stability, and arrangement on cell surfaces. Microridges are laterally-elongated protrusions arranged in maze-like patterns on mucosal

epithelial cells that rearrange dynamically by fission and fusion. To characterize how microridges mature and investigate the mechanisms driving fission and fusion, we imaged microridges in the maturing skin of zebrafish larvae. After their initial development, microridges continued to lengthen and microridge alignment became increasingly well ordered. Imaging F-actin and Non-Muscle Myosin II (NMII) revealed that microridge fission and fusion were associated with local NMII activity in the apical cortex. Inhibiting NMII blocked rearrangements, reduced microridge density, and altered microridge spacing. High-resolution imaging revealed that individual cortical NMII minifilaments are tethered to protrusions, often connecting adjacent microridges. NMII minifilaments connecting the ends of microridges fused them together, whereas minifilaments oriented perpendicular to microridges severed them or pulled them closer together. Our findings demonstrate that as cells mature, microridges continue to remodel and form an increasingly orderly arrangement through a process orchestrated by cortical NMII contraction.

Introduction

Cells create diverse actin-based protrusions to carry out a wide variety of functions. Not only do protrusions vary in shape and size, but also in persistence, dynamics, and their relative arrangement on cells. For example, lamellipodia extend and retract within seconds or minutes (Giannone et al., 2007), whereas invadopodia persist for hours (Murphy and Courtneidge, 2011), and stereocilia are stable throughout an animal's life (Narayanan et al., 2015; Zhang et al., 2012). The stability and plasticity of protrusions depends on the regulation of their constituent actin filaments, but those regulatory mechanisms vary. For example, despite the fact that microvilli maintain a relatively stable height, actin filaments within them are constantly turned over (Loomis et al., 2003; Meenderink et al., 2019; Tyska and Mooseker, 2002). By contrast, the stability of stereocilia reflects extreme stability of their actin filaments, which persist for months (Narayanan

et al., 2015; Zhang et al., 2012). The motility and relative arrangement of protrusions on cells are also regulated by diverse mechanisms. For instance, microvilli move rapidly and independently on cell surfaces (Meenderink et al., 2019), but form stable clusters by establishing protocadherin-based connections at their tips (Crawley et al., 2014; Meenderink et al., 2019). Stereocilia, on the other hand, form highly stable and stereotyped arrangements on cells, and their orientation is strictly dictated by planar cell polarity (Tarchini and Lu, 2019). Identifying mechanisms regulating the stability and arrangement of protrusions is critical to understanding how cell surfaces acquire diverse morphologies and adapt to tissue-level changes.

Microridges are laterally-elongated protrusions arranged in elaborate patterns on the apical surfaces of mucosal epithelial cells (Depasquale, 2018). Neighboring microridges tend to align parallel to one another, filling cell surfaces in maze-like arrangements. Although microridges are less studied than other protrusions, recent work in zebrafish periderm cells, which form the most superficial layer of the skin, have begun to identify mechanisms underlying microridge morphogenesis. Distinct from other protrusions that emerge and extend as unitary structures, microridges form from the coalescence of finger-like precursor protrusions called pegs (Lam et al., 2015; Pinto et al., 2019; van Loon et al., 2020). Microridge development requires specification of apical-basal cell polarity (Magre et al., 2019; Raman et al., 2016), activity of the branched actin nucleation complex Arp2/3 (Lam et al., 2015; Pinto et al., 2019; van Loon et al., 2020), Plakin cytolinkers (Inaba et al., 2020), keratin filaments (Inaba et al., 2020), and cortical non-muscle myosin II (NMII) contraction, which concomitantly promotes apical constriction (Lam et al., 2015; Pinto et al., 2019; van Loon et al., 2020). Like microvilli, actin filaments within microridges constantly turn over (Lam et al., 2015), but the recruitment of keratin filaments by Plakin cytolinkers helps preserve microridge structure in the face of actin turnover (Inaba et al., 2020). Microridges exhibit unusual dynamics, undergoing fission and fusion to form new patterns (Lam

et al., 2015). How microridge patterns mature after their initial formation has not been determined, and the molecular mechanisms executing fission and fusion are unknown.

The membranes of epithelial cells associate with a thin actomyosin filament network, called the cortex (Kelkar et al., 2020). NMII forms bipolar minifilaments within the cortex, which contract actin filaments to generate forces that regulate membrane tension, cytokinesis, and cellular morphogenesis (Kelkar et al., 2020; Martin and Goldstein, 2014). Both the density and specific arrangement of NMII minifilaments influence cortical contractility (Kelkar et al., 2020). The cortical network is attached to cell junctions, and pulls them to constrict apical surfaces during a variety of morphogenetic events (Martin and Goldstein, 2014). Cortical contraction also regulates protrusion morphogenesis. For example, contraction stimulates actin treadmilling to regulate microvillar length (Chinowsky et al., 2020). In zebrafish periderm cells, pulsatile NMII activity lowers apical membrane tension to permit the formation and elongation of microridges from peg precursors (van Loon et al., 2020). Cortical NMII contraction continues in these cells after microridges have formed (van Loon et al., 2020), but the functional significance of these later contractile events is unknown.

In this study, we characterized microridge dynamics and patterning as cells matured, and investigated the role of NMII in these processes. We found that after initial development, fission and fusion continuously remodel microridges, but these events dampen as development proceeds. High-resolution imaging revealed that cortical NMII minifilaments connect adjacent microridges, and that their specific orientation relative to microridges dictates the nature of rearrangements. These findings demonstrate that cortical NMII minifilaments are not only required for microridge formation, but also regulate microridge fission, fusion, and alignment to pattern maturing epithelial cell surfaces.

Results

Microridge patterns mature in larval zebrafish

To determine how microridge spacing and patterning change as the developing zebrafish skin matures, we imaged zebrafish periderm cells expressing the F-actin reporter Lifeact-GFP (Riedl et al., 2008) in 48, 72 and 96 hours post-fertilization (hpf) fish (**Fig 1A**). Microridges had already formed and elongated by 48 hpf, but became longer on average during this period (**Fig S1A-B**), likely reflecting a specific reduction in pegs and short microridges (**Fig S1C**). Total microridge density on the apical surface increased between 48 and 96hpf (**Fig 1B**), which could result from an increase in microridges or reduced apical area. However, apical cell areas were not reduced, but were in fact slightly larger at 96hpf than at 48 or 72hpf (**Fig S1D**). Since microridge development occurs in tandem with apical constriction during early development (van Loon et al., 2020), these observations suggest that changes to microridges after 48hpf represent a distinct maturation process.

One of the most striking features of microridges is their regularly spaced and aligned arrangement, reminiscent of the parallel organization of molecules in liquid crystals, referred to as a “nematic” organization (Needleman and Dogic, 2017). To investigate how microridge spacing changes as cells mature, we measured the distance between every point on each microridge and the nearest point on a neighboring microridge (**Fig 1C-D**). The mode, median, and mean distances between microridges were similar between the three different stages (**Fig 1E, S1E-F**) and, as expected, corresponded to the orthogonal distance between aligned microridges (**Fig 1C**). However, spacing variability decreased over time (**Fig 1F**), suggesting that initially variable microridge spacing matured towards a specific spacing distance.

To determine how microridge alignment changes as microridge spacing becomes less variable, we color coding regions of cells containing microridges aligned in the same orientation.

This analysis revealed that the number of domains with aligned microridges decreased, and each domain increased in area, over time (**Fig 1G-H**). These observations demonstrate that microridges increasingly align parallel to one another as the skin develops.

To determine if population-level changes in microridge patterning reflect microridge maturation in individual cells, we scatter-labeled periderm cells with RFP, enabling us to identify the same cells day-to-day, and thus track how microridge spacing and alignment change over time. Although each cell behaved differently, on average, microridge density increased, spacing became less variable, and microridges increasingly aligned between 48 and 96hpf (**Fig 2**), demonstrating that population-level trends in microridge arrangement reflect the maturation of microridge patterning in individual cells towards a nematic pattern.

Microridges continuously rearrange

To determine the mechanism by which microridge patterns change over time, we performed time-lapse imaging of periderm cells expressing Lifeact-GFP at 30-second intervals. At each developmental stage, pegs, the finger-like precursor protrusions that coalesce to form microridges, continued to dynamically appear within and between microridges (**Video 2-1**), likely contributing to microridge lengthening. As previously observed (Lam et al., 2015), microridges underwent two types of rearrangements that altered their pattern. First, intact microridges sometimes broke apart into two separate microridges; second, two separate microridges sometimes fused end-to-end to form a longer microridge (**Fig 3A, Video 2-1 and 2-2**). Imaging a reporter for the plasma membrane demonstrated that these events reflect fission or fusion of the whole protrusion, not just of its internal actin structure (**Figure 3B, Video 2-3**). As microridges matured, rearrangement events decreased from 0.362 events/μm·min at 48 hpf to 0.155 and 0.115 events/μm·min at 72 and 96 hpf, respectively (**Fig 3C, Video 2-1**). Fission and fusion events occurred with roughly equal frequency, and this proportion did not change over time (**Fig 3D**), but

the frequency of these rearrangements decreased as the pattern matured (**Fig 3E**, Spearman Correlation Coefficient = -0.832).

Cell stretching does not induce microridge rearrangement

Periderm cells are constantly pushed and pulled by neighboring cells as the epidermis grows. We therefore speculated that microridge fission and fusion may be induced by forces associated with cell shape distortion. To test this idea, we ablated periderm cells on either side of an observed cell using a laser on a 2-photon microscope (O'Brien et al., 2009b; van Loon et al., 2020). This procedure caused the central cell to stretch between the two wounds, and often pucker or bulge in the orthogonal axis. Surprisingly, cell elongation did not increase microridge fission or fusion, but simply distorted microridges to accommodate the cells' new shapes (**Fig 3F**, **Video 2-4**). This observation suggests that microridges do not undergo fission or fusion simply as a result of cellular distortion, and thus implies that remodeling events are actively regulated.

Microridge rearrangements require cortical NMII contraction

The apical cortex of periderm cells experiences pulsatile NMII-based contractions through at least 48 hpf (van Loon et al., 2020). These contractions are required for apical constriction and the coalescence of peg precursors to form and elongate microridges (van Loon et al., 2020), but later functions have not been described. To test if cortical contraction affects microridge fission or fusion events, we made time-lapse videos of periderm cells expressing fluorescent reporters for both F-actin (Lifeact-Ruby) and NMII (Myl12.1-EGFP) (Maître et al., 2012; van Loon et al., 2020). At 48hpf, periderm cells displayed local pulses of NMII reporter fluorescence in the apical cortex (**Fig 4A**, **Video 2-5**), which we previously found to reflect NMII contraction (van Loon et al., 2020). Many of these contraction events correlated spatially and temporally with microridge rearrangements (**Fig 4A**). To quantify this correlation, we measured the distance between microridge rearrangement events and the nearest detectable NMII contractile pulse in the same

frame. On average, 41% of microridge rearrangements occurred within 1μm of an NMII contraction (**Fig 4B**). By contrast, when the NMII reporter channel was rotated 90°, only 22% occurred within 1μm of a contraction (**Fig 4B**), indicating that the coincidence between contraction and rearrangement events did not occur by chance. These observations likely underestimate the number of rearrangement events associated with contraction, since contractions may be shorter-lasting or dimmer than we can detect with our reporter. NMII contractions equally correlated with fission and fusion events (**Fig 4C**).

To directly test if NMII contraction is required for microridge rearrangements, we treated 48hpf fish with the specific NMII inhibitor blebbistatin (Straight et al., 2003) for one hour, then made 10-minute videos of periderm cells expressing Lifeact-GFP. NMII inhibition dramatically reduced fission and fusion compared to controls (**Fig 4D-E**, **Video 2-6**), demonstrating that NMII activity is required for microridge remodeling.

NMII contraction regulates microridge density and spacing

Given that NMII contraction promotes microridge rearrangements, and that these dynamic events negatively correlate with microridge alignment, we hypothesized that inhibiting NMII contraction may disrupt microridge maturation. To determine the long-term consequences of suppressing NMII activity, we treated zebrafish with blebbistatin for 24 hours, starting at 48hpf. Compared to controls, microridges in blebbistatin-treated animals were shorter, distributed less densely, and spaced more widely (**Fig 5A-E**). These observations indicate that microridges must be actively maintained by contraction, which may facilitate the incorporation of new pegs into established microridges. Blebbistatin also increased microridge alignment. This effect on alignment may be a consequence of the lower microridge density, since our alignment index measures the number of domains containing aligned microridges (**Fig 5B,D,F**), but could also indicate that suppressing contraction allows the system to settle into a local energy minimum (see

Discussion). Since long-term NMII inhibition can have deleterious, indirect effects on cells, we compared microridges on individual cells before and after 1-hour blebbistatin treatment. Similar to 24-hour treatment, 1-hour exposure to blebbistatin disrupted microridge spacing, decreasing density and increasing the microridge alignment index (**Fig 6**).

High-resolution imaging reveals individual NMII minifilaments in the cortex

Since NMII inhibition experiments could not disambiguate NMII's role in regulating microridge fission and fusion, length maintenance, and spacing, we addressed these questions by imaging NMII organization and activity in the periderm cortex directly. To image NMII and F-actin with improved spatial resolution, we used Airyscan microscopy (Weisshart, 2014). Using this approach, the NMII reporter often appeared as pairs of puncta (**Fig 7A**). The Myl12.1-EGFP NMII reporter is a fusion of EGFP to a myosin regulatory light chain (Maître et al., 2012; van Loon et al., 2020), which binds near myosin heads at opposing ends of NMII minifilaments. We thus speculated that puncta pairs represent ends of single bipolar minifilaments. Consistent with this possibility, the median distance between intensity maxima of NMII reporter doublets was 281nm (**Fig 7B**), similar to the reported length of bipolar minifilaments assembled in vitro (~300nm in length; (Billington et al., 2013)). To further test if these structures are individual minifilaments, we imaged periderm cells expressing reporters for both NMII light chain (Myl12.1-Ruby) and a C-terminally tagged NMII heavy chain (Myh9a-EGFP). A fluorophore at the C-terminus of NMII heavy chains should localize to the middle of minifilaments, between NMII heavy chain heads (**Fig 7C-D**). Puncta in periderm cells expressing both reporters were arranged in the expected alternating pattern (**Fig 7C-D**). Thus, our imaging system allows us to distinguish individual NMII minifilaments within the plane of the apical cortex in cells of living animals.

Cortical NMII minifilaments associate with pegs and microridges

To determine how NMII minifilaments are arranged relative to cell protrusions, we imaged them, along with F-actin, at several developmental stages. Prior to microridge formation (16 hpf), NMII minifilaments in the apical cortex were closely associated with microridge peg precursors (**Fig 7A**), and continued to associate with protrusions as pegs coalesced to form microridges. At 24 hpf, NMII minifilaments were often attached to two separate microridges, bridging them end-to-end or side-to-side (**Fig 7E**). This organization was maintained as microridges matured: At 48hpf many cortical NMII "bridges" formed perpendicular connections between adjacent microridges, often appearing to consist of two end-to-end minifilaments (**Fig 7E**).

NMII minifilaments orchestrate microridge rearrangement and spacing

To observe how the organization of NMII minifilaments in the cortex relates to protrusion dynamics, we made high-resolution videos of periderm cells expressing Lifeact-Ruby and Myl12.1-EGFP. During early morphogenesis, appearance and disappearance of pegs often correlated with appearance and disappearance of NMII reporter signal, and movement of pegs was associated with a corresponding movement of the NMII reporter (**Fig 8A, Video 2-7**), confirming that NMII minifilaments are tethered to protrusions. At later stages, when microridges remodel, the orientation of NMII minifilaments correlated with the type of microridge rearrangement observed. Minifilaments connecting the ends of two microridges appeared to pull them together, fusing them into a longer microridge (**Fig 8B, Video 2-7**). By contrast, minifilaments oriented perpendicular to microridges were often associated with fission events, which occurred at the point where microridges attached to the minifilaments (**Fig 8B, Video 2-7**). Minifilaments arranged perpendicular to microridges also appeared to regulate microridge spacing: the attachment of minifilaments to two parallel microridges appeared to bring them closer together, whereas their disappearance or detachment allowed the two microridges to drift apart (**Fig 8C, Video 2-7**). These observations suggest that the spatial organization of individual cortical

NMII minifilaments directs the rearrangement of microridges, regulating the spacing between them and thus altering the microridge pattern on the apical surface.

Discussion

Our study reveals that cortical NMII orchestrates a unique process for the patterning and maturation of microridges. Cells retain microridges on their surfaces for days, and likely even weeks, but, unlike extremely stable stereocilia, microridges continuously remodel through an NMII-mediated “recombination” process of fission and fusion as they mature towards a more ordered, nematic arrangement (**Fig 9**). Thus, at least during the first week of development, microridges are not permanent cell identifiers, like a fingerprint, but evolving structures that form new patterns over time.

Microridge pattern maturation minimizes surface energy

The increasing nematic order of maturing microridge patterns suggests that they are governed by an energy minimization principle, which can be explained with concepts defined by physics. Optimal parallel packing of microridges likely minimizes the bending and stretching energy of the lipid bilayer that is coupled to the underlying cortex. Consistent with this idea, we found that the size of local alignment domains increased, and their number decreased, as microridge patterns matured (**Fig 1, Fig 2**). Inevitably, initial disorder in the emerging pattern brings about sharp boundaries between the domains of local alignment. These boundaries are defects in the nematic order, and thus associated with an energy penalty, a phenomenon well-known in liquid crystals (Needleman and Dogic, 2017). The global energy minimum likely corresponds to concentric microridges arranged in parallel rings, like a target. Our observations show that microridge patterns, which are initially in states with many alignment domains, progress towards this well-ordered global minimum over time, a process that requires crossing energy

barriers associated with fission and fusion of preexisting microridges. However, this global minimum cannot be readily reached from an arbitrary state with multiple alignment domains without crossing energy barriers associated with fission and fusion of preexisting microridges.

Our results suggest that myosin activity facilitates the crossing of energy barriers, promoting fission and fusion and thus rearranging microridge patterns. The fact that myosin activity leads to microridge fission and fusion with approximately equal probability (**Fig 3D**) suggests that it does not increase their order or disorder per se, but rather provides quantal “kicks” that locally alter pattern topology. Thus, myosin activity is analogous to the thermodynamic temperature of the pattern--by randomly breaking and fusing individual microridges, myosin allows the pattern to cross energy barriers separating local energy minima. Following this thermodynamic analogy, the decrease in microridge rearrangement events over time corresponds to slowly lowering the temperature, or annealing, which is well-known in physics to help systems reach lower energy states on complex energy landscapes with multiple minima (van Laarhoven and Aarts, 1987). Blebbistatin may represent rapid quenching (a sharp temperature drop) that allows the system to descend into the closest energy minimum, perhaps explaining why blebbistatin in our experiments increased the alignment index.

Microridges are modular protrusions

Both the initial formation and remodeling of microridges demonstrate that they are modular structures: individual units (pegs) assemble into longer structures (microridges); once assembled, microridges can be broken at any point and attached to other microridges. This modular nature distinguishes microridges from other protrusions. However, the apparent simplicity of this process elides the complexity of rearrangement events at the molecular level, which likely involve multiple, locally regulated activities. Fission requires not just severing actin filaments, but also locally disassembling a supramolecular network of F-actin, keratin filaments, and actin-binding proteins

(Pinto et al., 2019), as well as membrane remodeling. Microridge remodeling events require NMII activity, but fission is likely instigated by upstream regulators that coordinate multiple biochemical activities. Such roles could be played by Rho family GTPases, which can regulate both F-actin stability and NMII contraction (Kelkar et al., 2020; Ridley, 2015), or Aurora B kinase, which promotes NMII activity (Minoshima et al., 2003; Touré et al., 2008) and disassembly of actin and keratin filaments (Field et al., 2019) at the cytokinetic furrow. Fusion likely requires F-actin polymerization, the activity of F-actin cross-linking proteins that link the cytoskeletal networks of the two parent microridges, and the reintegration of keratin filaments, which have the potential to connect with themselves end-to-end (Çolakoğlu and Brown, 2009). NMII activity may facilitate both fission and fusion by reducing surface tension, as it does during initial microridge formation (van Loon et al., 2020), and by physically pulling protrusions to rupture them or bring them together.

The orientation of cortical NMII minifilaments determines the nature of microridge rearrangements

Visualizing individual NMII minifilaments in the cortex of living cells provided insight into how they execute microridge rearrangements, as well as evidence that they play a direct role in microridge spacing (**Fig 9**). From the earliest steps of microridge morphogenesis, cortical minifilaments associate with protrusions. This observation suggests that the ends of individual minifilaments are biochemically tethered to the base of pegs and microridges, orthogonal to actin filaments in these protrusions. When two pegs are tethered to opposite ends of a minifilament, contraction brings them closer together, providing an opportunity for them to fuse into a nascent microridge. Similarly, contraction of peg-to-microridge minifilament bridges may contribute to microridge elongation, and contraction of minifilament bridges connecting two microridge ends may promote microridge fusion. The recruitment of keratin filaments into these growing protrusions likely helps stabilize them (Inaba et al., 2020), preventing fusion events from reversing. By contrast, minifilaments tethered to the sides of microridges sometimes promoted

fission, suggesting that minifilaments may pull on microridges to facilitate their local disassembly. If minifilaments bridged two parallel microridges, they often appeared to pull them closer together without severing them, providing direct evidence that NMII can regulate microridge spacing. At the later stages, microridges were often linked by a bridge of two perpendicular minifilaments aligned end-to-end. This arrangement raises the intriguing possibility that minifilaments could serve as molecular spacers for aligned microridges, similar to how spectrin tetramers determine the spacing of actin rings in axons (Xu et al., 2013). However, it is at least as likely that spacing length is determined by another factor, such as the minimization of membrane bending energy, and that minifilaments organize to accommodate that spacing.

Minifilaments are typically thought to be isotropically oriented in the cortex of interphase cells (Kelkar et al., 2020), but our findings suggest that their association with microridges causes them to adopt a highly organized arrangement in the cortex of periderm cells. In mature periderm cells, since microridges align with cell borders and with one another, their arrangement approximates an ideal target-like concentric pattern; because minifilaments form perpendicular bridges between adjacent microridges, they are predominantly arranged radially towards the center of cells. Since contractility is influenced not just by minifilament density, but also the relative arrangement of NMII in the cortex (Kelkar et al., 2020), this unusual radial minifilament organization likely endows periderm cells with unique contractile properties. Collectively, our observations reveal a surprisingly organized arrangement of cortical minifilaments, indicating that understanding how cortical contraction executes specific biological processes will require a better understanding of cortical minifilament architecture.

Materials and methods

Zebrafish

Zebrafish (*Danio rerio*) were raised at 28.5°C on a 14-h/10-h light/dark cycle. Embryos were raised at 28.5°C in embryo water composed of 0.3 g/Liter Instant Ocean salt (Spectrum Brands, Inc.) and 0.1% methylene blue. Previously characterized zebrafish lines in this paper include AB wild-type fish (ZFIN: ZDB-GENO-960809-7), Tg(krt5:Gal4) (Rasmussen et al., 2015), Tg(UAS:Lifeact-GFP) (Helker et al., 2013), Tg(krt5:Lifeact-Ruby), and Tg(krt5:Myl12.1-EGFP) (van Loon et al., 2020). Tg(krt5:Gal4/+;UAS:Lifeact-GFP/+) zebrafish were incrossed or outcrossed to WT and screened for brightness on the day of imaging using a fluorescence dissecting microscope. For Airyscan microscopy, Tg(krt5:Myl12.1-EGFP) zebrafish were incrossed and injected with krt5:Lifeact-Ruby and krt5:Myl12.1-EGFP plasmids to improve brightness. All experimental procedures were approved by the Chancellor's Animal Research Care Committee at the University of California, Los Angeles.

Plasmids

Previously characterized plasmids in this paper include krt5:Myl12.1-EGFP (van Loon et al., 2020) and UAS:mRuby-PH-PLC (Jiang et al., 2019). krt5-Myh9a-mCherry was constructed using the Gateway-based Tol2-kit (Kwan et al., 2007). The following vectors used to construct krt5-Myh9a-mCherry have previously been described: p5E-krt5 (Rasmussen et al., 2015), p3E-mCherrypA (Kwan et al., 2007), and pDestTol2pA2 (Kwan et al., 2007). The Myh9a coding sequence was cloned from a cDNA library of 5dpf zebrafish larvae using the following primers: Forward: 5'-GGGGACAAGTTTGTACAAAAAAGCAGGCTATATGTCAGACGCAGAGAAGTTC-3'; Reverse: 5'-GGGGACCACTTTGTACAAGAAAGCTGGGTCTTACTCAGGAGTTGGCTCG-3'.

For transient transgene expression, ~5 nL plasmid (~25 ng/µL) was injected into single cell zebrafish embryos.

Microscopy

Live fluorescent images and videos of periderm cells were acquired on a Zeiss LSM800 confocal microscope. Images were acquired with Zeiss Zen Blue software using an EC Plan-Neofluar 40×/1.30 oil DIC M27 objective with 2–3× digital zoom. Optimal resolution and Z-stack intervals were set using Zen software, except for videos for which a Z-stack interval of 0.75 µm was used to improve imaging speed. During imaging, zebrafish slide chambers were mounted on a heated stage set to 28°C. The x-y position and z-stack were occasionally adjusted during time-lapse imaging to keep the cells of interest in the frame. For longitudinal experiments between 48-96 hpf, zebrafish were rescued from mounting agarose each day after imaging using forceps, then placed in separate petri dishes for mounting and imaging on subsequent days.

Airyscan microscopy was performed on a Zeiss LSM 880 confocal microscope with Airyscan in the Broad Stem Cell Institute Research Center/Molecular, Cell and Developmental Biology microscopy core at UCLA. Images were acquired with Zeiss Zen Black software using an Plan-Apochromat 63x/1.4 Oil DIC M27 objective with 2–5× digital zoom. After acquisition, Airyscan processing was performed with the default settings on Zen Black.

To ablate periderm cells expressing Lifeact-GFP, we adapted a previously described method (O'Brien et al., 2009a; van Loon et al., 2020). Videos of cell stretching by periderm cell ablation were acquired using Zeiss Zen Black Software on a Zeiss LSM 880 multiphoton microscope using an EC Plan-Neofluar 40×/1.30 oil DIC M27 objective and a Coherent Chameleon Ultra II laser at a wavelength of 813 nm. A 488-nm laser was used to find and focus on the cell surface at 250× digital zoom, and the cell was then exposed to 813 nm laser illumination for 3–4 s at 5–6% laser power using "live" scanning.

Drug Treatment

(-)-Blebbistatin (Cayman Chemical) was dissolved in DMSO (Fisher Scientific). Treatment solutions were made with Ringer's Solution and included the inhibitor, or equivalent concentration

of DMSO (≤1%), as well as up to 0.4 mg/mL MS-222 (Sigma). Zebrafish larvae were exposed to the treatment solution for the specified period of time, then mounted in agarose and immersed in the same solution. For treatments longer than 2 hours, larvae were initially exposed to a treatment solution without MS-222 and then transferred to a similar solution containing up to 0.4 mg/mL MS-222 ≥30min prior to imaging. For longitudinal experiments with blebbistatin, fish were first mounted in agarose and imaged, then rescued from agarose using forceps and exposed to treatment solutions. Approximately 30 minutes after exposure to treatment solutions, zebrafish were again mounted in agarose and slide chambers were filled with treatment solution. Zebrafish were imaged again after 1-hour exposure to treatment solutions.

Image Analysis and Statistics

All statistical testing was performed using RStudio (RStudio, Inc.). Data distributions were assessed for normality using the Shapiro-Wilk test and visually inspected using Q-Q plots. The appropriate parametric or non-parametric tests were then selected based on the normality of the data distributions being compared.

Microridge analysis was performed using a custom Python script. Images of periderm cells were sum-projected and smoothened with a Gaussian filter. Pixel intensities were then normalized based on the modality of their intensity distribution. Unimodal distributions were normalized to the full width at the half maximum, while bimodal distributions were normalized to values between both maxima. Images were then processed with a Hessian filter, thresholded and skeletonized. Vectorized skeletons were smoothened and fitted to a normalized cell image to produce vectorized microridge lines. Distances between microridges and microridge orientations were then calculated. Microridge alignment domains were calculated by interpolating Q-tensor ($\mathbf{Q} = \mathbf{v} \otimes \mathbf{v} - \frac{1}{2}\mathbf{I}$, where $\mathbf{v}$ is a unit tangent vector and $\mathbf{I}$ is a unit tensor).

Image management for presentation was performed using FIJI (Schindelin et al., 2012). The brightness and contrast of images were adjusted for the purpose of presentation. All movies were stabilized for presentation and analysis purposes using the Image Stabilizer FIJI plugin ("Kang Li @ CMU - Image Stabilizer Plugin for ImageJ," n.d.).

Microridge fusion and fission events were identified manually using the FIJI Multi-point tool. To measure distances from NMII contractions to fusion and fission events, NMII images were smoothened and contractions were automatically thresholded in FIJI with the Triangle method, then distances were measured between microridge rearrangement events and the edge of the nearest contraction using 'rgeos' and 'sp' R packages.

Author Contributions

APvL, ISE, ABG, and AS conceived of and designed the study; APvL performed all zebrafish experiments; ISE designed computational analysis pipeline; APvL, ABG, and AS wrote the paper.

Acknowledgements

We thank Sally Horne-Badovinac, Yasuko Inaba, and Kadidia Pemba Adula for comments on the manuscript, Son Giang and Linda Dong for excellent fish care, and Nat Prunet in the BSCRC/MCDB microscopy core for help with Airyscan microscopy. This work was funded by National Institutes of Health grants R21EY024400 and R01GM122901 to A. Sagasti, and by the Biotechnology and Biological Sciences Research Council of UK grants BB/P01190X and BB/P006507 to A.B. Goryachev. A.P. van Loon was supported by the Ruth L. Kirschstein National Research Service Award (GM007185).

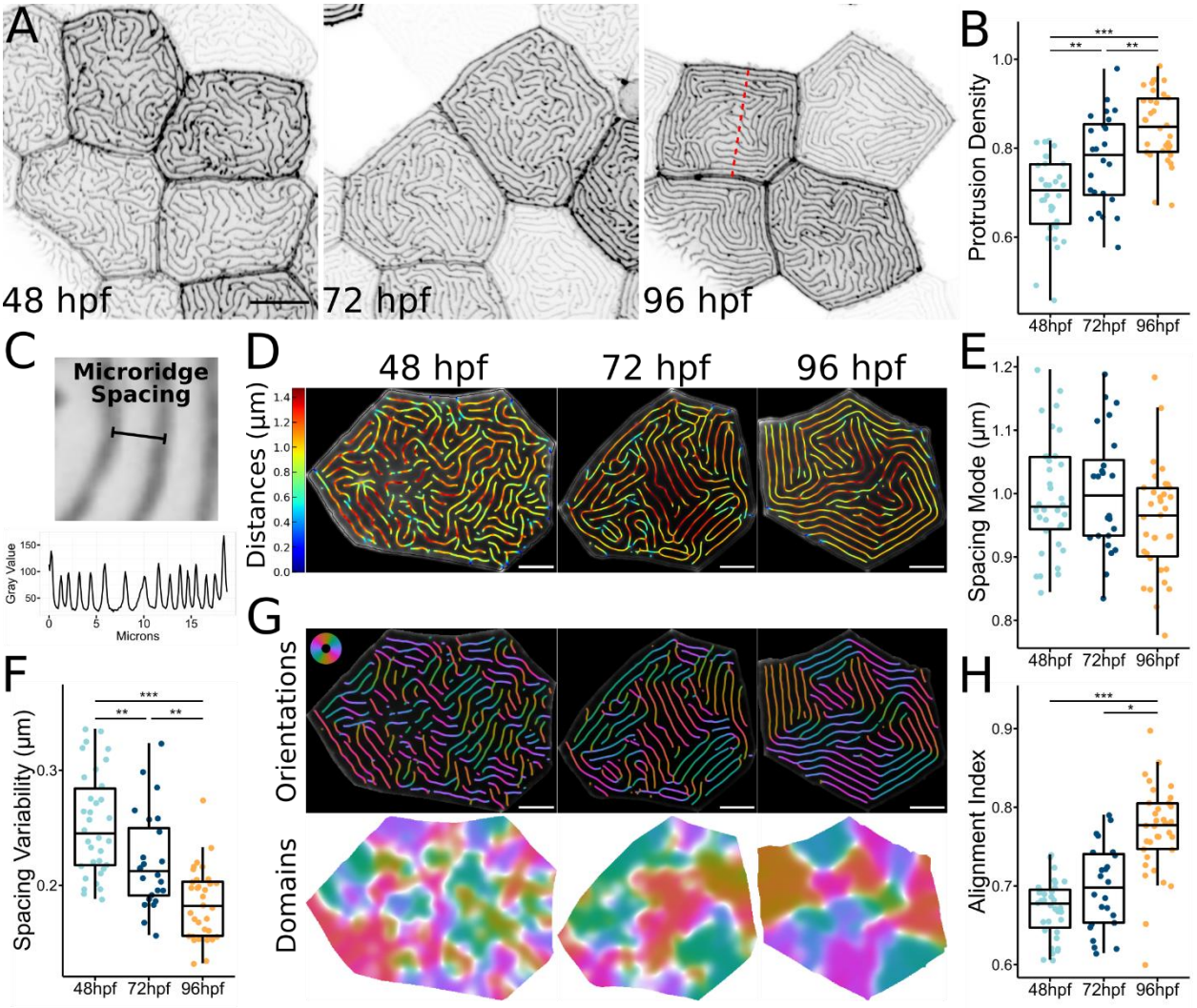

Figure 1. Microridge patterns mature over time. **(A)** Representative images of periderm cells expressing Lifeact-GFP in zebrafish larvae at the specified developmental stage. Images were inverted, so that high intensity fluorescence appears black and low intensity is white. **(B)** Dot and box-and-whisker plot of microridge density, defined as the sum microridge length (µm) normalized to apical cell area (µm^2), on periderm cells at the specified stage. 48 hpf, n=34 cells from 12 fish; 72 hpf, n=24 cells from 10 fish; 96 hpf, n=34 cells from 15 fish. P=1.87x10^{-9}, one-way ANOVA followed by Tukey's HSD test: 48-72 hpf, P=3.32x10^{-3}; 48-96 hpf, P=1.17x10^{-9}; 72-96 hpf, P=6.65x10^{-3}. **(C)** Top: diagram showing definition of microridge spacing distance. Microridge spacing was measured from a given point on a microridge to the nearest point on an adjacent

microridge. Bottom: profile plot of pixel intensity values across the width of a periderm cell expressing Lifeact-GFP on a 96 hpf zebrafish (indicated by dashed red line in A). **(D)** Visualization of microridge spacing in cells at the specified developmental stage. The distance to the nearest neighboring microridge is color-coded along microridges in each cell. Colors correspond to specific distances, as indicated on the bar to the left. **(E)** Dot and box-and-whisker plots of the mode distance between neighboring microridges in periderm cells at the specified stage. 48 hpf, n=34 cells from 12 fish; 72 hpf, n=24 cells from 10 fish; 96 hpf, n=34 cells from 15 fish. P=0.089, one-way ANOVA. **(F)** Dot and box-and-whisker plot of microridge spacing variability, defined as the interquartile range of distances, between neighboring microridges in periderm cells at the specified stage. 48 hpf, n=34 cells from 12 fish; 72 hpf, n=24 cells from, 10 fish; 96 hpf n=34 cells from 15 fish. $P=9.91x10^{-10}$, one-way ANOVA followed by Tukey's HSD test: 48-72 hpf, $P=7.72x10^{-3}$; 48-96 hpf, $P=8.11x10^{-10}$; 72-96 hpf, $P=1.90x10^{-3}$. **(G)** Visualization of microridge orientation at the specified stages. Microridge orientations are color-coded along each microridge (top). Colors correspond to the color wheel on the upper left. Microridge alignment domains were expanded from microridge orientations (bottom), using the same color wheel and scale as the above microridge orientations. See Methods for details. **(H)** Dot and box-and-whisker plot of the microridge alignment index for periderm cells at the specified stage. 48 hpf, n=34 cells from 12 fish; 72 hpf, n=24 cells from 10 fish; 96 hpf, n=34 cells from 15 fish. $P=2.96x10^{-12}$, one-way ANOVA followed by Tukey's HSD test: 48-72 hpf, P=0.121; 48-96 hpf, $P=4.02x10^{-10}$; 72-96 hpf, $P=8.79x10^{-7}$.

Scale bars: 10 μm (A) and 5 μm (D and G).

'*' $p \geq 0.05$, '**' $p \geq 0.01$, and '***' $p \geq 0.001$.

For box-and-whisker plots, middle box line is the median, and lower and upper ends of boxes are 25th and 75th percentiles, respectively.

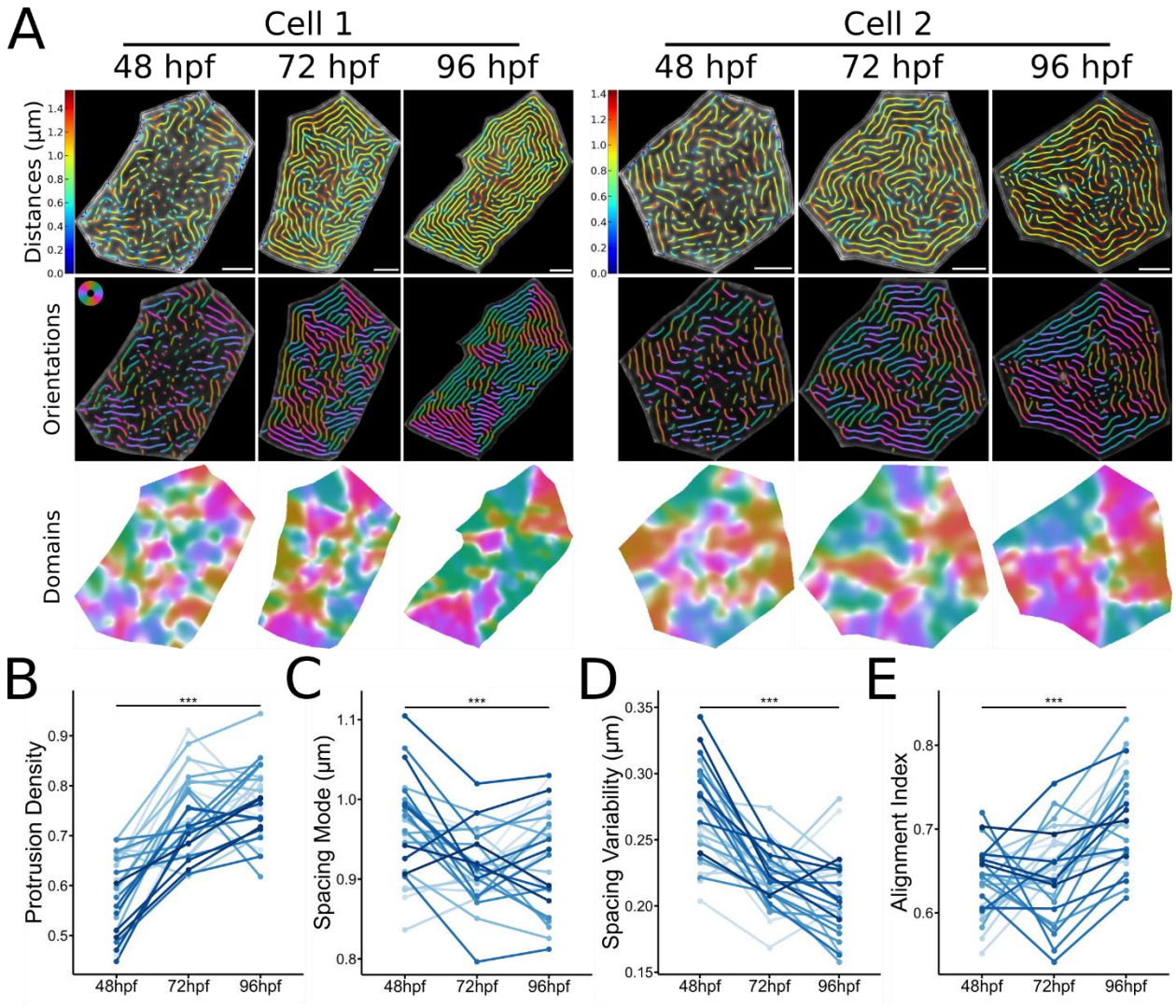

Figure 2. Microridge patterns mature on individual periderm cells. (A) Microridge distances, orientations, and alignment domains in two cells from 48-96 hpf. **(B)** Line and point plot of microridge density, defined as the sum microridge length (µm) normalized to apical cell area (µm^2), in periderm cells over time. n=28 cells from 9 fish. P=5.87x10^{-15}, one-way repeated measures ANOVA. **(C)** Line and point plot of the mode distances between neighboring microridges in periderm cells over time. n=28 cells from 9 fish. P=4.08x10^{-4}, one-way repeated measures ANOVA. **(D)** Line and point plot of microridge spacing variability (interquartile range of distances) between neighboring microridges in periderm cells over time. n=28 cells from 9 fish.

$P=7.37x10^{-11}$, one-way repeated measures ANOVA. **(E)** Line and point plot of microridge alignment index in periderm cells over time. n=28 cells from 9 fish. $P=5.16x10^{-8}$, one-way repeated measures ANOVA.

Scale bars: 5 μm (A).

'***' $p \geq 0.001$.

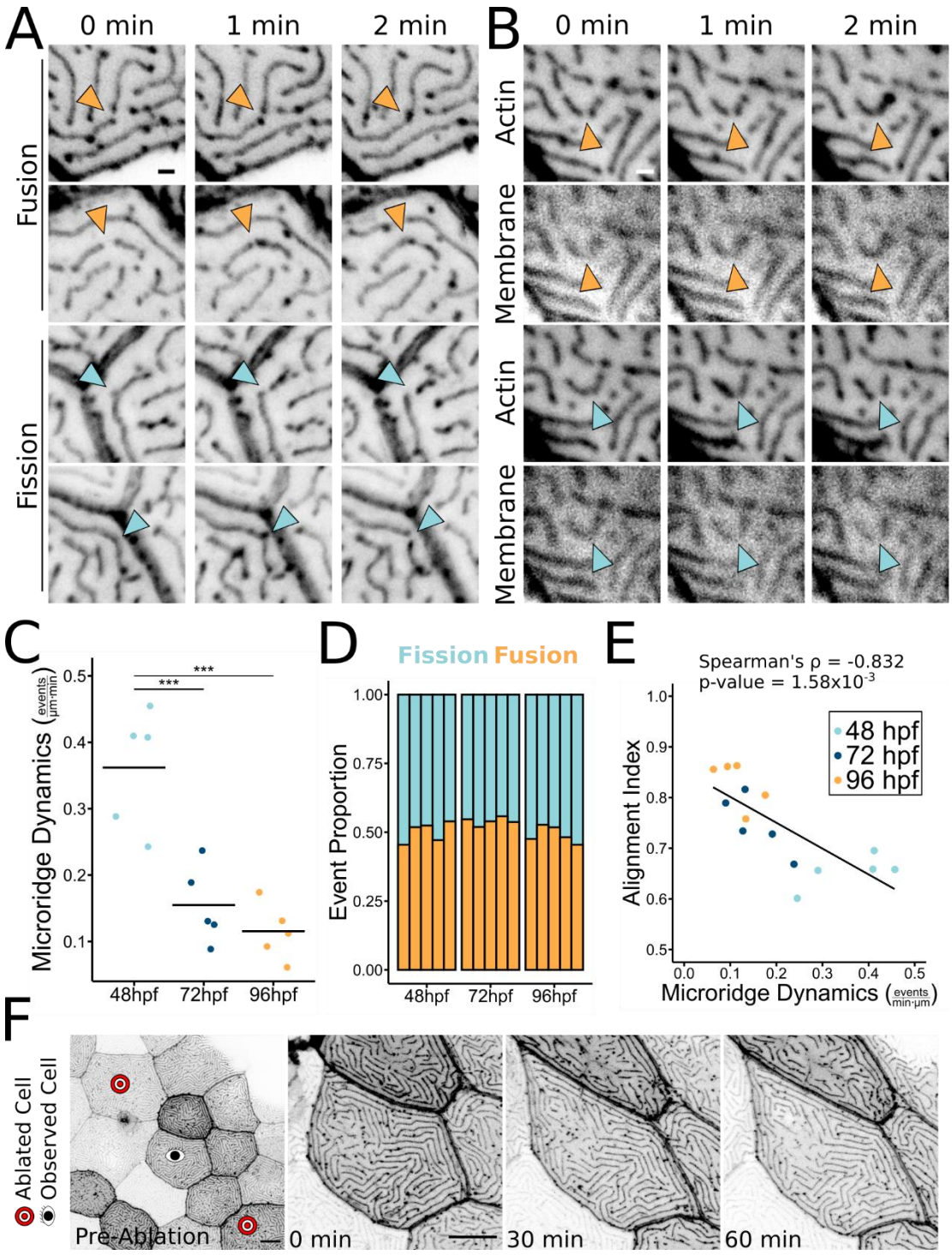

Figure 3. Microridges dynamically rearrange. (A) Time-lapse images of 48 hpf zebrafish periderm cells expressing Lifeact-GFP demonstrating microridges undergoing fission or fusion. Orange arrowheads indicate fusion; blue arrowheads indicate fission. Images were inverted, so

that high intensity fluorescence appears black and low intensity is white. Images are still frames from Video 2-2. (B) Time-lapse images of 48hpf zebrafish periderm cells expressing Lifeact-GFP (actin) and mRuby-PH-PLC (membrane) demonstrating microridges undergoing fission or fusion. Orange arrowheads indicate fusion; blue arrowheads indicate fission. Images were inverted, so that high intensity fluorescence appears black and low intensity is white. Images are still frames from Video 2-3. **(C)** Jittered dot plot of the sum of fission and fusion events in each cell, normalized to cell apical area, over a 10-minute period (events/μm·min) at the specified stage. Middle bar represents the mean. n=5 cells from 5 fish at all stages. $P=1.62x10^{-4}$, one-way ANOVA followed by Tukey's HSD test: 48-72 hpf, $P=9.75x10^{-4}$; 48-96 hpf, $P=2.17x10^{-4}$; 72-96 hpf, P=0.629. **(D)** Stacked bar plot of the proportion of fission and fusion events indicated stages. Each bar represents one cell. n=5 cells from 5 fish at all developmental stages. Fusion events were used in a Test of Equal Proportions (P=0.224) and fusion event proportion estimates were 0.501, 0.543, and 0.488 for 48, 72, and 96hpf, respectively. **(E)** Scatter plot of microridge dynamics (events/μm·min) over a 10-minute period versus the microridge alignment index at the start of the 10-minute period. n=5 cells from 5 fish at all developmental stages. $P=1.16x10^{-4}$, Spearman's rank correlation rho = -0.832. **(F)** Time-lapse image sequence of Lifeact-GFP-expressing periderm cells stretching in response to neighbor cell ablation on a 72 hpf zebrafish. Pre-ablation image shows the cell of interest between the ablated cells, and images of the cell of interest immediately after ablation (0 min) and at 30-minute intervals after ablation. The cell stretched dramatically, but microridge rearrangements did not appreciably increase. Images were inverted, so that high intensity fluorescence appears black and low intensity is white. Images are still frames from Video 2-4.

Scale bars: 1 μm (A and B) and 10 μm (E).

'***' $p \geq 0.001$.

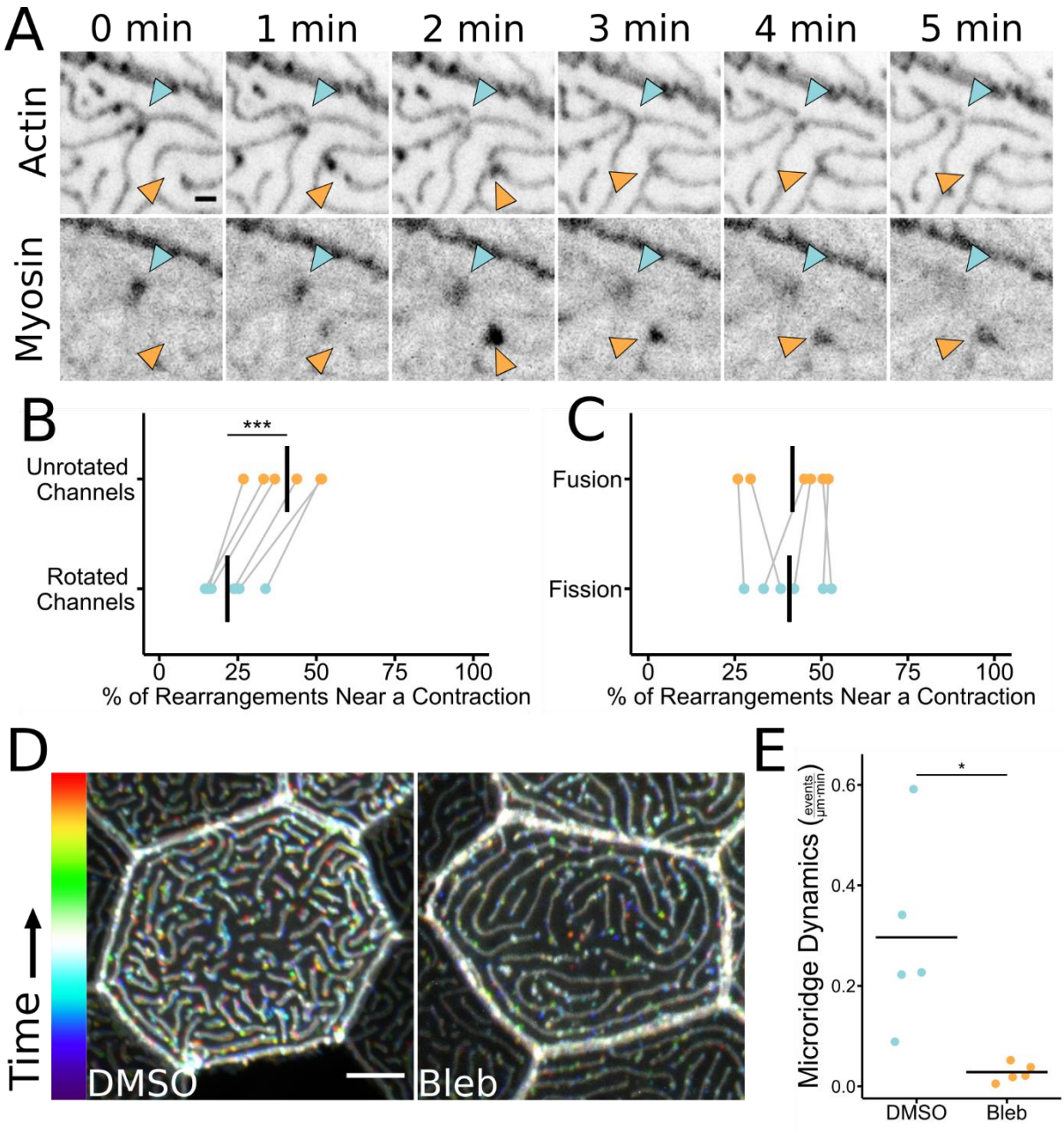

Figure 4. Microridge rearrangements spatially and temporally correlate with NMII contraction. (A) Time-lapse images of 48 hpf zebrafish periderm cells expressing Lifeact-mRuby (actin) and Myl12.1-EGFP (myosin). Microridges fission as a myosin contraction dissipates (blue arrowheads). Microridges fuse as a myosin contraction intensifies (orange arrowheads). Images were inverted, so that high intensity fluorescence appears black and low intensity is white. Images

are still frames from Video 2-5. **(B)** Dot plot of the percentage of microridge fission and fusion events within 1μm of an NMII contraction over a 10-minute period. Graph compares unrotated channels to data analyzed after rotating the NMII fluorescence channel 90° relative to the actin fluorescence channel. Grey lines connect the unrotated samples to their rotated counterparts. n=6 cells from 6 fish, including 3 cells from 3 fish at 24 hpf and 3 cells from 3 fish at 48 hpf. $P=2.27x10^{-4}$, paired t-test. **(C)** Dot plot of the percentage of microridge fission and fusion events within 1μm of an NMII contraction over a 10-minute period. Graph compares contraction-associated fusion events to contraction-associated fission events in the same cells. Grey lines connect points from the same cell. n=6 cells from 6 fish, including 3 cells from 3 fish at 24 hpf and 3 cells from 3 fish at 48 hpf. P=0.778, paired t-test. **(D)** Representative color-coded temporal projections (corresponding to the bar on the left) of images from 10-minute time-lapse movies (30-second intervals) in 49 hpf zebrafish periderm cells expressing Lifeact-GFP after 1hr exposure to 1% DMSO (vehicle control) or 50μM blebbistatin. Microridges in control cells are more dynamic over the 10-minute period, so control cells appear more colorful than blebbistatin-treated cells. Images are temporal projections of Video 2-6. **(E)** Jittered dot plot of the sum of fission and fusion events in each cell, normalized to cell apical area, over a 10-minute period (events/μm·min) in cells after 1-hour exposure to 1% DMSO (vehicle control) or 50μM blebbistatin. n=5 cells from 5 fish for control and treatment. P=0.033, unpaired t-test.

Scale bars: 5μm (D).

‘*’ $p \geq 0.05$ and ‘***’ $p \geq 0.001$.

Bars in dot plots represent the mean.

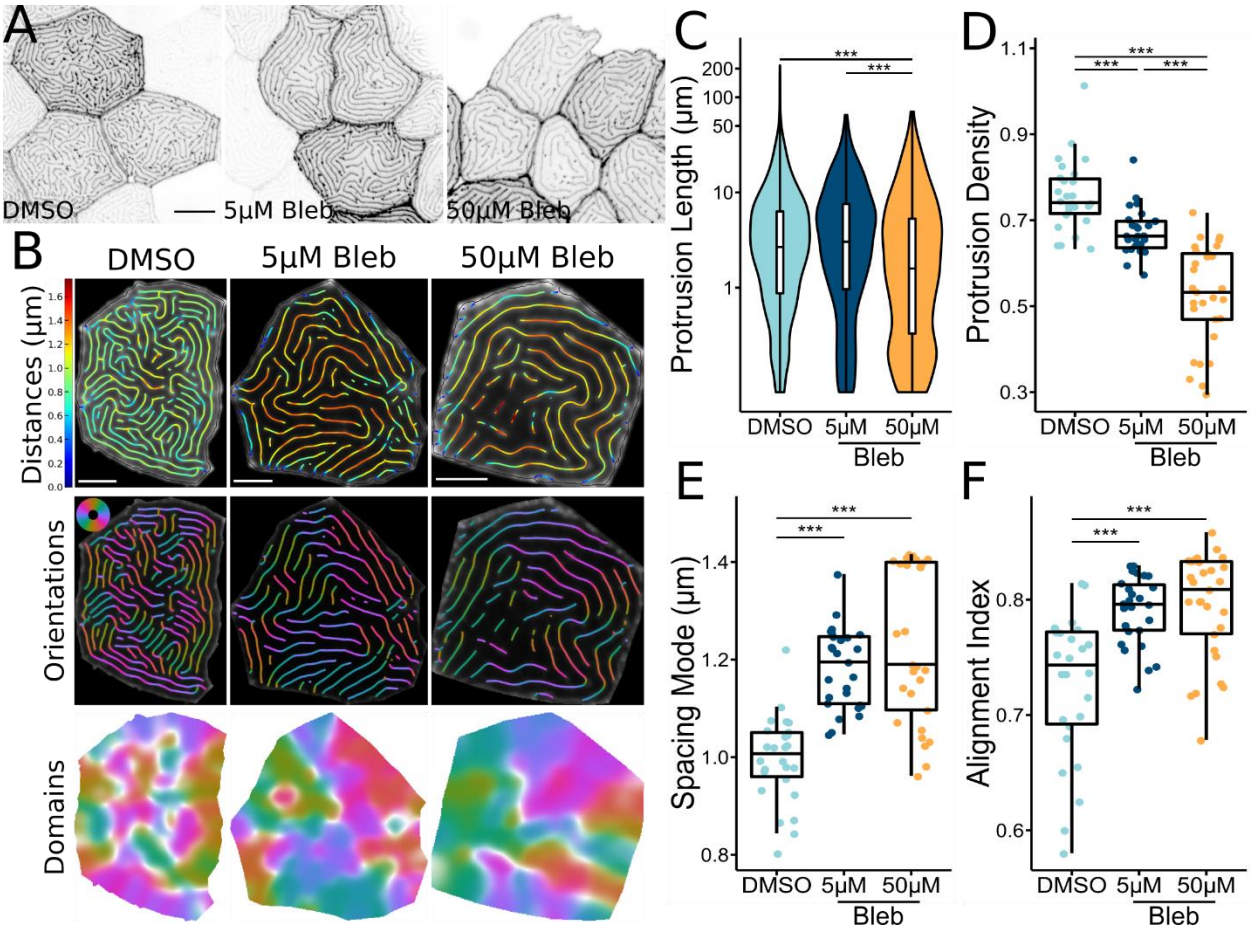

Figure 5. Inhibiting NMII changes microridge patterns. (A) Representative images of periderm cells expressing Lifeact-GFP on 72 hpf zebrafish after 24-hour exposure to the specified concentration of blebbistatin or vehicle control (DMSO). Images were inverted, so that high intensity fluorescence appears black and low intensity is white. **(B)** Visualizations of microridge distances, orientations, and alignment domains from periderm cells at 72 hpf after 24-hour exposure to the specified concentration of blebbistatin or vehicle control (DMSO). **(C)** Violin and box-and-whisker plot of projection length for periderm cells in 72 hpf zebrafish after 24-hour exposure to the specified concentration of blebbistatin or vehicle control (DMSO). DMSO, n=26 cells from 9 fish; 5μM blebbistatin, n=27 cells from 9 fish; 50μM blebbistatin, n=29 cells from 9 fish. $P<2.2x10^{-16}$, Kruskal-Wallis test followed by Dunn test with Benjamini-Hochberg p-value adjustment: DMSO-5μM blebbistatin, P=0.173; DMSO-50μM blebbistatin, $P=2.51x10^{-13}$; 5μM

blebbistatin-50μM blebbistatin, $P=3.79x10^{-17}$. **(D)** Dot and box-and-whisker plot of microridge density, defined as the sum microridge length (μm) normalized to apical cell area (μm^2), for periderm cells in 72 hpf zebrafish after 24-hour exposure to the specified concentration of blebbistatin or vehicle control (DMSO). DMSO, n=26 cells from 9 fish; 5μM blebbistatin, n=27 cells from 9 fish; 50μM blebbistatin, n=29 cells from 9 fish. $P=2.80x10^{-14}$, one-way ANOVA followed by Tukey's HSD test: DMSO-5μM blebbistatin, $P=3.07x10^{-3}$; DMSO-50μM blebbistatin, $P<2x10^{-16}$; 5μM blebbistatin-50μM blebbistatin, $P=7.70x10^{-8}$. **(E)** Dot and box-and-whisker plot of the mode distance between neighboring microridges in periderm cells in 72 hpf zebrafish after 24-hour exposure to the specified concentration of blebbistatin or vehicle control (DMSO). DMSO, n=26 cells from 9 fish; 5μM blebbistatin, n=27 cells from 9 fish; 50μM blebbistatin, n=29 cells from 9 fish. P=0.318, one-way ANOVA. **(F)** Dot and box-and-whisker plot of the alignment index on periderm cells in 72 hpf zebrafish after 24-hour exposure to the specified concentration of blebbistatin or vehicle control (DMSO). DMSO, n=26 cells from 9 fish; 5μM blebbistatin, n=27 cells from 9 fish; 50μM blebbistatin, n=29 cells from 9 fish. $P=4.56x10^{-7}$, one-way ANOVA followed by Tukey's HSD test: DMSO-5μM blebbistatin, $P=1.11x10^{-5}$; DMSO-50μM blebbistatin, $P=2.38x10^{-6}$; 5μM blebbistatin-50μM blebbistatin, P=0.951.

Scale bars: 10uM (A) and 5μm (B).

'**' $p \geq 0.01$ and '***' $p \geq 0.001$.

For box-and-whisker plots, middle box line is the median, and lower and upper ends of boxes are 25th and 75th percentiles, respectively.

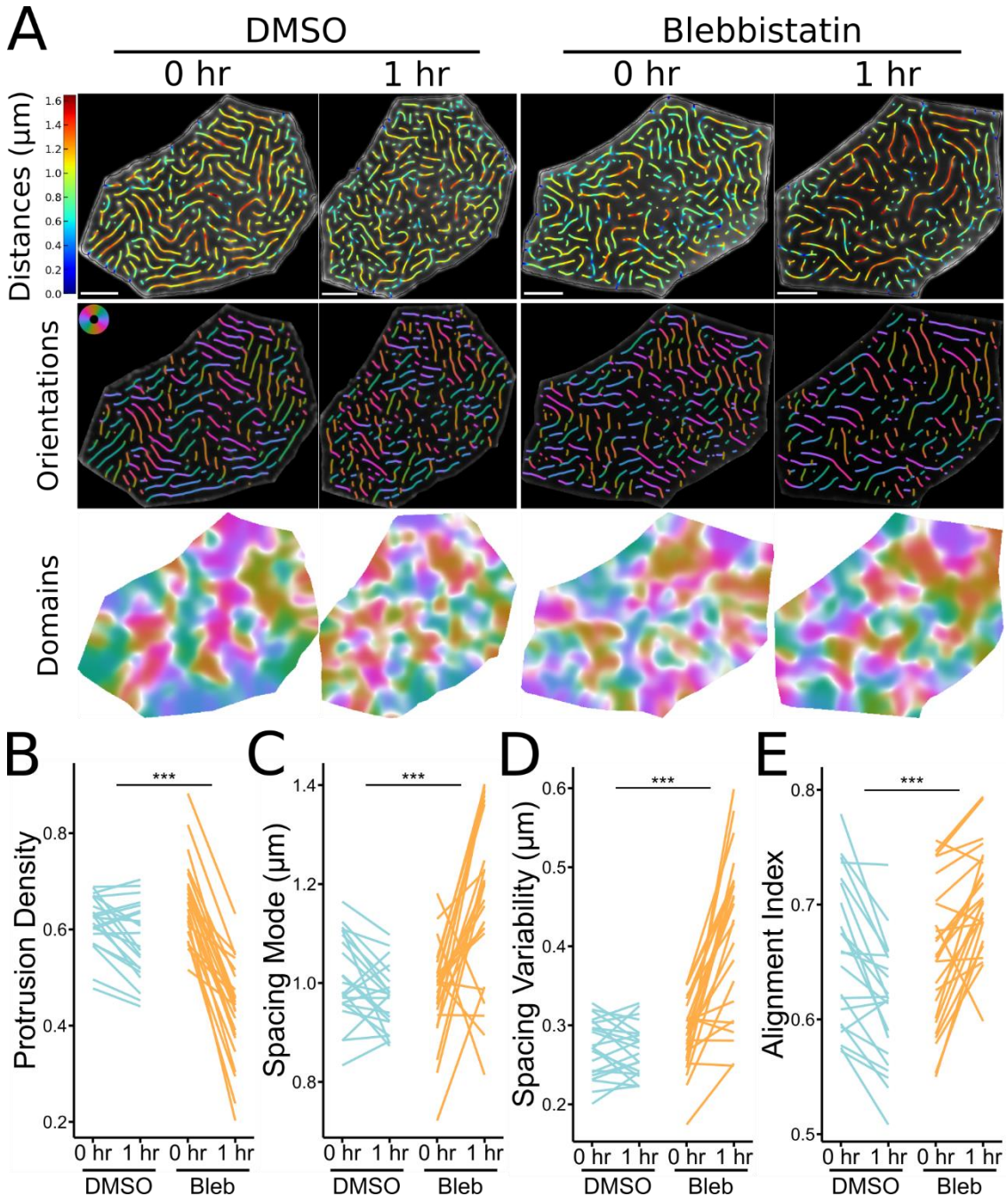

Figure 6. Short-term inhibition of NMII contractility alters microridge patterns in individual cells. (A) Representative visualizations of microridge distances, orientations, and alignment domains in periderm cells expressing Lifeact-GFP before (48 hpf, 0 hr) and after (49 hpf, 1hr) 1-hour treatment with 50µM blebbistatin or vehicle (DMSO). **(B)** Line plot of microridge density,

defined as the sum microridge length (μm) normalized to apical cell area (μm^2), from periderm cells before (48 hpf, 0 hr) and after (49 hpf, 1hr) 1-hour treatment with 50μM blebbistatin or vehicle control (DMSO). DMSO, n=22 cells from 4 fish; 50μM blebbistatin, n=25 cells from 4 fish. $P=4.09x10^{-11}$, one-way repeated measures ANOVA. **(C)** Line plot of microridge spacing mode from periderm cells before (48 hpf, 0 hr) and after (49 hpf, 1hr) 1-hour treatment with 50μM blebbistatin or vehicle control (DMSO). DMSO, n=22 cells from 4 fish; 50μM blebbistatin, n=25 cells from 4 fish. $P=7.76x10^{-6}$, one-way repeated measures ANOVA. **(D)** Line plot of microridge spacing variability (interquartile range of distances) between neighboring microridges in periderm cells before (48 hpf, 0 hr) and after (49 hpf, 1hr) 1-hour treatment with 50μM blebbistatin or vehicle control (DMSO). DMSO, n=22 cells from 4 fish; 50μM blebbistatin, n=25 cells from 4 fish. $P<2x10^{-16}$, one-way repeated measures ANOVA. **(E)** Line plot of the alignment index in periderm cells before (48 hpf, 0 hr) and after (49 hpf, 1hr) 1-hour treatment with 50μM blebbistatin or vehicle control (DMSO). DMSO, n=22 cells from 4 fish; 50μM blebbistatin, n=25 cells from 4 fish. $P=1.02x10^{-8}$, one-way repeated measures ANOVA.

Scale bars: 5μm (A).

‘***’ $p \geq 0.001$.

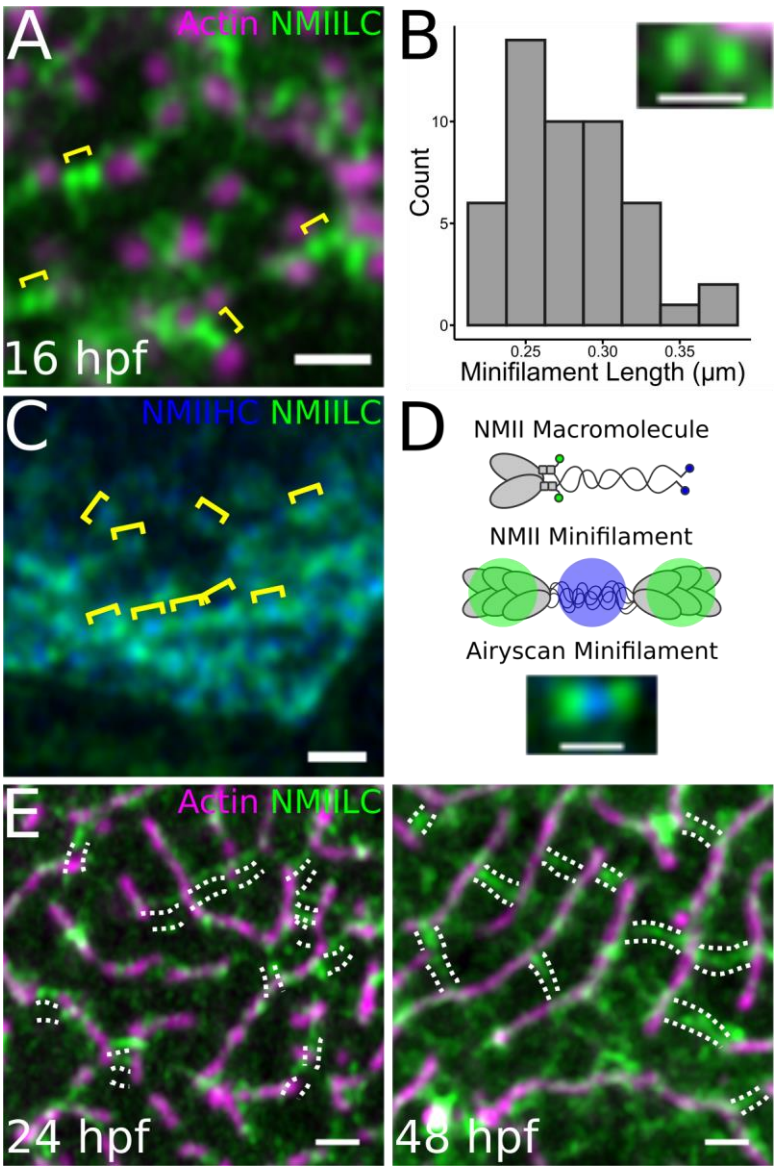

Figure 7. NMII minifilaments connect adjacent pegs and microridges. (A) Airyscan image of a 16 hpf zebrafish periderm cell expressing fluorescent reporters for actin (Lifeact-Ruby) and NMII light chain (Myl12.1-GFP). Pairs of green puncta (yellow brackets) appear in the cortex between adjacent pegs (magenta puncta). **(B)** Histogram of distances between the intensity maxima of presumptive NMII minifilaments. Inset is a representative image showing GFP signal at opposing ends of a presumptive NMII minifilament in a periderm cell expressing reporters for actin (Lifeact-Ruby) and NMII light chain (Myl12.1-GFP). n=49 minifilaments from 4 cells on 4 fish. **(C)** Airyscan

image of a 24 hpf zebrafish periderm cell expressing fluorescent reporters for NMII heavy chain (NMIIHC, Myh9a-mCherry) and NMII light chain (NMIILC, Myl12.1-GFP). NMIIHC channel was pseudo-colored blue. Brackets show examples of GFP-mCherry-GFP fluorescence patterns. **(D)** Diagram of NMII fluorescent protein fusion design and expected NMII minifilament fluorescence pattern. The upper graphic shows an NMII macromolecule, composed of two heavy chains, two essential light chains, and two regulatory light chains. GFP was fused to the regulatory light chains (Myl12.1-GFP), while mCherry was fused to the tail of the heavy chains (Myh9a-mCherry; represented in blue). The middle graphic shows the expected fluorescence pattern when multiple NMII macromolecules, labelled like the one in the upper graphic, assemble into an NMII minifilament. The lower Airyscan image shows an NMII minifilament in the cortex of a 24hpf zebrafish periderm cell expressing Myl12.1-GFP and Myh9a-mCherry. **(E)** Airyscan images showing NMII minifilaments connecting adjacent microridges side-to-side and end-to-end during (24hpf) and after (48hpf) microridge formation in periderm cells expressing reporters for actin (Lifeact-Ruby) and NMII light chain (Myl12.1-GFP). Dotted lines track along NMII minifilament “bridges”.

Scale bars: 1 μm (A, C, & E) and 500 nm (B & D)

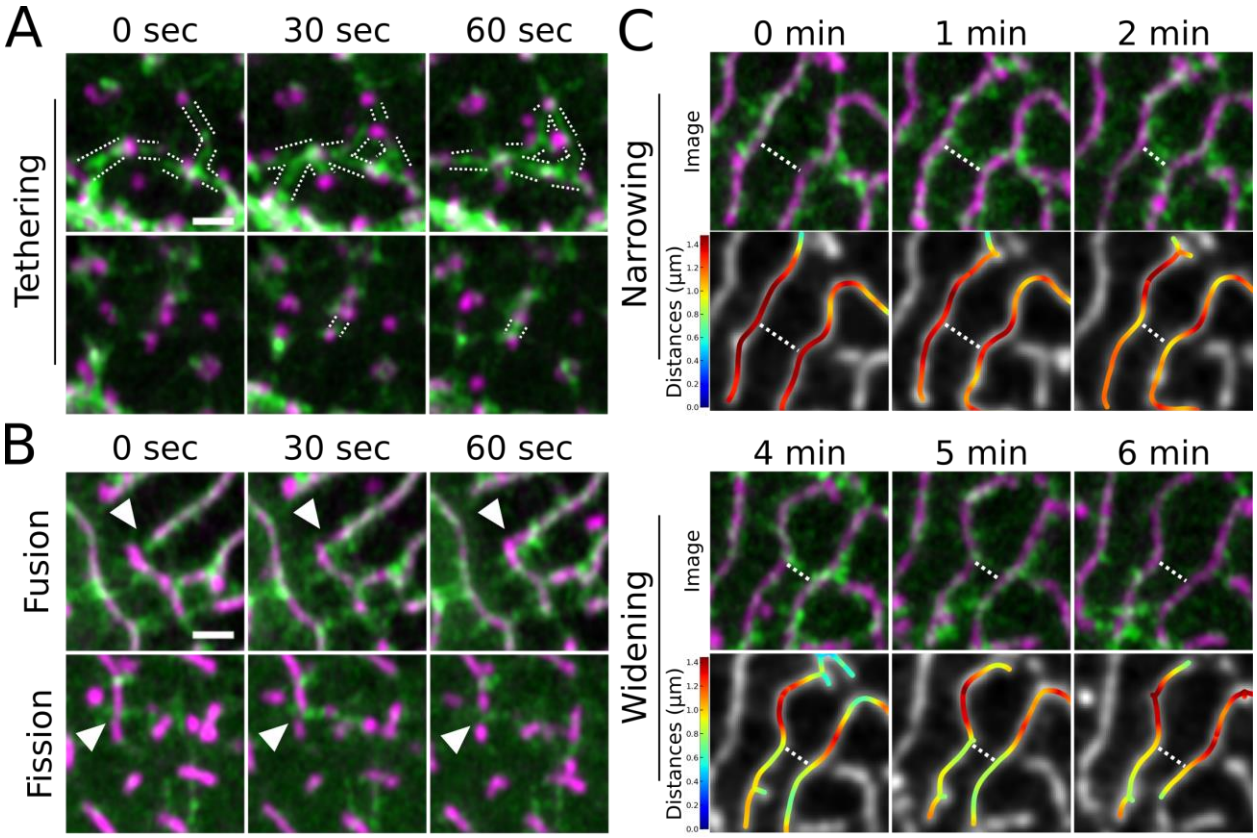

Figure 8. NMII minifilaments dynamically connect pegs and organize microridge rearrangements. (A) Airyscan time-lapse images of NMII minifilaments dynamically connecting pegs as they emerge in the cortex of a periderm cell expressing fluorescent reporters for actin (Lifeact-mRuby) and NMII (Myl12.1-GFP). Dotted lines track along NMII minifilament "bridges". Images include still frames from Video 2-7. **(B)** Airyscan time-lapse images of microridge rearrangements (white arrowheads) in periderm cells expressing fluorescent reporters for actin (Lifeact-mRuby) and NMII (Myl12.1-GFP). In the upper panels, an NMII minifilament connects the ends of adjacent microridges, fusing them together. In the lower panels, NMII minifilaments line up perpendicular to a microridge and appear to sever it. Images are still frames from Video 2-7. **(C)** Airyscan time-lapse images of microridge spacing dynamics in periderm cells expressing fluorescent reporters for actin (Lifeact-mRuby) and NMII (Myl12.1-GFP). Dotted line highlights narrowing and widening regions. Top rows show Airyscan images; bottom rows show color-coded

distances. Colors correspond to color bars on the left. The upper two rows show NMII minifilaments connecting two adjacent microridges and apparently pulling them together. The lower two rows show the NMII minifilament bridge between microridges dissipating as the adjacent microridges separate. Images are still frames from Video 2-7.

Scale bars: 1μm (A and B).

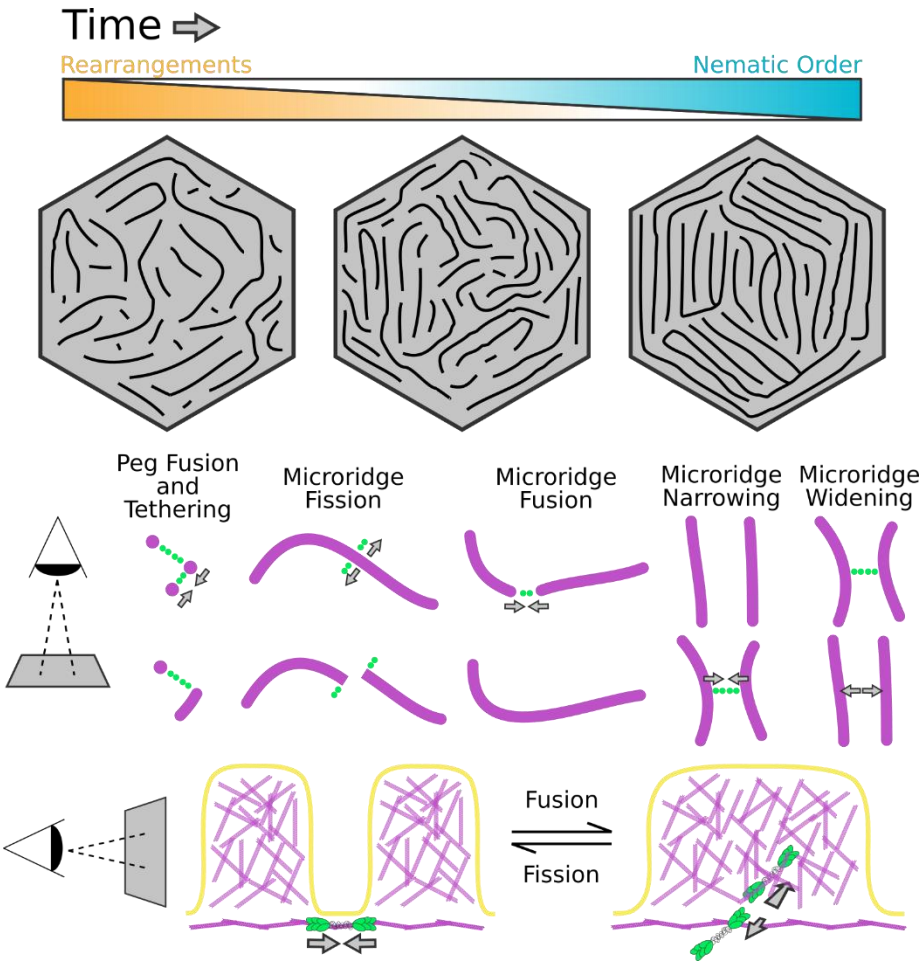

Figure 9. Model for microridge maturation and minifilament-mediated rearrangements

Top: The nematic order of microridge patterns increases as rearrangements decrease in frequency. **Bottom**: The orientation of NMII minifilaments determines the outcome of rearrangement events and regulates spacing (see Discussion).

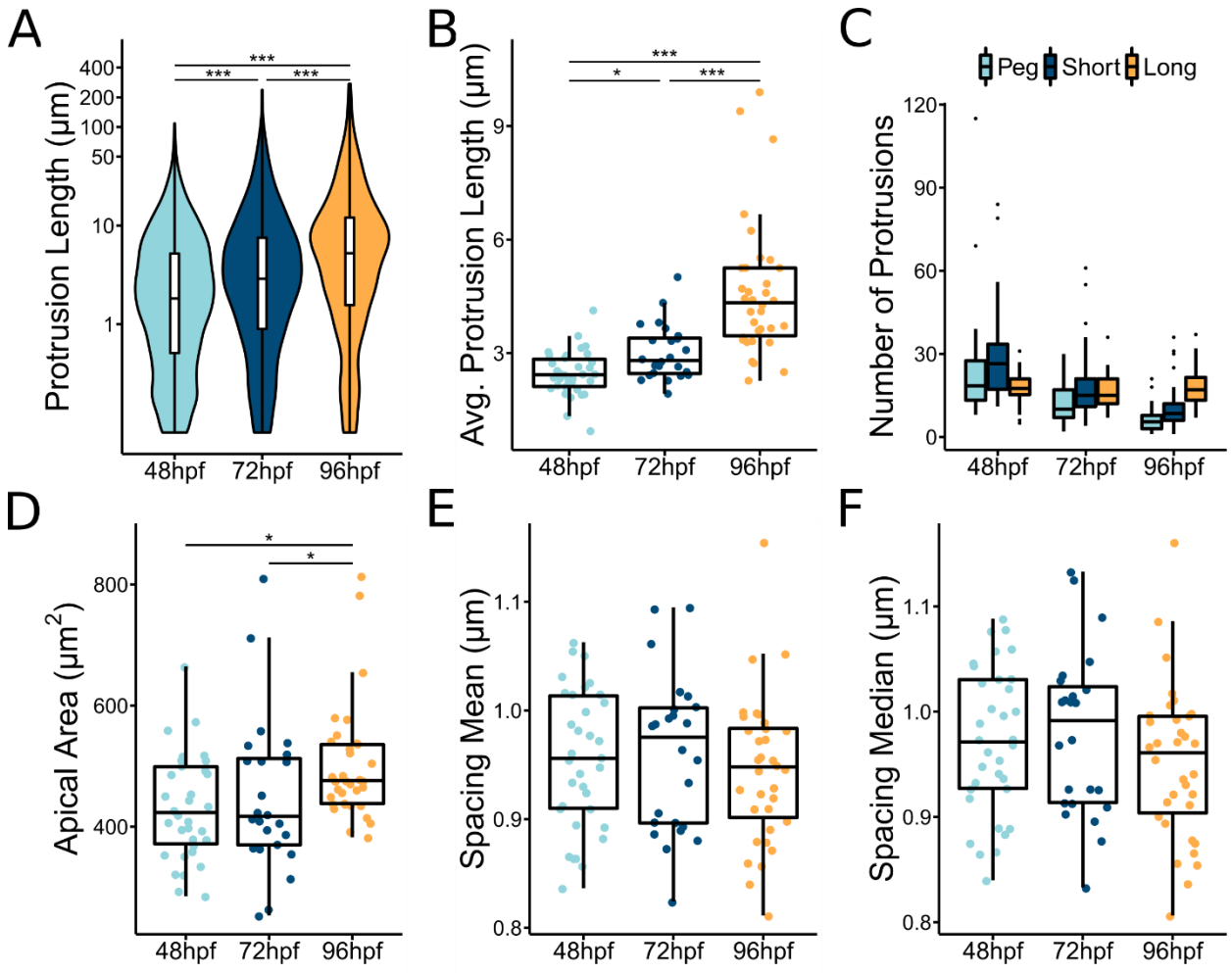

Fig S1. Additional quantification of morphological changes in maturing microridges. (A) Violin and box-and-whisker plot of protrusion length for periderm cells at the specified stage. 48 hpf, n=34 cells from 12 fish; 72 hpf, n=24 cells from 10 fish; 96 hpf, n=34 cells from 15 fish. $P<2.2x10^{-16}$, Kruskal-Wallis test followed by Dunn test with Benjamini-Hochberg p-value adjustment: 48-72 hpf, $P=1.36x10^{-14}$; 48-96 hpf, $P=2.67x10^{-59}$; 72-96 hpf, $P=6.08x10^{-14}$. **(B)** Dot and box-and-whisker plot of average protrusion length on periderm cells at the specified stage. 48 hpf, n=34 cells from 12 fish; 72 hpf, n=24 cells from 10 fish; 96 hpf, n=34 cells from 15 fish. $P=1.81x10^{-10}$, Kruskal-Wallis test followed by Dunn test with Benjamini-Hochberg p-value adjustment: 48-72 hpf, P=0.019; 48-96 hpf, $P=8.60x10^{-11}$; 72-96 hpf, $P=3.05x10^{-4}$. **(C)** Box-and-whisker plot of protrusion number distributed among pegs (<0.75µm), short microridges (0.75-

5μm), and long microridges (>5μm) on periderm cells at the specified stage. 48 hpf, n=34 cells from 12 fish; 72 hpf, n=24 cells from 10 fish; 96 hpf, n=34 cells from 15 fish. Two-way ANOVA with interaction: hpf, $P=3.12x10^{-12}$; protrusion type, $P=4.84x10^{-3}$; hpf-protrusion type interaction, $P=3.03x10^{-5}$. **(D)** Dot and box-and-whisker plot of periderm cell apical area at the specified stage. 48 hpf, n=34 cells from 12 fish; 72 hpf, n=24 cells from 10 fish; 96 hpf, n=34 cells from 15 fish. P=0.011, Kruskal-Wallis test followed by Dunn test with Benjamini-Hochberg p-value adjustment: 48-72 hpf, P=0.722; 48-96 hpf, P=0.014; 72-96 hpf, P=0.041. **(E)** Dot and box-and-whisker plot of microridge spacing mean for periderm cells at the specified stage. 48 hpf, n=34 cells from 12 fish; 72 hpf, n=24 cells from 10 fish; 96 hpf, n=34 cells from 15 fish. P=0.308, one-way ANOVA. **(F)** Dot and box-and-whisker plot of microridge spacing median for periderm cells at the specified stage. 48 hpf, n=34 cells from 12 fish; 72 hpf, n=24 cells from 10 fish; 96 hpf, n=34 cells from 15 fish. P=0.569, one-way ANOVA.

‘*’ $p \geq 0.05$ and ‘***’ $p \geq 0.001$.

For box-and-whisker plots, middle box line is the median, and lower and upper ends of boxes are 25th and 75th percentiles, respectively.

Video Legends

Video 2-1. Microridge fusion and fission diminish as microridge patterns mature

10-minute time-lapse videos with 30-second intervals of periderm cells expressing Lifeact-GFP in zebrafish at the indicated developmental stage. Microridge fusion and fission attenuate as microridges become longer and more aligned at each stage. Orange circles show locations of microridge fusions. Blue circles show locations of microridge fissions. Scale bar: 10μm.

Video 2-2. Microridges fuse and fission

4.5-minute time-lapse videos with 30-second intervals of periderm cells expressing Lifeact-GFP in 48hpf zebrafish. White arrowheads show locations of microridge fusion and fission events. Scale bar: 1μm.

Video 2-3. Microridge fusion and fission reflect fusion and fission of the plasma membrane

10-minute time-lapse video with 30-second intervals of periderm cells expressing fluorescent reporters for actin (Lifeact-GFP) and membrane (mRuby-PH-PLC) on 48hpf zebrafish. Microridge fusion (yellow arrowhead) and fission (white arrowhead) in the actin channel are mimicked by fission and fusion of projections in the membrane channel. Time-lapse frames are sum projection images. Scale bar: 1μm.

Video 2-4. Rapid cell shape changes do not induce microridge fusion and fission

60-minute time-lapse video with 1-minute intervals of periderm cells expressing Lifeact-GFP on 72hpf zebrafish. Time-lapse begins immediately after laser ablation of periderm cells on either

side of the cell of interest. The cell of interest rapidly elongates between the two wounds, but does not increase fusion and fission events. Scale bar: 10μm.

Video 2-5. NMII contractions correlate with microridge fusion and fission

10-minute time-lapse video with 30-second intervals of periderm cells expressing fluorescent reporters for actin (Lifeact-mRuby) and NMII (Myl12.1-EGFP) on 48hpf zebrafish. Microridges fuse near sites of intensifying myosin fluorescence signal (yellow arrowheads) and fission near sites of diminishing myosin fluorescence signal (white arrowhead). Scale bar: 1μm.

Video 2-6. Short-term NMII inhibition reduces microridge fusion and fission

10-minute time-lapse video with 30-second intervals of periderm cells expressing Lifeact-GFP on 49hpf zebrafish after 1-hour treatment with 1% DMSO or 50μm blebbistatin. Microridge fusion and fission decrease in periderm cells after 1-hour treatment with blebbistatin. Orange circles show locations of microridge fusions. Blue circles show locations of microridge fissions. Scale bar: 5μm.

Video 2-7. NMII minifilaments coordinate peg dynamics and microridge fusion, fission, and spacing

9-minute time-lapse videos with 1-minute intervals of periderm cells expressing fluorescent reporters for actin (Lifeact-mRuby) and NMII (Myl12.1-EGFP). NMII minifilaments appear as two green puncta. Different NMII-mediated events indicated by title cards. "Bridges" of one or two NMII minifilaments attach to pegs as they appear, and occasionally pull them toward one another. NMII minifilaments connect two microridge ends and fuse them into a longer microridge. NMII

minifilaments oriented perpendicular to a microridge in the x-y plane sever a microridge. Finally, NMII minifilament "bridges" connecting two adjacent microridges contract to pull the microridges closer together, and allow microridges to drift further apart as they disappear. Scale bar: 1μm.

References

Billington N, Wang A, Mao J, Adelstein RS, Sellers JR. 2013. Characterization of three full-length human nonmuscle myosin II paralogs. *J Biol Chem* **288**:33398–33410.

Chinowsky CR, Pinette JA, Meenderink LM, Lau KS, Tyska MJ. 2020. Non-muscle myosin-2 contractility-dependent actin turnover limits the length of epithelial microvilli. *Mol Biol Cell* mbcE20090582.

Çolakoğlu G, Brown A. 2009. Intermediate filaments exchange subunits along their length and elongate by end-to-end annealing. *The Journal of Cell Biology*. doi:10.1083/jcb.200809166

Crawley SW, Shifrin DA Jr, Grega-Larson NE, McConnell RE, Benesh AE, Mao S, Zheng Y, Zheng QY, Nam KT, Millis BA, Kachar B, Tyska MJ. 2014. Intestinal brush border assembly driven by protocadherin-based intermicrovillar adhesion. *Cell* **157**:433–446.

Depasquale JA. 2018. Actin Microridges: ACTIN MICRORIDGES IN EPITHELIUM. *Anat Rec* **31**:81.

Field CM, Pelletier JF, Mitchison TJ. 2019. Disassembly of Actin and Keratin Networks by Aurora B Kinase at the Midplane of Cleaving Xenopus laevis Eggs. *Curr Biol* **29**:1999–2008.e4.

Giannone G, Dubin-Thaler BJ, Rossier O, Cai Y, Chaga O, Jiang G, Beaver W, Döbereiner H-G, Freund Y, Borisy G, Sheetz MP. 2007. Lamellipodial actin mechanically links myosin activity with adhesion-site formation. *Cell* **128**:561–575.

Helker CSM, Schuermann A, Karpanen T, Zeuschner D, Belting H-G, Affolter M, Schulte-Merker S, Herzog W. 2013. The zebrafish common cardinal veins develop by a novel mechanism: lumen ensheathment. *Development* **140**:2776–2786.

Inaba Y, Chauhan V, van Loon AP, Choudhury LS, Sagasti A. 2020. Keratins and Plakin family

cytolinker proteins control the length of epithelial microridge protrusions. *Elife* **9**. doi:10.7554/eLife.58149

Jiang N, Rasmussen JP, Clanton JA, Rosenberg MF, Luedke KP, Cronan MR, Parker ED, Kim H-J, Vaughan JC, Sagasti A, Parrish JZ. 2019. A conserved morphogenetic mechanism for epidermal ensheathment of nociceptive sensory neurites. *Elife* **8**. doi:10.7554/eLife.42455

Kang Li @ CMU - Image Stabilizer Plugin for ImageJ. n.d. http://www.cs.cmu.edu/~kangli/code/Image_Stabilizer.html

Kelkar M, Bohec P, Charras G. 2020. Mechanics of the cellular actin cortex: From signalling to shape change. *Curr Opin Cell Biol* **66**:69–78.

Kwan KM, Fujimoto E, Grabher C, Mangum BD, Hardy ME, Campbell DS, Parant JM, Yost HJ, Kanki JP, Chien C-B. 2007. The Tol2kit: a multisite gateway-based construction kit for Tol2 transposon transgenesis constructs. *Dev Dyn* **236**:3088–3099.

Lam P-Y, Mangos S, Green JM, Reiser J, Huttenlocher A. 2015. In vivo imaging and characterization of actin microridges. *PLoS One* **10**:e0115639.

Loomis PA, Zheng L, Sekerková G, Changyaleket B, Mugnaini E, Bartles JR. 2003. Espin cross-links cause the elongation of microvillus-type parallel actin bundles in vivo. *J Cell Biol* **163**:1045–1055.

Magre I, Fandade V, Damle I, Banerjee P, Yadav SK, Sonawane M, Joseph J. 2019. Nup358 regulates microridge length by controlling SUMOylation-dependent activity of aPKC in zebrafish epidermis. *J Cell Sci* **132**. doi:10.1242/jcs.224501

Maître J-L, Berthoumieux H, Krens SFG, Salbreux G, Jülicher F, Paluch E, Heisenberg C-P. 2012. Adhesion functions in cell sorting by mechanically coupling the cortices of adhering cells. *Science* **338**:253–256.

Martin AC, Goldstein B. 2014. Apical constriction: themes and variations on a cellular mechanism driving morphogenesis. *Development* **141**:1987–1998.

Meenderink LM, Gaeta IM, Postema MM, Cencer CS, Chinowsky CR, Krystofiak ES, Millis BA, Tyska MJ. 2019. Actin Dynamics Drive Microvillar Motility and Clustering during Brush Border Assembly. *Dev Cell* **50**:545–556.e4.

Minoshima Y, Kawashima T, Hirose K, Tonozuka Y, Kawajiri A, Bao YC, Deng X, Tatsuka M, Narumiya S, May WS Jr, Nosaka T, Semba K, Inoue T, Satoh T, Inagaki M, Kitamura T. 2003. Phosphorylation by aurora B converts MgcRacGAP to a RhoGAP during cytokinesis. *Dev Cell* **4**:549–560.

Murphy DA, Courtneidge SA. 2011. The “ins” and “outs” of podosomes and invadopodia: characteristics, formation and function. *Nat Rev Mol Cell Biol* **12**:413–426.

Narayanan P, Chatterton P, Ikeda A, Ikeda S, Corey DP, Ervasti JM, Perrin BJ. 2015. Length regulation of mechanosensitive stereocilia depends on very slow actin dynamics and filament-severing proteins. *Nat Commun* **6**:6855.

Needleman D, Dogic Z. 2017. Active matter at the interface between materials science and cell biology. *Nature Reviews Materials* **2**:17048.

O’Brien GS, Martin SM, Söllner C, Wright GJ, Becker CG, Portera-Cailliau C, Sagasti A. 2009a. Developmentally regulated impediments to skin reinnervation by injured peripheral sensory axon terminals. *Curr Biol* **19**:2086–2090.

O’Brien GS, Rieger S, Martin SM, Cavanaugh AM, Portera-Cailliau C, Sagasti A. 2009b. Two-photon axotomy and time-lapse confocal imaging in live zebrafish embryos. *J Vis Exp*. doi:10.3791/1129

Pinto CS, Khandekar A, Bhavna R, Kiesel P, Pigino G, Sonawane M. 2019. Microridges are apical

epithelial projections formed of F-actin networks that organize the glycan layer. *Sci Rep* **9**:12191.

Raman R, Damle I, Rote R, Banerjee S, Dingare C, Sonawane M. 2016. aPKC regulates apical localization of Lgl to restrict elongation of microridges in developing zebrafish epidermis. *Nat Commun* **7**:11643.

Rasmussen JP, Sack GS, Martin SM, Sagasti A. 2015. Vertebrate epidermal cells are broad-specificity phagocytes that clear sensory axon debris. *J Neurosci* **35**:559–570.

Ridley AJ. 2015. Rho GTPase signalling in cell migration. *Curr Opin Cell Biol* **36**:103–112.

Riedl J, Crevenna AH, Kessenbrock K, Yu JH, Neukirchen D, Bista M, Bradke F, Jenne D, Holak TA, Werb Z, Sixt M, Wedlich-Soldner R. 2008. Lifeact: a versatile marker to visualize F-actin. *Nat Methods* **5**:605–607.

Schindelin J, Arganda-Carreras I, Frise E, Kaynig V, Longair M, Pietzsch T, Preibisch S, Rueden C, Saalfeld S, Schmid B, Tinevez J-Y, White DJ, Hartenstein V, Eliceiri K, Tomancak P, Cardona A. 2012. Fiji: an open-source platform for biological-image analysis. *Nat Methods* **9**:676–682.

Straight AF, Cheung A, Limouze J, Chen I, Westwood NJ, Sellers JR, Mitchison TJ. 2003. Dissecting temporal and spatial control of cytokinesis with a myosin II Inhibitor. *Science* **299**:1743–1747.

Tarchini B, Lu X. 2019. New insights into regulation and function of planar polarity in the inner ear. *Neurosci Lett* **709**:134373.

Touré A, Mzali R, Liot C, Seguin L, Morin L, Crouin C, Chen-Yang I, Tsay Y-G, Dorseuil O, Gacon G, Bertoglio J. 2008. Phosphoregulation of MgcRacGAP in mitosis involves Aurora B and Cdk1 protein kinases and the PP2A phosphatase. *FEBS Lett* **582**:1182–1188.

Tyska MJ, Mooseker MS. 2002. MYO1A (brush border myosin I) dynamics in the brush border of LLC-PK1-CL4 cells. *Biophys J* **82**:1869–1883.

van Laarhoven PJM, Aarts EHL. 1987. Simulated annealing In: van Laarhoven PJM, Aarts EHL, editors. Simulated Annealing: Theory and Applications. Dordrecht: Springer Netherlands. pp. 7–15.

van Loon AP, Erofeev IS, Maryshev IV, Goryachev AB, Sagasti A. 2020. Cortical contraction drives the 3D patterning of epithelial cell surfaces. *J Cell Biol* **219**. doi:10.1083/jcb.201904144

Weisshart K. 2014. The basic principle of airyscanning. *Zeiss Technology Note* **22**.

Xu K, Zhong G, Zhuang X. 2013. Actin, spectrin, and associated proteins form a periodic cytoskeletal structure in axons. *Science* **339**:452–456.

Zhang D-S, Piazza V, Perrin BJ, Rzadzinska AK, Poczatek JC, Wang M, Prosser HM, Ervasti JM, Corey DP, Lechene CP. 2012. Multi-isotope imaging mass spectrometry reveals slow protein turnover in hair-cell stereocilia. *Nature* **481**:520–524.

Chapter 4

Conclusions and future perspectives

The observations and experiments performed here describe the mechanisms of microridge formation and pattern maturation in live animals. This work also demonstrates essential roles for NMII contraction in both of these processes. During early larval development, the surfaces of zebrafish periderm cells are covered in finger-like protrusions that we have dubbed “pegs”. At this early stage, NMII contracts the apical cortex, constricting periderm cells and appearing in localized pulses that concentrate near cell borders. Cortical NMII contractions reduce membrane surface tension allowing pegs to fuse to one another and thereby elongate into microridges. Locally, individual NMII minifilaments in the cortex tether pegs to one another and contract between them, pulling them together. As periderm cells constrict, NMII contraction gradually spreads from cell borders toward the center of the cell surface, becoming ubiquitous across the cortex of periderm cells. Microridges gradually assemble and elongate through a dynamic process of fission and fusion which occurs in a pattern that mimics the concentric progression of cortical contraction. Cortical NMII minifilaments connect adjacent microridges and orchestrate fusion and fission events by pulling them together or apart. Microridges continue to fuse and fission after they finish formation and cover the surface of periderm cells. However, these dynamic microridge rearrangements diminish as the microridge pattern matures. As the larvae develops, microridges locally align with one another and become more evenly spaced. Continued NMII contraction after initial microridge formation allows periderm cells to reorganize microridges into more energetically favorable conformations, progressively creating more ordered patterns.

In the process of investigating the role of NMII contraction in microridge morphogenesis, this dissertation has described broader principles that could have implications outside the context of microridge development. First, is the important role that contraction plays in reducing membrane tension to allow the formation of protrusions. In some contexts, actin polymerization is sufficient to bend the cell membrane and form a protrusion (Raucher and Sheetz, 2000; Leijnse

et al., 2015). This work demonstrates that NMII contraction can be used to overcome the same energy barrier. The second principle my work has demonstrated is that the morphology of protrusions can be directly affected by the organization of the underlying cytoskeletal network, i.e. the apical cortex/terminal web. Although the relationship between the networks of protrusions and cortices is still incompletely understood, the impact of cortical myosin organization on the morphogenesis of microridges demonstrates that the two networks are inextricably linked. This principle is further supported by additional observations in which the morphology of protrusions and the organization of the terminal web are disrupted simultaneously (Seki et al., 2017).

Although the experiments described in this dissertation greatly progress our understanding of microridge formation and pattern maturation, there are many aspects of both processes that warrant further investigation. One open question concerns the origin of the microridge precursor structures, pegs. Morphologically, pegs bear resemblance to microvilli, which are found on many cell types (Elsaesser and Paysan, 2007; Fisher et al., 2008; Sauvanet et al., 2015), and can mature into other types of protrusions, like stereocilia (Tilney et al., 1992), or even assemble into microridge structures (Gorelik et al., 2003). With the exception of actin, very few molecular components of pegs are known, and further work will be needed to determine their similarity to microvilli. Although it is still a topic of active research in microvilli, it will be of particular importance to identify the actin-nucleating and polymerizing proteins that form pegs. The ability to directly inhibit peg formation would help answer an important question about microridge structure and assembly: whether pegs are molecularly unique structures that retain a distinct molecular organization within microridges. There are several lines of evidence that suggest that pegs are structurally distinct microridge components. Previous TEM studies have shown both bundled and branched actin organizations within microridges (Bereiter-Hahn et al., 1979; Schliwa, 1975; Uehara et al., 1991). This work and other studies (Lam et al., 2015; Inaba et al., 2020; Pinto et al., 2019) have demonstrated that inhibiting the branched actin nucleator

Arp2/3 prevents microridge elongation and disassembles microridges, but has no apparent effects on pegs. Finally, actin fluorescence reporters reveal bright punctae that appear within, and sometimes move between, mature microridges (this dissertation). However, it has not been explicitly established that pegs retain their molecular identity within microridges. Inhibition of peg formation or identification of peg-specific proteins could address whether pegs are required for microridge formation, whether bright actin fluorescence reporter punctae represent pegs within microridges, and whether peg dynamics contribute to the densification of microridge protrusions on periderm cells over time.

Another aspect of microridge formation and pattern maturation that warrants further study is the regulation of the, apparently stochastic, contractile activity of the periderm cell cortex. NMII contractions similar to those I have observed in periderm cells have also been observed in other epithelial cells (Solon et al., 2009; Martin et al., 2009; Munro et al., 2004; Fernandez-Gonzalez and Zallen, 2011). In many of these systems pulsatile NMII contraction is activated by RhoA through ROCK (Mason et al., 2013; Munjal et al., 2015). I demonstrated that ROCK is required for NMII contraction and microridge development, suggesting that NMII contractions in periderm cells are also regulated by RhoA. Expression of a dominant negative RhoA protein has also been shown to alter microridge spacing (Lam et al., 2015). However, RhoA regulation is complex and can be influenced by many different factors including signalling from GPCRs (Kerridge et al., 2016), interaction with apico-basal polarity proteins (Silver et al., 2019), and feedback from it's own downstream effects (Munjal et al., 2015; Segal et al., 2018). Additional experiments will be required to determine how RhoA regulates contraction during microridge formation and pattern maturation. Several fluorescent reporters have been used to visualize RhoA activity in live cells (Benink and Bement, 2005; Munjal et al., 2015). Direct visualization of RhoA activity in periderm cells would allow us to see local activity patterns of RhoA and analyze how they spatially and temporally correlate with NMII contraction. To determine how RhoA is regulated upstream, I

would analyze NMII and RhoA fluorescent reporter activity in a small CRISPR screen of potential GEF and GAP regulators of RhoA using a screening method previously-validated in zebrafish (Wu et al., 2018).

NMII contraction can also be affected by the organization of the actin network. The orientation, length, and connectivity of actin all impact tension generated by myosins (Kelkar et al., 2020). During microridge formation cortical NMII contraction relieves membrane tension and allows pegs to coalesce into microridges. It is possible that contraction plays a similar role in rearranging microridges after they have formed. I observed that NMII minifilaments in the cortex are associated with, and oriented perpendicular to, the sides of microridges. The formation and maturation of microridge patterns may, therefore, represent a gradual reorganization or the cortical actomyosin network: an initially isotropic cortex, present while pegs are the predominant protrusions, may transition to an anisotropic cortex in which NMII minifilaments are radially arranged, connecting the microridges, which wrap around the cell surface in a roughly concentric pattern. This would result in a feedback mechanism by which NMII contractility is not only regulated biochemically, but also by its own effects on the changing architecture of the cortical actomyosin network as microridges form and organize on the cell surface. Further investigation will be required to test this possibility more directly. Platinum replica electron microscopy could confirm my observations and provide insight into cortical organization in much greater detail. Inhibiting cortical components, like actin crosslinking proteins, would allow us to observe how altering cortical organization affects NMII contraction, as well as microridge formation and pattern maturation. Another way to test this hypothesis would be to observe myosin contraction and minifilament organization during the anisotropic microridge formation that occurs in rapidly elongating cells following neighbor cell ablation. These experiments, and others, will contribute to more fully understanding the complex interplay between the apical cortex and microridge protrusions.

References

Benink, H.A., and W.M. Bement. 2005. Concentric zones of active RhoA and Cdc42 around single cell wounds. *J. Cell Biol.* 168:429–439.

Bereiter-Hahn, J., M. Osborn, K. Weber, and M. Vöth. 1979. Filament organization and formation of microridges at the surface of fish epidermis. *J. Ultrastruct. Res.* 69:316–330.

Elsaesser, R., and J. Paysan. 2007. The sense of smell, its signalling pathways, and the dichotomy of cilia and microvilli in olfactory sensory cells. *BMC Neurosci.* 8 Suppl 3:S1.

Fernandez-Gonzalez, R., and J.A. Zallen. 2011. Oscillatory behaviors and hierarchical assembly of contractile structures in intercalating cells. *Phys. Biol.* 8:045005.

Fisher, P.J., P.A. Bulur, S. Vuk-Pavlovic, F.G. Prendergast, and A.B. Dietz. 2008. Dendritic cell microvilli: a novel membrane structure associated with the multifocal synapse and T-cell clustering. *Blood*. 112:5037–5045.

Gorelik, J., A.I. Shevchuk, G.I. Frolenkov, I.A. Diakonov, M.J. Lab, C.J. Kros, G.P. Richardson, I. Vodyanoy, C.R.W. Edwards, D. Klenerman, and Y.E. Korchev. 2003. Dynamic assembly of surface structures in living cells. *Proc. Natl. Acad. Sci. U. S. A.* 100:5819–5822.

Inaba, Y., V. Chauhan, A.P. van Loon, L.S. Choudhury, and A. Sagasti. 2020. Keratins and the plakin family cytolinker proteins control the length of epithelial microridge protrusions. *Elife*. 9. doi:10.7554/eLife.58149.

Kelkar, M., P. Bohec, and G. Charras. 2020. Mechanics of the cellular actin cortex: From signalling to shape change. *Curr. Opin. Cell Biol.* 66:69–78.

Kerridge, S., A. Munjal, J.-M. Philippe, A. Jha, A.G. de las Bayonas, A.J. Saurin, and T. Lecuit.

2016. Modular activation of Rho1 by GPCR signalling imparts polarized myosin II activation during morphogenesis. *Nat. Cell Biol.* 18:261–270.

Lam, P.-Y., S. Mangos, J.M. Green, J. Reiser, and A. Huttenlocher. 2015. In vivo imaging and characterization of actin microridges. *PLoS One*. 10:e0115639.

Leijnse, N., L.B. Oddershede, and P.M. Bendix. 2015. An updated look at actin dynamics in filopodia. *Cytoskeleton* . 72:71–79.

Martin, A.C., M. Kaschube, and E.F. Wieschaus. 2009. Pulsed contractions of an actin-myosin network drive apical constriction. *Nature*. 457:495–499.

Mason, F.M., M. Tworoger, and A.C. Martin. 2013. Apical domain polarization localizes actin-myosin activity to drive ratchet-like apical constriction. *Nat. Cell Biol.* 15:926–936.

Munjal, A., J.-M. Philippe, E. Munro, and T. Lecuit. 2015. A self-organized biomechanical network drives shape changes during tissue morphogenesis. *Nature*. 524:351–355.

Munro, E., J. Nance, and J.R. Priess. 2004. Cortical flows powered by asymmetrical contraction transport PAR proteins to establish and maintain anterior-posterior polarity in the early C. elegans embryo. *Dev. Cell*. 7:413–424.

Pinto, C.S., A. Khandekar, R. Bhavna, P. Kiesel, G. Pigino, and M. Sonawane. 2019. Microridges are apical epithelial projections formed of F-actin networks that organize the glycan layer. *Sci. Rep.* 9:12191.

Raucher, D., and M.P. Sheetz. 2000. Cell spreading and lamellipodial extension rate is regulated by membrane tension. *J. Cell Biol.* 148:127–136.

Sauvanet, C., J. Wayt, T. Pelaseyed, and A. Bretscher. 2015. Structure, regulation, and functional

diversity of microvilli on the apical domain of epithelial cells. *Annu. Rev. Cell Dev. Biol.* 31:593–621.

Schliwa, M. 1975. Cytoarchitecture of surface layer cells of the teleost epidermis. *J. Ultrastruct. Res.* 52:377–386.

Segal, D., A. Zaritsky, E.D. Schejter, and B.-Z. Shilo. 2018. Feedback inhibition of actin on Rho mediates content release from large secretory vesicles. *J. Cell Biol.* 217:1815–1826.

Seki, Y., Y. Miyasaka, S. Suzuki, K. Wada, S.P. Yasuda, K. Matsuoka, Y. Ohshiba, K. Endo, R. Ishii, H. Shitara, S.-I. Kitajiri, N. Nakagata, H. Takebayashi, and Y. Kikkawa. 2017. A novel splice site mutation of myosin VI in mice leads to stereociliary fusion caused by disruption of actin networks in the apical region of inner ear hair cells. *PLoS One*. 12:e0183477.

Silver, J.T., F. Wirtz-Peitz, S. Simões, M. Pellikka, D. Yan, R. Binari, T. Nishimura, Y. Li, T.J.C. Harris, N. Perrimon, and U. Tepass. 2019. Apical polarity proteins recruit the RhoGEF Cysts to promote junctional myosin assembly. *J. Cell Biol.* 218:3397–3414.

Solon, J., A. Kaya-Copur, J. Colombelli, and D. Brunner. 2009. Pulsed forces timed by a ratchet-like mechanism drive directed tissue movement during dorsal closure. *Cell*. 137:1331–1342.

Tilney, L.G., M.S. Tilney, and D.J. DeRosier. 1992. Actin filaments, stereocilia, and hair cells: how cells count and measure. *Annu. Rev. Cell Biol.* 8:257–274.

Uehara, K., M. Miyoshi, and S. Miyoshi. 1991. Cytoskeleton in microridges of the oral mucosal epithelium in the carp, Cyprinus carpio. *Anat. Rec.* 230:164–168.

Wu, R.S., I.I. Lam, H. Clay, D.N. Duong, R.C. Deo, and S.R. Coughlin. 2018. A Rapid Method for Directed Gene Knockout for Screening in G0 Zebrafish. *Dev. Cell*. 46:112–125.e4.